THESIS
2

This is to certify that the

dissertation entitled

A Study of Conductivity in a Complex Geometry.

presented by

Sangil Hyun

has been accepted towards fulfillment
of the requirements for

Ph.D. degree in Physics & Astronomy

M. F. Thorpe
Major professor

Date July 6, 98

A STUDY OF CONDUCTIVITY IN A COMPLEX GEOMETRY

By

Sangil Hyun

A DISSERTATION

Submitted to
Michigan State University
In partial fulfillment of the requirements
For the degree of

DOCTOR OF PHILOSOPHY

Department of Physics and Astronomy

1998

ABSTRACT

A STUDY OF CONDUCTIVITY IN A COMPLEX GEOMETRY

By

Sangil Hyun

I present a study of the conductivity[1] of a material with a complex geometry. There are three main parts in this dissertation, the determination of the isotropic conductivity, anisotropic conductivity, and effective conductivity. In the first part, a method using a multi-probe measurement together with a numerical simulation is introduced for the determination of the *isotropic conductivity* in a complex geometry. This method has been demonstrated on micron-sized diamond crystallites and diamond homoepitaxial films. The 3d-computer image for the finite element method (FEM) has been reconstructed from the scanning electron microscope (SEM) photos. For a sample with four probes, a 6 x 6 geometrical factor matrix is generated from the FEM analysis. In addition, the experimental measurement on the sample provides another 6 x 6 resistance matrix. The sample conductivity and contact resistances can be determined by the least-square fitting for the geometrical factors and the resistances. In the second part, this method is generalized for the *anisotropic conductivity* that is represented by a 3 x 3 tensor. It has been validated on computer models and real material (bismuth). This modified numerical scheme using the FEM analysis and the *iterative linearization technique* has identified the anisotropic conductivity tensor within acceptable errors in most cases. Some conditions for the application of this technique have been suggested

from the analysis of the results. In the last part, I describe the *effective conductivity* of a *composite material*. Much research has been done to investigate the electric, thermal, and elastic properties of composite materials. However, only a few problems with a simple geometry have been solved analytically. For instance, the dielectric properties of a composite that includes two perfect circular conductors have been determined analytically by a multipole expansion method. However, for complex composites, the analytic solutions cannot be obtained in most cases. Therefore, a numerical technique using the finite element method has been introduced for problems where the analytic approach fails. The FEM analysis is known as the most effective scheme to solve a boundary value problem in a complicated geometry. The simulation using this method is a primary step to understanding the effective medium theory for a complex composite material. To demonstrate this technique in the study of composite materials, numerical simulations have been performed and the results have been compared with the analytical solutions for a simple composite material.

To all whom I am indebted for this,
especially North Koreans in the horrible famine.

ACKNOWLEDGMENTS

I would like to thank Professor M. F. Thorpe for his considerate and patient guidance over the years. His insights into physics and passions on the study have made a deep impression on me. Also, I like to appreciate Professors S. D. Mahanti, N. O. Birge, D. Stump, and S. Hawley for being my guidance committee members. The collaboration with Professor B. Golding, Professor A. R. Day, and Dr. M. D. Jaeger has been a great pleasure and experience to me. I want to acknowledge Ms. J. King for her help.

I appreciate many people who have shared their lives in this small building, especially, H. Seong, K. Chun, J. S. Moon, B. Djordjevic, and J. U. Kim. They have made my life here always delightful. I appreciate also L. Malete for his helping on my manuscript. I know there have been invaluable and uncountable help from many people who have not been named here. They should be acknowledged, too.

My study would not be accomplished without the prayer, support, and patience of my dear parents, M. G. Hyun and G. J. Kim, and whole family including a newly born nephew, SeongWon, whom I have not yet meet. My deep thanks should go to them.

I want to represent a special gratitude to my beloved Myeoung H. Oh who has shared the valuable and memorable times with me. I thank you more than I can express.

Finally, my thanks would go to Him who have created the world and me. In my whole life, He has lead me to the truth with His boundless love.

TABLE OF CONTENTS

LIST OF TABLES viii

LIST OF FIGURES x

CHAPTER 1 INTRODUCTION 1

CHAPTER 2 CONDUCTIVITY MEASUREMENT OF MICRON-SIZED DIAMOND CRYSTALLITES 4

- 2.1 INTRODUCTION 4
  - *2.1.1 motivation 4*
  - *2.1.2 van der Pauw formula for 2d film 8*
  - *2.1.3 inverse problem 11*
  - *2.1.4 Finite Element Method (FEM) 15*
- 2.2 THEORY 23
  - *2.2.1 conductivity and geometrical factors 23*
  - *2.2.2 resistance table and its properties 25*
  - *2.2.3 contact resistances 31*
- 2.3 COMPUTER SIMULATION 34
  - *2.3.1 reconstruction of 3d computer image 34*
  - *2.3.2 modeling and analysis using FEM 39*
  - *2.3.3 least square fitting 47*
- 2.4 EXPERIMENT 50
  - *2.4.1 sample preparation 50*
  - *2.4.2 four-probe measurement 53*
- 2.5 ANALYSIS 55
  - *2.5.1 diamond film 55*
  - *2.5.2 sample 1 (Ohmic contacts) 60*
  - *2.5.3 sample 2 (non-Ohmic contacts) 62*
- 2.6 CONCLUSION 68

CHAPTER 3 ANISOTROPIC CONDUCTIVITY MEASUREMENT FOR COMPLEX GEOMETRY 70

- 3.1 INTRODUCTION 70
- 3.2 THEORY 72
  - *3.2.1 anisotropic conductivity tensor 72*
  - *3.2.2 iterative linearization technique for nonlinear inverse problem 74*
  - *3.2.3 orthogonal transformation 80*
- 3.3 COMPUTER SIMULATION 81
  - *3.3.1 sample geometry 81*
  - *3.3.2 simulated experimental data using FEM 83*
  - *3.3.3 iterative linearization fitting using FEM 84*
- 3.4 EXPERIMENT 85
  - *3.4.1 sample preparation (Bi cylinder) 85*
  - *3.4.2 six-probe measurement 88*
- 3.5 ANALYSIS 89
  - *3.5.1 computer generated sample (2d) 89*

3.5.2 computer generated sample (3d) *92*
3.5.3 real sample (Bi cylinder) *96*
3.5.4 stability test *101*
3.6 CONCLUSION 106

CHAPTER 4 EFFECTIVE CONDUCTIVITY OF A MEDIUM WITH CIRCULAR INCLUSIONS 108
4.1 INTRODUCTION 108
4.2 A BRIEF HISTORY OF THE STUDY ON A COMPOSITE MATERIAL 109
4.3 THEORY 113
4.3.1 4-point resistance (R_4) *114*
4.3.2 2-point resistance (R_2) *118*
4.3.3 The ratio of R_4 and R_2 .... *121*
4.4 COMPUTER SIMULATION 122
4.4.1 FEM analysis for 2d composite *122*
4.4.2 FEM analysis for 3d composite *124*
4.5 ANALYSIS 126
4.5.1 2d composite *126*
4.5.2 3d composite *128*
4.5.3 The ratio of 4-point and 2-point resistances *130*
4.6 CONCLUSION 130

APPENDICES 133
A.1 RECIPROCITY THEOREM 134
A.2 COUNTING OF INDEPENDENT *4-TERMINAL* TERMS 138
A.3 RESISTANCES OF TWO PERFECT HYPERSPHERICAL CONDUCTORS 140

REFERENCES 145

LIST OF TABLES

Table 2.1 Selected properties of diamond structure semiconductors ------------------------ 4

Table 2.2 A resistance table from all possible combinations of voltage and current measurements -- 27

Table 2.3 How to generate the triangular matrix from six diagonal terms so that the triangular matrix produces a whole table -------------------------------- 30

Table 2.4 The number of independent elements in the resistance table --------------------30

Table 2.5 Resistance table with two contact resistances for current flows ------------------ 32

Table 2.6 The characteristics of the meshings for each sample ------------------------------ 42

Table 2.7 The Ohmic resistance table obtained from Table 2.5 (symmetric) ---------------48

Table 2.8 The non-Ohmic resistance table obtained from Table 2.5 (non-symmetric) ----- 48

Table 2.9 The characteristics of CVD diamond samples ------------------------------------52

Table 2.10 Resistances measured for homoepitaxial film by 4-probe experiment (kΩ)------ 56

Table 2.11 Geometrical factor table obtained by FEM (mm^{-1})-----------------------------------56

Table 2.12 The resistivity and contact resistances of diamond film (Film 1) given by van der Pauw formula (VDP) and our method. ------------------------------------ 56

Table 2.13 Resistances measured by 4-probe experiment (kΩ)---------------------------------58

Table 2.14 Another resistance table for the opposite current flows of Table 13 (kΩ)-------- 58

Table 2.15 Geometrical factors calculated from FEM (mm^{-1})-----------------------------------58

Table 2.16 The resistivity and contact resistances of Film 2 given by van der Pauw formula (VDP) and our method.--- 58

Table 2.17 Stability test of 4-terminal resistances on the position of one contact ------------59

Table 2.18 Resistances obtained from the experimental measurement for Sample 1 (kΩ)---61

Table 2.19 Geometrical factors from the finite element method for Sample 1 (μm^{-1})--------61

Table 2.20 Resistivity and contact resistances for Sample 1, assuming that all the contact resistances were Ohmic.-- 61

Table 2.21 Resistances obtained from the experimental measurement for Sample 2 (kΩ)---64

Table 2.22 Geometrical factors from the finite element method for Sample 2 (μm^{-1})------- 64

Table 2.23 Resistivity and contact resistances for Sample 2 ---------------------------------64

Table 2.24 Fit result of conductivity model with two activation energies for data in Figure 2.27 --66

Table 3.1 Electrical resistivity of metalic crystals. Values of principal resistivities at T=20° C. (in unit $10^{-6}\ \Omega$ cm) --- 71

Table 3.2 The comparison of the fitted results of the conductivity tensor elements with the prescribed values for the computer model in 2d --------------------------------- 91

Table 3.3 The comparison of the fitted results of the conductivity tensor elements with the prescribed values for the computer model in 3d ---------------------------------- 93

Table 3.4 Principal values of the resistivity of Bi. ($10^{-6}\ \Omega$ cm) ----------------------------99

Table 3.5 Different meshings for the stability test of a cylindrical sample ----------------- 102

Table 3.6 Different meshings for the stability test of Cylinder2 -----------------------------106

Table A.1 The number of independent 4-terminal terms in a resistance matrix for *n*-probe measurement ---139

LIST OF FIGURES

Figure 2.1 A polycrystalline diamond film (a) and a bicrystal (b) that was formed by two single crystallites ---------- 5

Figure 2.2 A typical shape of CVD diamonds used in this measurement. It is a micron-sized sample grown on a Si substrate.---------- 6

Figure 2.3 The conductivity measurement of a simple shaped sample is usually straightforward. This cylindrical geometry forms constant electric current pattern inside the sample ---------- 7

Figure 2.4 The conductivity measurement of 2D film in arbitrary geometry is done by four-probe measurement.---------- 9

Figure 2.5 A clover-shaped film (a) and a bridge-shaped film (b) are used for four-probe measurement.---------- 10

Figure 2.6 A schematic of the *inverse* and *direct* problem. Those two problems can be characterized by what is known and what is determined in the problem.---------- 12

Figure 2.7 Heat conduction problem on a simple bar ---------- 13

Figure 2.8 A boundary value problem is solved in this irregular geometry. Boundary conditions on each surface are needed.---------- 16

Figure 2.9 Some typical element shapes are presented for FEM. Each element has nodes on the vertices or some extra nodes on the edges to enhance the accuracy.---------- 17

Figure 2.10 Highly distorted meshes that are not usually acceptable in mesh generating ---- 18

Figure 2.11 A sample of meshed geometry with square-shaped elements in 2d ---------- 19

Figure 2.12 By the FEM analysis, a voltage distribution on a sample is obtained. The interpolation technique is used to obtain the distribution inside the elements.--- 22

Figure 2.13 For 2-terminal measurement, the voltage is calculated by a line integral along the path *l* and the current is obtained by a surface integral on the cross section *S*.--- 23

Figure 2.14 Showing a conductor that has four probes that are attached on the surface ------ 24

Figure 2.15 Micron-sized diamond crystal grown by a chemical vapor deposition technique before Au leads were attached. Five titanium contacts were formed on the surface and four of them (indexed) were used for the measurement. ---------- 26

Figure 2.16 Contact resistances have two different values (r_i, r_i') for non-Ohmic contacts. A resistance measurement consists of a sample resistance R_{sample} and contact resistances added in series.---------- 32

Figure 2.17 Each SEM photo is given in an orientation for viewing angle (θ, ϕ) as shown in this figure.-- 34

Figure 2.18 SEM photos of a sample (Sample 2) in various orientations. (a) $\theta, \phi = 0°, 0°$ (b) $\theta, \phi = 50°, 0°$ (c) $\theta, \phi = 50°, 90°$ (d) $\theta, \phi = 50°, 270°$ ------------------ 35

Figure 2.19 Computer images reconstructed from SEM photos by image processing. Five small pyramids on the surface denote five contacts. Compare these two images with the SEM photos in the Figure 2.18. --- 38

Figure 2.20 Triangular planes generated from three keypoints were combined into a large plane as shown in (a). A volume could be constructed by connecting these large planes into a volume unit. The volume elements for the diamond crystallites were presented in (b) and (c).-- 40

Figure 2.21 The elements used for the meshing of 2d film (square) and 3d crystallites (tetrahedra). Sometimes elements that have only four nodes on the corners were used.-- 42

Figure 2.22 Meshed structures of the diamond film(a) and crystallites (Sample 1(b), Sample 2 (c)). Figure 2.20(b) and (c). Each model has square-shaped contacts on the surface. -- 43

Figure 2.23 Equipotential lines on the surface of the samples given by ABAQUS. (a) is for homoepitaxial film. (b), (c) are for Sample 1. (d),(e) are for Sample 2. The figures of 3d samples were obtained in different orientations.---------------------------- 46

Figure 2.24 A normal picture of the 2d sample (diamond homoepitaxial film) is shown in (a). Two schematics ((b), (c)) of the sample denote the positions of the contacts. Film 1 (b) has four contacts and film 2 (c) has six contacts. Gray-colored squares in the figures represent the contacts actually used for the measurement.---------------- 51

Figure 2.25 Two micron-sized CVD diamond crystallites, Sample 1 (a) and Sample 2 (b). Sample 1 has Au leads attached on the Ti contacts and Sample 2 is a shape before the lead attachment -- 51

Figure 2.26 Temperature dependence of a resistance of diamond crystallites (Sample 1 (solid circles) and Sample 2 (open circles)). To investigate the temperature dependence of the resistivity of these samples, a four-terminal resistance (R_{23}^{14}) were measured over a wide range of temperatures.--- 54

Figure 2.27 Temperature dependence of the resistivities of the diamond samples. Two microcrystallites (MC-A, MC-B) correspond to Sample 1 and Sample 2. PF1 and PF2 are polycrystalline films. HF1 and HF2 are homoepitaxial films. The resistivity of these samples was obtained by rescaling the resistance measurement in Figure 2.26 using the fitted resistivity.--- 67

Figure 3.1 A diamond crystallite has a local defect (twin boundary) denoted by an arrow. This defect was neglected in the isotropic conductivity determination.---------------- 70

Figure 3.2 Iterative linearization technique of χ^2 minimization in 1d (Newton method). This technique is useful when the function form of the χ^2 is not known. Each step, the function form is approximated to a linearized form by Taylor expansion. After many iterations, it reaches the minimum point. -- 76

Figure 3.3 Many probes are attached on the surface of samples in 2d (a) and 3d (b). More contacts are needed for anisotropic conductivity tensor compared to isotropic conductivity tensor. -- 82

Figure 3.4 Schematics of a real sample (Bi cylinder) with six circular Au electrodes. (a) It is a relatively thin cylinder. Three contact pads were formed on each circular plane of the sample. (b) Three pads on a plane were formed to have an angle from three pads on the other plane.-- 86

Figure 3.5 The normal photos of the Bi sample for the real measurement.[2] It has six contacts that are formed on both sides of the circular planes. (a) and (b) show the formation of contacts on these two sides. The ruler shows the size of the sample.---------- 87

Figure 3.6 A computer generated sample for the determination of anisotropic conductivity. This 2d computer model has six circular probes. The contour map (b) shows the equipotential lines. The meshing was done by ANSYS and the analysis was done by ABAQUS.-- 89

Figure 3.7 These figures show the fitting procedures of the tensor in 2d. The fittings were performed using only 4-point resistances (a) or whole resistances in the table (b). Three data points are equivalent to three conductivity tensor terms.------------- 90

Figure 3.8 Two principal directions were drawn on the surface of 2d computer model. Three directions (one real and two fitted) represent a remarkable coincidence.---------91

Figure 3.9 The meshing (a) and equipotential lines (b) of a 3d computer generated sample. Six brick-shaped probes were formed on six facets of the sample.-------------- 94

Figure 3.10 These figures show the fitting procedures of the tensor in 3d. The fittings were performed using only 4-point resistances (a) or whole resistances in the table (b). Six parameters in a tensor were obtained each step. The iterations in 3d needed a few more steps to the optimum than in 2d.-- 95

Figure 3.11 Sensitivity test of the conductivities fitted by 4-point terms and whole table has been done to check the relation between the result and the Gaussian noise.------97

Figure 3.12 Equipotential lines of the real sample (Bi) obtained by FEM analysis.----------- 98

Figure 3.13 Fitting procedures of a resistivity tensor of the real sample. Two meshings were used to test our method on this sample. Only three principal components of the tensor were shown in these pictures. Two planar resistivity components (solid circle and square) are observed stable around the real value, but the perpendicular component (triangle) shows a substantial variation, especially in (b). ---------- 100

Figure 3.14 Resistivity fittings were done for the Bi sample using three different meshings. Bi10-1 is a fine meshing and Bi4-2 is a rough meshing. It turned out that the perpendicular resistivity component was so sensitive on the meshing while the other components were stable. -- 103

Figure 3.15 Resistivity fittings were performed on some modified structures. The modifications were done by rotating the contact pads. The dependence of the result on the angles was shown in the figure. Huge variations were observed for all components. Interestingly, two planar resistivity components (ρ_x, ρ_y) crossed over somewhere between 2° and 5° .--- 103

Figure 3.16 Equipotential lines of thicker cylindrical sample (Cylinder 2). This model has more layers of elements along the perpendicular direction. That may enhance the fitting result for that direction.-- 104

Figure 3.17 This graph was obtained from another computer test for the same geometry of the Bi cylinder (Cylinder 1). The simulated resistances were generated by the meshing Bi10-1. The fitted results from different meshings were presented. The perpendicular component (triangle) shows still a huge variation for this computer model.-- 105

Figure 3.18 Another computer test for a thick sample (Cylinder 2) as shown in Figure 3.16. The simulated resistances were generated by the meshing Bulk10-1. The fitting from other meshings could reproduce the all resistivity components nicely including the perpendicular component. -- 105

Figure 4.1 A composite material consists of two different dielectric constant regions (ε_0, ε_i) in dilute limit.-- 110

Figure 4.2 Elastic energy distribution in a composite material with many circular inclusions under hydrostatic pressure. The contour map was given by the elasticity analysis using ABAQUS. Elastic energy turned out to be distributed mostly near the necks between two circles. --- 112

Figure 4.3 4-point resistance measurement of two circular inclusions. The voltage between two inclusions is calculated in terms of the geometrical parameters when a constant electric field is applied. --- 115

Figure 4.4 Normalized current I_0 is defined by the total current flowing through the cross section of the inclusions.--116

Figure 4.5 One dimensional composite material with two perfect conductor inclusions.---- 117

Figure 4.6 2-point resistance measurement of two circular inclusions. A resistance is obtained when the current flows between these two inclusions. ------------------------- 119

Figure 4.7 The geometry of 2d composite material with circular inclusions. Huge plates were attached to the host to form a constant electric field in 4-point resistance measurement. Those plates were removed for 2-point resistance measurement - 123

Figure 4.8 Contour graphs of voltage distribution near the neck in 2d. (a) is given from 4-point measurement and (b) is given from 2-point measurement. ------------------123

Figure 4.9 Three-dimensional composite material with two spherical inclusions. Similar large bricks were attached to the host for 4-point measurement ---------------------- 125

Figure 4.10 Contour graph of voltage distribution near the neck in 3d. (a) is given from 4-point measurement and (b) is given from 2-point measurement ----------------------- 125

Figure 4.11 The meshed structure of the spherical inclusions. For a rough meshing, as these spheres approach together, the shape of the neck is getting less realistic because of the sharp ends of the spheres --126

Figure 4.12 Numerical solutions of the 4-point and 2-point resistances were obtained for 2d composite using FEM analysis. They agree well in all regions with the analytical solutions. (b) shows the detail in the close neck limit --------------------------- 127

Figure 4.13 Numerical solutions of the 4-point and 2-point resistances were obtained for 3d composite using FEM analysis. They agree nicely in most regions with the analytical solutions, but show some disagreements in an asymptotic regime (close limit). (b) shows the detail in that limit -- 129

Figure 4.14 The ratio between 4-point resistance and 2-point resistance in 2d and 3d. Each ratio was observed to approach a constant in the close neck limit ($w/a << 1$). The limiting value is given by π in 2d and $\pi^2/3$ in 3d ------------------------------- 131

Figure A.1 A sample with four probes and its equivalent circuit. The electric circuit is composed of many resistors that are fully connected ----------------------------- 135

Figure A.2 Two circular perfect conductors in a host material in the close neck limit ------ 141

Chapter 1 INTRODUCTION

The determination of the physical properties of a material has been one of the main topics in experimental and theoretical research over the years. It has been a primary step to characterize a specific material in most experiments. Moreover, the study has been considered as an important approach to investigate the structural dependence of material properties for some structured materials such as glasses, amorphous solids, and composites. The effective material properties have been considered for a composite that consists of more than one material. Some studies have been conducted to find an optimum structure associated with these physical properties (electric, mechanical, and thermal). The determination of these properties is usually straightforward in a simple geometry. However, it is not possible for complex structures such as an arbitrary-shaped diamond crystallite. The trouble in the determination usually comes from the complicated geometry of the material. This is one of main motivations of this study. The finite element method (FEM) has been adapted to deal with this trouble numerically. This technique is a powerful tool to solve a boundary value problem especially in a complex geometry. Sometimes, another computer simulation technique could be used to enhance the performance of this method. This numerical technique in the determination of the material properties provides a way to overcome a major limitation that results from complex geometry.

In this dissertation, I describe the numerical determination of material properties. Throughout my work, only the electric properties (conductivity, resistance) have been considered. However, the methods suggested in this study can be applied to the determination of other material properties (thermal, elastic, etc.), too. In Chapter 2, I present the numerical method for the determination of the conductivity of micron-sized diamond crystallites. For this diamond sample, the conductivity is isotropic due to its symmetric lattice structure. The method is demonstrated on a diamond film for the comparison with the well-known van der Pauw method. Two main procedures, the multi-probe measurement and the FEM analysis are required to identify the sample conductivity. This work could be considered as the first measurement of a diamond crystallite in micron scale. In addition to conductivity, contact resistances are determined also quantitatively. The conductivity measurement of a single diamond crystal provides a primary step to the study of the transport properties in polycrystalline films. In Chapter 3, I introduce a more generalized technique for the evaluation of anisotropic conductivity that involves the 3 x 3 tensor. Aided by another computer simulation (iterative linearization technique), the method using FEM analysis determines the anisotropic tensor in a complex geometry. This generalized technique has been tested for computer models and for a real material (bismuth). The conditions for the application of this technique are obtained from the analysis of the result. In Chapter 4, this numerical technique (FEM) is introduced to study the electrical properties of a composite. A simple composite in 2d, which consists of a host and two circular inclusions has been selected for the demonstration of the method because some analytic solutions of the electric conduction problem are available in this geometry. Two resistances (4-point and 2-point) in the composite are defined and obtained numerically and analytically over a wide range of the neck distances between the inclusions. The numerical method turns out to reproduce remarkably well the analytic solutions. In addition, a simple relation between the resistances has been observed in the close neck limit. This relation may be useful in the study of the effective conductivity of a composite in random close packing. The numerical simulation using FEM could be considered a primary step in the study of the effective medium theory for a composite material, especially in a complex geometry.

Chapter 2 CONDUCTIVITY MEASUREMENT OF MICRON-SIZED DIAMOND CRYSTALLITES

2.1 Introduction

2.1.1 motivation

Because of its unique electrical and mechanical properties, diamond attracts much interest these days. It has very wide band gap, high thermal conductivity, and extreme strength as in Table 2.1. Motivated from these concerns, much research has been done on the determination of the electrical properties of this material. Although it behaves similarly in many respects to Si and Ge located in the same column of the periodic table, it has some unique properties compared to these semiconductor materials. However, most studies have been conducted on two-dimensional films because they can be fabricated easily and many important devices are in this form. A diamond film grown on a Si substrate (polycrystalline film) is a mixture of many isolated single crystallites (see Figure 2.1(a)), it includes many local defects (grain boundaries, twins, and dislocations)

Table 2.1 Selected properties of diamond structure semiconductors.

	Band Gap at 300K[3] (eV)	Lattice Parameter at 300K[3] (Å)	Bond Energy (kJ-mol^{-1})[4]	Thermal Conductivity at 300K (W-cm^{-1}-C^{-1})
Diamond	5.47	3.56683	347	24 ~ 25[5]
Si	1.12	5.43095	196	1.5[3]
Ge	0.66	5.64613	163	0.6[3]

that contribute on the transport property of this film. One of these defects in the film is in the form of a bicrystal in Figure 2.1(b). The electric transport in a Si polycrystalline film has been investigated and modeled by the Trap Transistor Model.[6,7] It turns out that the transport in a polycrystalline film is dominated by grain boundaries. The role of these local defects on transport in the diamond film has not been studied rigorously before, because some electric properties of a single crystal are not measured simply due to the complex geometry. Figure 2.2 shows an electron micrograph of typical single crystal that is a well faceted micron-sized diamond.

Usually the determination of the conductivity of a regularly shaped macroscopic sample is straightforward, both in principle and in practice. For a suitable choice of the sample geometry, there is a region where the current flow is uniform and, if the voltage is sampled across this region the measurements are independent of the contact resistances [a so-called 4-terminal measurement] and the resistivity is easily obtained. An example of this is a cylinder in Figure 2.3 with current contacts near both ends and voltage probes

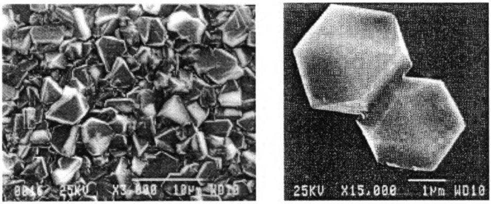

(a) (b)

Figure 2.1 A polycrystalline diamond film (a) and a bicrystal (b) that was formed by two single crystallites.

near the center of the bar. Since this cylindrical conductor has constant area through the current direction, we have a simple relation for resistance R from the geometrical parameters (L, A) by

$$R = \rho \frac{L}{A}, \tag{2.1}$$

where L is length and A is area. If I neglect the contact resistances coming from the 2-terminal measurement, I need to use two extra contacts. The voltage between these two leads is free of a voltage drop across the electrical contacts. However, this approach is not possible for many samples for which regular shapes are difficult to obtain or fabricate, especially in the micron scale. There is a well-known 4-probe method to determine the conductivity in complex geometry, as first suggested by van der Pauw.[8] However, this method requires some restrictions on the geometry of the sample and contact pads. The sample should be a quasi two-dimensional sample. The contacts should be on the circumference of the sample. Therefore, the van der Pauw method cannot be used for the 3d diamond crystallites.

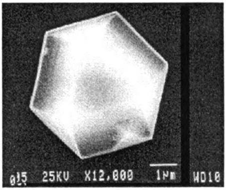

Figure 2.2 A typical shape of CVD diamonds used in this measurement. It is a micron-sized sample grown on a Si substrate.

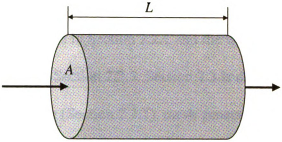

Figure 2.3 The conductivity measurement of a simple shaped sample is usually straightforward. This cylindrical geometry forms constant electric current pattern inside the sample.

I suggest a technique based on the multi-probe measurement of *I-V* characteristics and computer simulation using the finite element method (FEM). This method can be applied to an arbitrary sample geometry under a restriction that the sample is Ohmic. However, the contacts can be non-Ohmic. The diamond samples in this study have been grown by a chemical vapor deposition (CVD) technique on a silicon substrate with boron doping. This technique has been tested on a diamond film, and the conductivity of diamond crystallites has been determined. The conductivity of 3d microcrystallites has been measured and compared with that of a 2d film (especially polycrystalline film). Throughout this chapter, the conductivity of diamond is taken to be isotropic because of its lattice symmetry. Although the determination by this technique has been done on electrically isotropic diamond crystallites, it is a quite general scheme that can be applied to other materials.

In Section 2.1.2, the van der Pauw method is briefly reviewed and compared with our technique. The general idea of the inverse problem and the finite element method (FEM) will be described in Section 2.1.3 and Section 2.1.4. In the following Section 2.2, I will introduce the resistance table from multi-probe measurements (Section 2.2.2) and the geometrical factor will be defined in Section 2.2.1 and the way to consider the contact resistances will be described in Section 2.2.3. Section 2.3 is devoted to computer simulations of image processing (Section 2.3.1), mesh generating and analysis using FEM (Section 2.3.2) and the χ^2 fitting technique to extract the material properties will be described in Section 2.3.3. A brief description of the experimental measurements will follow in Section 2.4. In Section 2.5, we tested this method with the van der Pauw method on a 2d film (Section 2.5.1) and then apply this technique to the data taken from two diamond crystallites and discuss the results (Section 2.5.2). Finally, I summarize the application of the method and give some suggestions in Section 2.6.

2.1.2 van der Pauw formula for 2d film

The determination of the resistivity of a regular shaped conductor is simple because it provides a uniform current inside the sample so that a simple relation between the resistivity and even the Hall coefficient and parameters for the sample shape can be given. However, this is not possible in case where a sample is grown and shaped arbitrarily as in Figure 2.4. A method based on the well-known technique of conformal mapping of two-dimensional fields[9] to measure the resistivity and the Hall coefficient of 2-dimensional films was developed by van der Pauw.[8] This method is very useful to derive those quantities from simple *I-V* measurements and without considering contact resistances between the sample and contacts by using multi-probe measurements.

Suppose we have a flat sample as in Figure 2.4 and the current I_{12} is injected

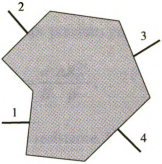

Figure 2.4 The conductivity measurement of 2D film in arbitrary geometry is done by four-probe measurement.

from lead 1 to 2 and the voltage V_{34} between lead 3 and 4 is measured. Then a resistance R_{12}^{34} is defined by V_{34}/I_{12} and it is independent of the contact resistances because there is no current flowing through the leads where the voltage is measured. The resistivity ρ of the sample and 4-point resistances (R_{12}^{34}, R_{23}^{41}) are related by

$$\exp(-\frac{\pi R_{12}^{34} d}{\rho}) + \exp(-\frac{\pi R_{23}^{41} d}{\rho}) = 1, \tag{2.2}$$

where $R_{ij}^{lm} = V_{lm}/I_{ij}$ and d is the thickness of the sample. The resistivity ρ is given by

$$\rho = \frac{\pi d}{\ln 2} \frac{(R_{12}^{34} + R_{23}^{41})}{2} f(\frac{R_{12}^{34}}{R_{23}^{41}}) , \tag{2.3}$$

where f is a function of the ratio R_{12}^{34}/R_{23}^{41} only and has a relation

$$\frac{R_{12}^{34} - R_{23}^{41}}{R_{12}^{34} + R_{23}^{41}} = f \cosh^{-1}\left\{\frac{\exp(\ln 2/f)}{2}\right\} . \tag{2.4}$$

The Hall mobility can be obtained by the change of R_{13}^{24} when a magnetic field is applied perpendicular to the plane. A resistance R_{13}^{24} is given by a cross measurement of voltage and current as done in the usual Hall geometry. If the magnetic induction is B and the resistivity of the sample is known by the previous procedure,

$$\mu_H = \frac{d}{B}\frac{\Delta R_{13}^{24}}{\rho}, \tag{2.5}$$

where ΔR_{13}^{24} indicates a change of the resistance. Usually a *clover-shaped* sample , shown in Figure 2.5(a), is used to eliminate the influence of the contacts. There are some advantages with this shape compared to the *bridge-shaped* sample (Figure 2.5(b)). For low electronic mobility, it provides more Hall current at same amount of heat dissipation. Moreover, it has mechanical strength and can be used for small sample. However, this method works only for a situation that satisfies the following conditions. First, the contacts should be located on the circumference of the sample. Although there are some marginally safe regions inside the sample, for instance near the corners of a square sample, generally this condition should be satisfied.[10] Secondly, the contacts should be small compared to the sample size. This second condition raises trouble in micron-sized

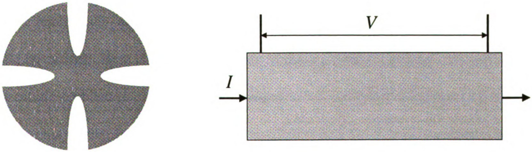

(a) (b)

Figure 2.5 A clover-shaped film (a) and a bridge-shaped film (b) are used for four-probe measurement.

samples. Moreover, the van der Pauw method requires homogeneous thickness of the sample. Following a 2-dimensional approximation, it does not consider any current variation along the perpendicular direction to the plane. Finally, the sample should have a *singly connected* surface. There should not be any hole inside the sample, which generates a separated boundary from the outer surface. With these restrictions, it does not help us to calculate the conductivity of three-dimensional shaped microcrystallites.

2.1.3 inverse problem

All physical problems might be classified into one of two categories, *the direct problem* and *the inverse problem* depending on what is known and what is to be identified in the problem. The term *inverse problem* can be defined simply as the determination of the *causes* from the *results*. It is the opposite to the *direct problem* that determines the *results* from the given *causes* (see Figure 2.6). The direct problem is the determination of some physical quantities (potential, free energy, temperature, current etc.) from the given conditions (geometry, boundary condition, initial condition, and material property). Most analytic problems are usually *direct problems*. To solve a problem analytically, all necessary conditions that cause some physical phenomena should be defined. Here is a simple example of direct problem. Suppose we have an electrostatic problem to obtain voltage distribution in a spherical conductor that has constant charge distribution. This can be done by solving the Poisson's equation with the prescribed conditions (geometry, charge distribution, etc.). Even some numerical simulations are also *direct problems*. One of these examples is molecular dynamics.

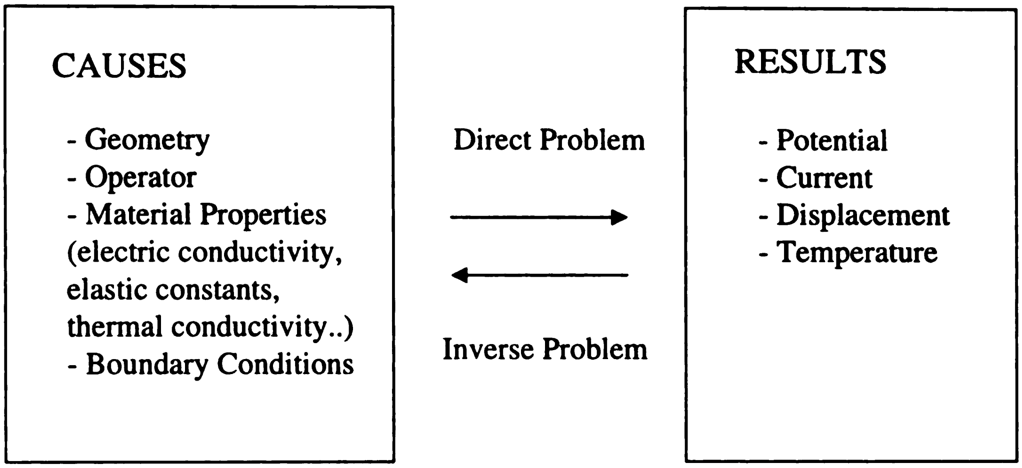

Figure 2.6 A schematic of the *inverse* and *direct* problem. Those two problems can be characterized by what is known and what is determined in the problem.

Consider a system consisting of many particles in a fixed volume. This system at a later time can be described by the initial conditions (potential, initial position and momentum of each particle, etc.). All positions and momenta of the particles at this later time can be given by the simulation. However, some problems are quite different from the *direct problems*. Suppose we determine some physical quantities from experimental data by some fitting procedure. The results (experimental data) are used to find the causes (physical properties). It can be called an *inverse problem*. The fitting is usually performed to identify the unknown causes from the measured results. The optimization technique can be classified by an *inverse problem*. It determines some parameters that minimize the measured quantities (energy, power, χ^2 etc.).

Suppose we have a heat conduction problem as in Figure 2.7. Given a temperature distribution at an initial time $t = 0$, find the temperature distribution on the bar at later time t. This problem is a direct problem because the solution of the

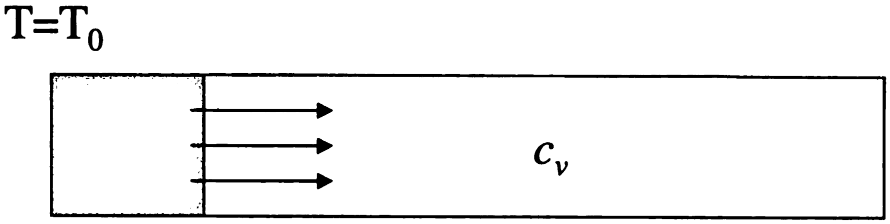

Figure 2.7 Heat conduction problem on a simple bar.

temperature distribution is determined by the initially given conditions. And this problem is a *well-posed* direct problem because the temperature distribution at time t can be determined uniquely from the given conditions (temperature distribution at $t = 0$, heat capacity c_v of bar, and boundary conditions on the surface) and the heat conduction equation governing the analysis.[11] However, if we solve this problem in a different way so that the initial temperature distribution on the bar should be found from the temperature distribution at later time t, it is an *inverse problem*. This problem is an *ill-posed* problem that does not have a unique solution because the temperature distribution function $T(x)$ in all regions of the bar cannot be determined from a finite number of measurements of the temperature distribution at time t. Tikhonov developed a regularization technique to solve a problem that cannot be solved by normal methods like the inversion of linear equations.[12] However, this regularization is not needed for our problem that is a *well-posed* problem. Enough information is available to extract the unknown parameters in our problem. We will determine the conductivity of the sample and the contact resistances where the unknown parameters are fewer than the measured (known) resistances provided by the multi-probe method. In our problem, the *I-V* characteristics of the crystallite can be viewed as *results* and we identify the conductivity and contact resistances as *causes*.

Suppose ϕ is a field variable representing a physical state of the system, which is a response to an applied force f. Then a governing equation can be written as Eq. (2.6) where $L(k)$ is an operator and k denotes material properties of the system.

$$L(k)\phi = f\ , \tag{2.6}$$

The inverse problem is, given the response ϕ, and the applied force f, to determine any missing information involving geometry, operator form, boundary conditions and material properties. Our problem can be more specifically classified as a *material property inverse problem* following the classification of Kubo.[13] He suggested that inverse problems could be classified depending on what quantities to be determined. There are five main inverse problems; *domain/boundary problem* (that includes electric potential computer tomography (CT) method, inversion scheme for electric potential CT method, crack identification), *governing equation* inverse problem, *initial/boundary value* inverse problem, *force inverse* problem, and *material property* inverse problem. In our problem for the determination of the conductivity of a material with a complex geometry by multi probe *I-V* measurement, the applied force f is the current and the response is the potential. We know the form of the operator L defined by the analysis type. The unknown quantity that we need to identify in this problem is the conductivity as a material property.

2.1.4 Finite Element Method (FEM)

Initially the finite element method has been developed for the analysis of structural mechanics because of its excellent applicability to complex geometry analysis. It is a very efficient way to analyze the mechanical property of an object with irregular shape. However, it has been recognized it could be used to solve other problems like electromagnetic, heat conduction, fluid mechanics, acoustics, and piezoelectric studies. This method can be extended to dynamic problems as well as static. There are numerical methods such as finite difference method (FDM), Monte Carlo, spectral, variational method for solving a partial differential equation. However, the finite element method is considered the most efficient for a study in a complicated and highly irregular geometry. Only a few geometries of boundary value problem can be solved analytically even for simple partial differential equations like Laplace's equation. Such geometries might be line, square, circle, sphere, and cylinder. However, most real problems generally have very complicated shapes compared to these simple and ideal structures. Some problems of irregular shapes might be solved by using the perturbation method. Otherwise, it should be approached by successive numerical approximations.

Suppose we solve a boundary value problem as in Figure 2.8 and the inside domain is governed by a partial differential equation

$$\Delta\psi = f \quad , \tag{2.7}$$

where Δ is an operator that may represent Laplace's equation, Poisson's equation ,or heat conduction problem depending on the type of analysis. f can be any type of source as charge, heat source, and so on. The solution ψ, which represents voltage (electromagnetic) or temperature (heat conduction), can be solved by well-defined

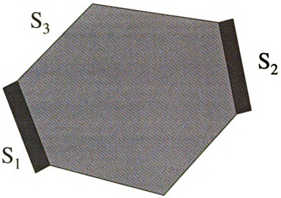

Figure 2.8 A boundary value problem is solved in this irregular geometry. Boundary conditions on each surface are needed.

boundary conditions on the surface of the domain as

$$\psi = \psi_0 \qquad : \textit{Dirichlet} \text{ condition} \tag{2.8}$$

$$\frac{\partial}{\partial n}\psi = \psi_0' \qquad : \textit{Neumann} \text{ condition ,} \tag{2.9}$$

where $\frac{\partial}{\partial n}\psi$ is a normal derivative of ψ. Since our problem is electrodynamic analysis of a diamond crystallite, Laplace's equation should be satisfied inside the region when there is no static electric charge in the sample. We need *Dirichlet* conditions as boundary conditions on the leads (S_1, S_2) where specific voltages are applied. *Neumann* condition on the other surface S_3 with $\psi_0' = 0$ is given as no current flows through the surface. These boundary conditions can be represented by

$$\nabla^2 V = 0 \tag{2.10}$$

$$V = V_0 \text{ on } S_1 \text{ , } V = 0 \text{ on } S_2 \tag{2.11}$$

$$\hat{n} \cdot \vec{E} = 0 \text{ on } S_3. \tag{2.12}$$

2.1.4.1 preprocessor

There are three main procedures in FEM, the *preprocessor*, *analysis*, *postprocessor*. The *preprocessor* generates geometry and initial conditions of the problem. Initial conditions consist of the construction of the geometry, meshes (nodes and elements), boundary conditions, and material properties. In the procedure of geometry reconstruction, we need to have the coordinates of vertices, faces and their connectivity. We developed an algorithm to reconstruct a 3d sample from 2d SEM pictures.[14] The coordinates of the sample vertices obtained by this technique are used to generate the geometry of the computer model in the FEM analysis. This process to build the computer geometry is one of main steps in *the preprocessor*. Some commercial FEM packages including ANSYS provide a CAD type utility for this process. The computer model consists of lines in 1d, areas in 2d and volumes in 3d. The whole domain of the model should be divided into subdomains if different materials are involved in the analysis. Each material is assigned to a given subdomain.

After the construction of the geometry, this whole domain should be meshed into

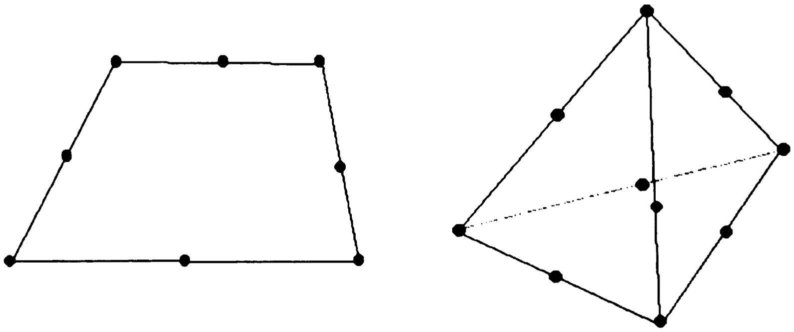

Figure 2.9 Some typical element shapes are presented for FEM. Each element has nodes on the vertices or some extra nodes on the edges to enhance the accuracy.

the *elements*. Each domain of the volume should be meshed separately. These elements are the most important objects in FEM, where the analysis is performed inside. Each element is defined by *nodes*, *lines*, and *facets* as in Figure 2.9. Elements can be lines in 1d, triangles, squares, honeycombs in 2d, and tetrahedras, cubes in 3d. However, highly distorted elements as in Figure 2.10 are not recommended because they may cause serious numerical errors in simulation. Following the defined shapes and sizes of elements, the whole domain can be covered by the elements as shown in Figure 2.11. Apparently finer meshes can generate more realistic shape for a complex structure and can enhance the accuracy of the simulation. However, many meshes increase degrees of freedom so that the performance of the simulation would be limited by the computing power. A spherical object is one of the most complicated structures to mesh well. All boundaries of elements are defined by a line segment in 2d, plane in 3d. A curve in 2d or a curved plane in 3d cannot be used for the boundaries of the elements. A circle in 2d can be meshed only into a polygon. It may cause a serious problem in the numerical analysis of two adjacent circles. Except for these extreme structures, the meshing itself is not so

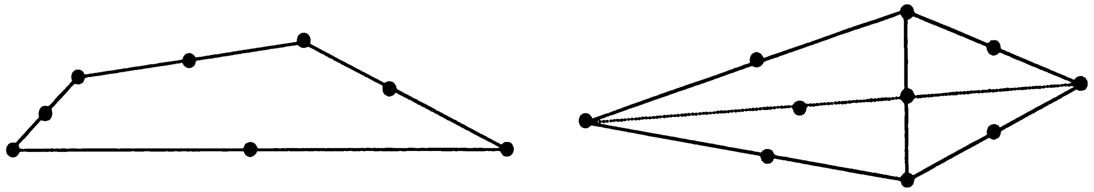

Figure 2.10 Highly distorted elements are not usually acceptable in mesh generating.

Figure 2.11 A sample of meshed geometry with square-shaped elements in 2d.

important in the numerical simulations. The meshing generates the coordinates of all nodes and defines the topology of each element defined by these nodes. This information is moved into the next stage of analysis.

2.1.4.2 analysis

In the analysis procedure, a function is defined inside each element. As mentioned earlier, since the physical quantities in the problem are represented only on the nodal points at the boundaries of elements, they are not defined yet inside the elements. We express the physical quantities (voltage, displacements, etc.) in terms of the functions whose magnitudes are defined on the nodal points. This function is interpolated to generate physical quantities inside the elements. This property is the main difference with the finite difference method (FDM), which is very similar to the FEM in many aspects. All variables, including first and second derivatives of the physical quantities, can be obtained by the interpolation of this function inside the elements.

The next equation is one example of this function defined by the basis function ϕ_i.

$$\psi = \sum_{i=1}^{q} \phi_i u_i \tag{2.13}$$

where ϕ_i is a known basis function and u_i is an unknown coefficient (Ritz coefficient).[15,16] We have q unknown coefficients here. In FEM, the basis functions are selected to calculate the physical values inside the elements. Then all values in the whole domain can be represented by the coefficients and the physical quantities on each node. The global potential energy is represented by the sum of the local potential energy defined for each element. The variational principle is applied to find out the values of ψ on the nodes. By solving for the coefficients in the above equation, we can construct the functional ψ and obtain the physical quantities in the whole region. One choice for the basis functions is orthogonal polynomials. The degree of the polynomials is an option to enhance the efficiency of the analysis. However, the increase of the degree of the polynomials means the increase of degrees of freedom so that it causes a memory problem in computing. We have a trade off here between the accuracy of the simulation and the limit of computing power. This trouble happens similarly in the mesh generation as mentioned in the previous section. The finer mesh gives a better result, but it increases the number of nodes where each functional ψ is defined. After setting up the functionals of the physical variable, we solve the boundary value problem inside the elements. That means we have the equations of the unknown coefficients by solving the differential equation and applying the boundary conditions between the elements and their adjacent elements. The boundary conditions should be the continuity relations of the physical quantities around the boundary of the elements. The first derivative of the variable also should be continuous. For instance, the voltage and electric field on the boundary between two finite elements should be continuous. Then, the potential energy of each element is represented by the unknown coefficients and combined together for the global potential energy Π as in

$$\Pi = \int \Phi du \approx \sum_{j=1}^{n} \Phi_j (u_i^j) \ . \tag{2.14}$$

The variational principle should be applied to minimize the potential energy functional Π. The unknowns are the nodal point variables that are related to the unknown coefficients in Eq. (2.13). The global function Π would be the electric power in electrodynamics, potential energy in electrostatic, heat dissipation in heat conduction, and elastic potential energy in the structural mechanics. In the variational method, the functional should satisfy the minimization condition of

$$\frac{\partial \Pi}{\partial u_i} = 0 \ , \quad i = 1,..,n \tag{2.15}$$

where the approximate solution is given by

$$\mathbf{u}^n = \sum_{i=1}^{n} f_i a_i \ , \tag{2.16}$$

where f_i is a Ritz function equivalent to a basis function and a_i is a Ritz parameter. In this procedure, the correct boundary conditions of $\mathbf{u}^n$ should be applied on the surfaces and the differential equation should be satisfied inside the complete domain. By solving the minimization method, the physical quantities on all nodes and the unknown coefficients (Ritz parameters) are determined. Those values generate a complete solution for the whole region.

2.1.4.3 postprocessor

In last step of postprocessor, a complete solution has been obtained for the whole region. Since each variable on the node is given by the analysis, values inside the elements can be determined by the interpolation of the functional in Eq. (2.13). From the given quantities on the nodes, we can calculate other information. For instance, we solve the electric conduction problem using only one variable that is voltage. However, after the voltage on each node is obtained from the analysis, the current flow can be calculated from the electric field and the conductivity of the material. The postprocessor provides the visualization of the results by the interpolation technique; the contour map of voltage, current, stress and strain distributions as presented in Figure 2.12. This is a very useful and fast way to check if the simulation works well. More detail about FEM can be

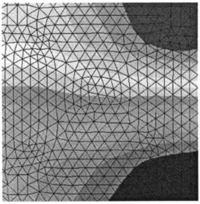

Figure 2.12 By the FEM analysis, a voltage distribution on a sample is obtained. The interpolation technique is used to obtain the distribution inside the elements.

found in other references.[17, 18, 19]

2.2 Theory

2.2.1 conductivity and geometrical factors

For a complicated geometry, the conductivity cannot be determined directly from the measurement of the resistances since we measure the voltage and current that depend on the geometry. We cannot separate the conductivity (geometry independent) from a resistance (geometry dependent). Thus, we define a geometrical factor that only depends on the geometry to treat the conductivity separately from the resistance. At this moment, the contact resistances are neglected. The way to treat contact resistances (Ohmic and non-Ohmic) will be described later in Section 2.2.3.

When we measure the voltage V and current I in a sample like Figure 2.13, a resistance is defined by

$$R=\frac{V}{I}=\frac{\int \vec{E}\cdot d\vec{l}}{\int \vec{J}\cdot d\vec{S}}=\frac{\int \vec{E}\cdot d\vec{l}}{\sigma\int \vec{E}\cdot d\vec{S}}=\frac{1}{\sigma}\Gamma=\rho\Gamma \quad , \tag{2.17}$$

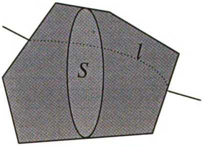

Figure 2.13 For 2-terminal measurement, the voltage is calculated by a line integral along the path l and the current is obtained by a surface integral on the cross section S.

where we assumed the conductivity tensor is isotropic; otherwise σ can not be taken out the integral. A newly defined quantity $\Gamma = \int \vec{E} \cdot d\vec{l} \, / \int \vec{E} \cdot d\vec{S}$ in this relation depends on the geometry only, not on the absolute value of the conductivity.

Suppose we have a sample with four probes as in Figure 2.14, 36 resistances can be defined from six measurements of voltage and six measurements of current. We can represent each resistance with a corresponding quantity Γ defined in Eq. (2.17). From a voltage between two leads *l*, *m* and a current through *i*, *j*, a resistance R_{ij}^{lm} is defined in the same manner.

$$R_{ij}^{lm} = \frac{V_{lm}}{I_{ij}} = \frac{\int_l^m \vec{E} \cdot d\vec{l}}{\int_i^j \vec{J} \cdot d\vec{S}} = \frac{\int_l^m \vec{E} \cdot d\vec{l}}{\sigma \int_i^j \vec{E} \cdot d\vec{S}} = \rho \Gamma_{ij}^{lm} \tag{2.18}$$

We call the quantity Γ_{ij}^{lm} defined in Eq. (2.18) a *geometrical factor*. By defining this

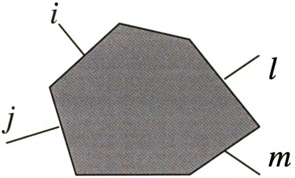

Figure 2.14 Showing a conductor that has four probes that are attached on the surface.

geometrical factor, the conductivity (which is a constant as an intrinsic material property) can be separated from the resistance. This geometrical factor Γ is given by L / A for a simple geometry of cylindrical shape, where L is a length and A is a constant area. However, in most cases it can not be obtained by this simple form because of complicated geometry that induces a complicated non-uniform current pattern. Following this definition in Eq. (2.18), each resistance has its corresponding geometrical factor with the conductivity as a scale factor. These geometrical factors can be given by a numerical simulation described in Section 2.1.4 using unit conductivity. These calculated geometrical factors will be used later to determine the conductivity by fitting with resistances given by the experimental measurement.

2.2.2 resistance table and its properties

In a multi-probe measurement, we can define many different configurations for the resistance measurement depending on how to choose the leads for voltage and current measurement. All possible measurements provide a set of resistances that forms a matrix, a so called *resistance table*.

One of the diamond crystals (Sample 2) with contact pads prior to lithographic lead attachment is presented in Figure 2.15. In a normal multi-probe measurement, contacts are attached on the surface of a sample and the I-V characteristics are measured. At least four contacts are needed to obtain contact-free resistances. Although we have five pads on the surface in this sample, four of the five pads were used for the measurement, with the furthest to the left having no lead attached. This pad was at a

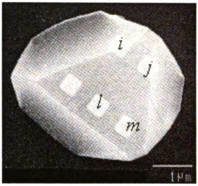

Figure 2.15 Micron-sized diamond crystal grown by a chemical vapor deposition technique before Au leads were attached. Five titanium contacts were formed on the surface and four of them (indexed) were used for the measurement.

constant (but initially unknown) potential that was determined by the finite element code. With the four probes for the *I-V* measurement, a set of resistances can be given by all possible voltage and current measurements. This set is called a ***resistance table*** that has all necessary information of the sample conductivity and contact resistances. A current I_{ij} flows through the terminal *i*, *j* and a potential difference V_{lm} is measured across terminal *l*, *m*. We can define a (signed) resistance $R_{ij}^{lm} = V_{lm} / I_{ij}$, which reduces to the standard definition of resistance (2-terminal resistance) when $i, j = l, m$. With this definition of resistance, we can generate a resistance matrix as Table 2.2 formed by V_{lm} column and I_{ij} row for all possible combinations. This set of measurement forms a ${}^nC_2\,(= n(n-1)/2)$ by ${}^nC_2$ resistance matrix of all possible pairs of current terminals and voltage terminals but there are only ${}^nC_2$ independent elements in this matrix because of the following constraints. For an Ohmic sample, the matrix is symmetric under the exchange of current and voltage terminals, i.e.

Table 2.2 A resistance table from all possible combinations of voltage and current measurements.

R_{ij}^{lm}	V_{12}	V_{13}	V_{14}	V_{23}	V_{24}	V_{34}
I_{12}	R_{12}^{12}	R_{12}^{13}	R_{12}^{14}			
I_{13}		R_{13}^{13}	R_{13}^{14}			
I_{14}			R_{14}^{14}			
I_{23}				R_{23}^{23}		
I_{24}					R_{24}^{24}	
I_{34}						R_{34}^{34}

$$R^{ij}_{lm} = \frac{V_{ij}}{I_{lm}} = R^{lm}_{ij} = \frac{V_{lm}}{I_{ij}} \ , \tag{2.19}$$

where V_{ij} is the voltage between the leads i, j and I_{lm} is the current between the leads l, m. This is a *reciprocity theorem*,[20] which is proved in the Appendix A.1 for the present geometry. Along any row of the resistance matrix, the current I_{lm} is a constant, and the voltage is a scalar potential that satisfies

$$V_{ij} = V_{ik} + V_{kj} \ . \tag{2.20}$$

Thus, the resistance elements have the additive property

$$R^{ij}_{lm} = \frac{V_{ij}}{I_{lm}} = \frac{V_{ik} + V_{kj}}{I_{lm}} = R^{ik}_{lm} + R^{kj}_{lm} \ . \tag{2.21}$$

Using these two rules, we can show that there are only ${}^{n}C_2$ independent elements in the resistance matrix by the following construction:

Consider the $n-1$ elements (R^{1i}_{12}, $i = 2,..,n$) in the first row of the resistance matrix. These terms can generate all the other elements in this row using the addition rule

$$R^{ij}_{12} = R^{1j}_{12} - R^{1i}_{12} \ , \tag{2.22}$$

where $i < j = 2,..,n$. Note that changing the order of the indices changes the sign of the resistance. In the second row, only $n-2$ elements of R^{1i}_{13} ($i = 3,..,n$) are needed to construct the remaining elements in that row because, by the reciprocity theorem, $R^{12}_{13} = R^{13}_{12}$ and R^{13}_{12} was given in the first row. Continuing in this manner we need $n-1$ terms in the first row, $n-2$ terms in the second row, for a total of

$$(n-1)+(n-2)+....+2+1=\frac{n(n-1)}{2}={}^{n}C_2 \tag{2.23}$$

independent elements. There are many possible choices of the ${}^{n}C_2$ independent elements, but they cannot be selected arbitrarily. By the above construction, the $(n-1)$ by $(n-1)$ upper diagonal block forms one independent set. Surprisingly, the ${}^{n}C_2$ diagonal elements (the set of 2 terminal elements) also form an independent set, related to the off diagonal elements by

$$R_{ij}^{lm}=\frac{R_{jl}^{jl}+R_{im}^{im}-R_{jm}^{jm}-R_{il}^{il}}{2}\ . \tag{2.24}$$

This relation means that knowledge of only the 2-terminal measurements can be used to generate the complete resistance matrix, which can be used as a useful self consistency-check on the experimental results. Table 2.3 shows how the diagonal terms reconstruct the whole resistance table. Three off-diagonal terms in the triangular matrix in the bold box can be obtained from the six diagonal terms by Eq. (2.24). Six terms in the bold box was already shown to generate the whole matrix in Table 2.3. In Table 2.4, I summarized how the number of elements of the resistance matrix, and the number of independent elements depend on the number of terminals. We need at least four terminals to extract the resistivity ρ and the contact resistances because otherwise there are more unknowns than independent terms.

As an example, consider the case for four terminals ($n=4$) shown in Table 2.4. There are six ways to select two of four terminals and so there is a 6 by 6 resistance matrix with six independent elements. The six diagonal elements form the most

Table 2.3 How to generate the triangular matrix from six diagonal terms so that the triangular matrix produces a whole table

R_{ij}^{lm}	V_{12}	V_{13}	V_{14}	V_{23}	V_{24}	V_{34}
I_{12}	R_{12}^{12}	$\frac{R_{12}^{12}+R_{13}^{13}-R_{23}^{23}}{2}$	$\frac{R_{12}^{12}+R_{14}^{14}-R_{24}^{24}}{2}$			
I_{13}		R_{13}^{13}	$\frac{R_{13}^{13}+R_{14}^{14}-R_{34}^{34}}{2}$			
I_{14}			R_{14}^{14}			
I_{23}				R_{23}^{23}		
I_{24}					R_{24}^{24}	
I_{34}						R_{34}^{34}

Table 2.4 The number of independent elements in a resistance table.

Number of Terminal	Dimension of Resistance Table	Elements in Resistance Table	Independent Elements	Unknowns (ρ , contact resistances)
2	1	1	1	3
3	3	9	3	4
4	6	36	6	5
5	10	100	10	6
6	15	225	15	7
:	:	:	:	:
n	${}^{n}C_2 = n(n-1)/2$	$[{}^{n}C_2]^2$	${}^{n}C_2 = n(n-1)/2$	$n+1$

important set of independent elements from which we can use Eq. (2.24) to obtain the three off-diagonal terms, R_{12}^{13}, R_{12}^{14}, R_{13}^{14} as shown in Table 2.3. The 3 x 3 upper diagonal block (shown inside the bold line in Table 2.2 and Table 2.3) is an alternative independent set that can be used to construct the entire matrix using the procedure outlined above. However, it is interesting to note that the set of 4-terminal measurements is not all independent. Note that by Eq. (2.24), only two of the 4-terminal elements are independent with

$$R_{13}^{24} = R_{14}^{23} + R_{12}^{34} \ . \tag{2.25}$$

As a result, a set of six terms including three 4-terminal measurements *cannot* be used to reconstruct the whole resistance table.

It is important to note that the above analysis is only true for samples where the *I-V* curve is independent of the current direction (otherwise the reciprocity theorem fails).[20, 21] Some of the experimental data analyzed in Section 2.5.3 has non-Ohmic characteristics indicated by asymmetry of a table, and so the resistance matrix has more than 6 independent elements. The necessary modifications to the above analysis are model dependent, and will be discussed for the specific situation of the experiment.

2.2.3 contact resistances

In two previous sections, it has been found that the geometrical factors separate the unknown conductivity from a resistance. However, the contact resistances should be considered in 2-terminal and 3-terminal resistances. The measured resistances include the contact resistances, so the representation of the resistances should be modified. We

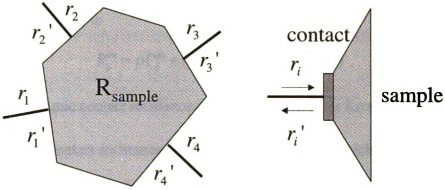

Figure 2.16 Contact resistances have two different values (r_i, r_i') for non-Ohmic contacts. A resistance measurement consists of a sample resistance R_{sample} and contact resistances added in series.

Table 2.5 Resistance table with two contact resistances for current flows.

R_{ij}^{lm}	V_{12}	V_{13}	V_{14}	V_{23}	V_{24}	V_{34}
I_{12}	$\rho\Gamma_{12}^{12} + r_1 + r_2'$	$\rho\Gamma_{12}^{13} + r_1$	$\rho\Gamma_{12}^{14} + r_1$	$\rho\Gamma_{12}^{23} - r_2'$	$\rho\Gamma_{12}^{24} - r_2'$	$\rho\Gamma_{12}^{34}$
I_{13}	$\rho\Gamma_{13}^{12} + r_1$	$\rho\Gamma_{13}^{13} + r_1 + r_3'$	$\rho\Gamma_{13}^{14} + r_1$	$\rho\Gamma_{13}^{23} + r_3'$	$\rho\Gamma_{13}^{24}$	$\rho\Gamma_{13}^{34} - r_3'$
I_{14}	$\rho\Gamma_{14}^{12} + r_1$	$\rho\Gamma_{14}^{13} + r_1$	$\rho\Gamma_{14}^{14} + r_1 + r_4'$	$\rho\Gamma_{14}^{23}$	$\rho\Gamma_{14}^{24} + r_4'$	$\rho\Gamma_{14}^{34} + r_4'$
I_{23}	$\rho\Gamma_{23}^{12} - r_2$	$\rho\Gamma_{23}^{13} + r_3'$	$\rho\Gamma_{23}^{14}$	$\rho\Gamma_{23}^{23} + r_2 + r_3'$	$\rho\Gamma_{23}^{24} + r_2$	$\rho\Gamma_{23}^{34} - r_3'$
I_{24}	$\rho\Gamma_{24}^{12} - r_2$	$\rho\Gamma_{24}^{13}$	$\rho\Gamma_{24}^{14} + r_4'$	$\rho\Gamma_{24}^{23} + r_2$	$\rho\Gamma_{24}^{24} + r_2 + r_4'$	$\rho\Gamma_{24}^{34} + r_4'$
I_{34}	$\rho\Gamma_{34}^{12}$	$\rho\Gamma_{34}^{13} - r_3$	$\rho\Gamma_{34}^{14} + r_4'$	$\rho\Gamma_{34}^{23} - r_3$	$\rho\Gamma_{34}^{24} + r_4'$	$\rho\Gamma_{34}^{34} + r_3 + r_4'$

assume these contact resistances can be added *in series* to the sample resistance because the contact area is assumed an equipotential due to the high conductivity of the Au/Ti contact pads. This leads to

$$R_{ij}^{lm} = \rho\Gamma_{ij}^{lm} + r_i(\delta_{il} - \delta_{im}) + r_j(\delta_{jm} - \delta_{jl}) \ , \tag{2.26}$$

where r_i is the Ohmic contact resistance of terminal *i* and δ_{ij} is Kronecker delta function.

However, contact resistances are generally non-Ohmic which is indicated by non-symmetric three terminal elements in the observed resistance table. We assume that the sample itself is Ohmic, which is justified if the four terminal elements are symmetric. Since the *I-V* characteristics are non-linear and not symmetric for non-Ohmic behavior of the contacts, each contact has two independent resistances for the two different current directions [i.e. current reversal with the magnitude of the current held constant]. To investigate such non-Ohmic *I-V* characteristics of a contact, we used two fitting parameters, r_i, r_i' corresponding to the two contact resistances for constant current flow as in Figure 2.16. If r_i is a contact resistance when a current is flowing *into* the sample and r_i' is for a current flowing *out* of the sample, then Eq. (2.26) is modified to become

$$R_{ij}^{lm} = \rho\Gamma_{ij}^{lm} + r_i(\delta_{il} - \delta_{im}) + r_j'(\delta_{jm} - \delta_{jl}) \tag{2.27}$$

to be a more general expression for non-Ohmic contacts. The whole expression of the resistance table following the relation of Eq. (2.27) is given in Table 2.5.

2.3 Computer Simulation

2.3.1 reconstruction of 3d computer image

In FEM, all the information of the sample geometry is needed for the preprocessor that constructs a computer model for the analysis. It may include the coordinates and topology of all vertices, lines, planes, and volumes associated with the sample shape. However, since our samples are micron-sized crystals, it is not straightforward to measure the shape of such small objects. One way is using electron lithography to get the SEM (Scanning Electron Microscope) photos. An *inverse ray tracing* technique is used to reconstruct the three dimensional object that will be used in simulations. *Ray tracing* is a computer process used to create a two dimensional representation of a three dimensional object by tracing the path of the ray of light between the light source, objects, and an observer.[22] We apply this technique *in reverse* to construct a three dimensional image from the two-dimensional SEM photos. Since these photos were only two dimensional, we needed several pictures taken along different

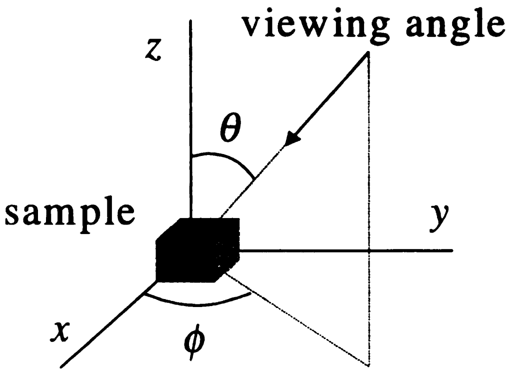

Figure 2.17 Each SEM photo is given in an orientation for viewing angle (θ, ϕ) as shown in this figure.

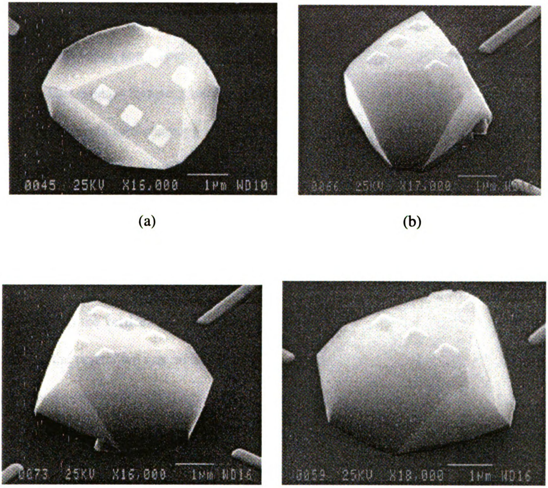

(a) (b)

(c) (d)

Figure 2.18 SEM photos of a sample (Sample 2) in various orientations. (a) $\theta, \phi = 0°, 0°$ (b) $\theta, \phi = 50°, 0°$ (c) $\theta, \phi = 50°, 90°$ (d) $\theta, \phi = 50°, 270°$

orientations defined by viewing angles in Figure 2.17. Figure 2.18(a)~(d) present four different pictures projected in each direction before gold leads are attached on the five contacts formed on the surface. In this sample, contacts were located on the upper surface since it has been formed by the electron beam along the vertical direction. Therefore, the picture in Figure 2.18(a) taken along the same direction shows most of the detailed geometry. However, some contacts were observed smeared down the surface (see Figure 2.18(c)). This contact formed a wide contact area that could affect the *I-V* measurements. For a more complicated contact formation or some serious deformations in the lower part, it is necessary to select all viewing angles carefully to take the whole geometry of the sample. After taking these SEM pictures, the coordinates of all vertices of the sample and contacts were digitized on each photo.

The algorithm treats the crystal as an irregular polyhedron and attempts to assign coordinates to the vertices in a way that is consistent with the SEM images. From each picture of the crystal we can measure the *projected* length of an edge of the diamond crystal, and compare it with the projected length calculated from the assumed vertex coordinates. The vertex coordinates are adjusted to minimize

$$\chi_l^2 = \sum_i \left[\frac{l_i - l_i^{SEM}}{\sigma_i^l}\right]^2, \qquad (2.28)$$

where l_i is a calculated projected length, l_i^{SEM} is the projected length from the SEM and σ_i is an estimate of the experimental error in measuring l_i^{SEM}. The sum is over all edges visible in each picture, and over all pictures. The positions of the contact pads are determined by including the coordinates of the corners of the contact pads, and the lengths from the corners to some of the crystal vertices. Taking pictures from enough different orientations to ensure that every edge was visible in at least two images was adequate to ensure that we could construct a representation of the sample that matched the SEM images very well. Because we knew that the sample was a single crystal, we added some additional constraints to the minimization process. Specifically we required the facets to be planar, and the facet angles to conform to the known facet angles of the diamond structure, e.g. 70.5° or 109.4° between different (111) facets. The flatness constraint was achieved by adding to χ^2 the term

$$\chi_p{}^2 = \sum_i \sum_j \left[\frac{\vec{c}_i \cdot (\vec{r}_{ij} - \vec{c}_i)}{\sigma_i^p} \right]^2 , \qquad (2.29)$$

where $\vec{r}_{ij}$ denotes j-th vertex coordinate in i-th facet and $\vec{c}_i$ is a constant vector that is normal to the i-th plane. The facet angles are constrained by adding to χ^2 a term

$$\chi_f{}^2 = \sum_i \left[\frac{\theta_i - \theta_i^{theory}}{\sigma_i^f} \right]^2 , \qquad (2.30)$$

where the facet angles θ_i^{theory} are those appropriate for a diamond structure. The sum is over pairs of facets. The σ_i^p in Eq. (2.29) and σ_i^f in Eq. (2.30) are standard deviations denoting the weighting factors for each constraint. Although it is arbitrary how these factors are assigned, they should be larger than the standard deviation associated with the edge lengths l_i because these lengths could be determined very easily and directly from the SEM photographs.

$$\chi^2 = \chi_l{}^2 + \chi_p{}^2 + \chi_f{}^2 . \qquad (2.31)$$

The total χ^2, the sum of the three quantities in Eq. (2.28)~ (2.30) is minimized by adjusting the vertex coordinates using a standard non-linear minimization routine.[23] The final coordinates associated with the minimized χ^2 were used as the input for the current flow analysis that was done using the finite element method.

After this optimization procedure, we obtained a computer model of the sample. It provided all information about the geometry defined by the coordinates of vertices and the connectivity of planes and volumes. Nearly 80 vertices were needed in our models and most vertices were for the contacts. The contact areas have been constructed very carefully since the transport in the sample mostly depends on the area. By initially assigning high conductivity to the contacts, the contribution of the contacts to the resistance measurements was determined only by the effective area for the current flow. We attached five contact pads in the shape of small pyramids on the sample as in Figure 2.19. Although only four contacts of five were used for the real measurement, we made the fifth contact also to generate the equipotential area below the contact. Figure 2.19(a) and (b) shows two views of the computer model (Sample 2), which correspond to the

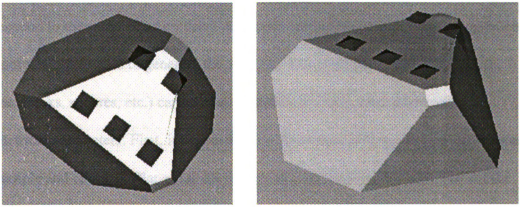
(a) (b)

Figure 2.19 Computer images reconstructed from SEM photos by image processing. Five small pyramids on the surface denote five contacts. Compare these two images with the SEM photos in the Figure 2.18.

SEM image in Figure 2.18(a) and (d) respectively. It was not possible to observe the bottom of a sample because of the Si substrate. Some diamond crystallites may have an unusual structure of local defect below that cannot be identified in the SEM photos. However, usually it does not contribute significantly to the transport as much as the top part of the sample does. On the surface near the contact pads, a large variation of current flow was observed. However, it was not so on the surface below where no contact pads were formed.

2.3.2 modeling and analysis using FEM

2.3.2.1 modeling (preprocessor : ANSYS)

After the geometry reconstruction, I did the simulation using the finite element method to solve the electrical conduction problem. All FEM tasks in this problem were performed by the commercial packages ANSYS[24] and ABAQUS[25]. ANSYS 6.1 was used for a preprocessor (mesh generating) and the other processes (numerical analysis and post processor) were done by ABAQUS 5.5. In modeling by ANSYS, I generated volumes that correspond to the sample and contacts. Since our sample had highly irregular geometry, it was not straightforward to generate the structure. Some simple structures (squares, circles, bricks, spheres, etc.) can be constructed by giving a few coordinates and geometrical parameters. First, it begins with the formation of keypoints for all vertices of the sample and contacts. Planes for the volume construction are made by linking the keypoints that are associated with a plane. Some vertices of a plane may not be located on the same plane even after the geometry optimization with the constraint of a flat plane. ANSYS does not allow making a plane by linking these vertices. All keypoints should be

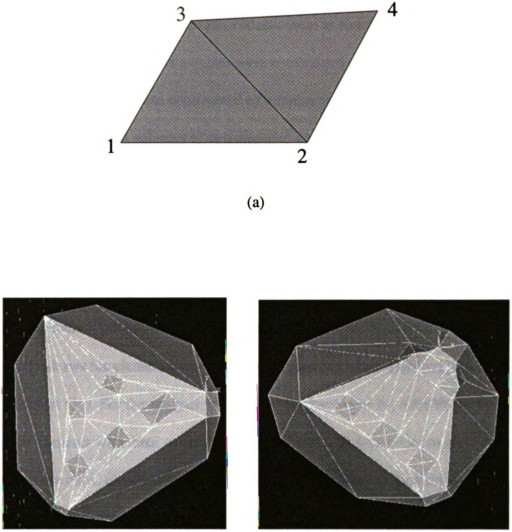

(a)

(b) (c)

Figure 2.20 Triangular planes generated from three keypoints were combined into a large plane as shown in (a). A volume could be constructed by connecting these large planes into a volume unit. The volume elements for the diamond crystallites were presented in (b) and (c).

on the same plane to construct a plane. Thus, a triangle plane was used to overcome this trouble. Suppose we need to make a plane structure by four vertices (1, 2, 3, 4) in Figure 2.20(a) and the vertex 4 is not on the plane defined by the other three vertices (1, 2, 3). Then we make two triangular planes and connect them to form a folded plane made of four vertices. Most planes in our samples were constructed in this way as shown in Figure 2.20(b) and (c). A volume was constructed by combining these planes. Figure 2.20(b) and (c) present the structured volumes of two diamond crystallites before the meshing. Both of our samples consisted of six separated volumes (one huge volume for the sample and five small pyramids for the contact pads). Different material properties could be assigned to the separated volumes in the FEM analysis.

After constructing these volumes, we need to select the type of element for the meshing. Element types are selected depending on the dimension and the analysis type. Figure 2.21 shows the element shapes used in the meshing of the diamond film (2d) and the crystallites (3d). For the analysis of electrical conduction in 2d, ANSYS provides triangular elements with three or six nodes and squares with four nodes or eight nodes. In 3d, we can use cubic elements with 8 or 20 nodes and tetrahedral elements with 4 or 10 nodes. Tetrahedral elements were usually used to mesh an irregular shape in 3d where it was not done by cubic elements. Tetrahedral elements with four nodes were used for the diamond films and one diamond crystallite (Sample 1) and tetrahedral elements with 10 nodes were used for the other diamond crystal (Sample 2). The diamond film was meshed by square elements (2d) as well as tetrahedral elements (3d) to test whether the 2d approximation of the film was valid in the simulation. Figure 2.22 shows the meshed structures of all samples; a diamond film(a) and crystallites ((b) and (c)).

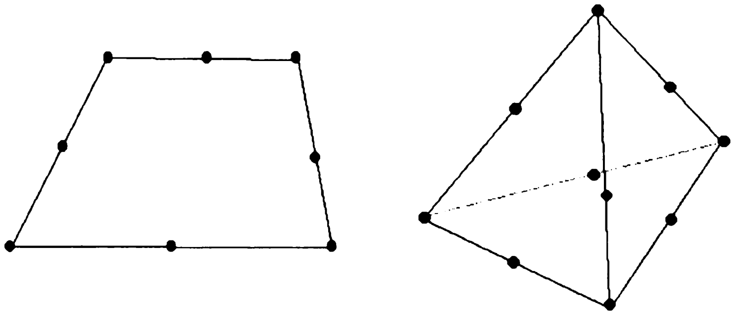

Figure 2.21 The elements used for the meshing of 2d film (square) and 3d crystallites (tetrahedra). Sometimes elements that have only four nodes on the corners were used.

Table 2.6 The characteristics of the meshings for each sample.

	Homoepitaxial films	Sample 1	Sample 2
Element type	DC3D4	DC3D4	DC3D10
Nodes per elements	4	4	10
Total Nodes	800	1100	4700
Number of elements	2300	5500	3300

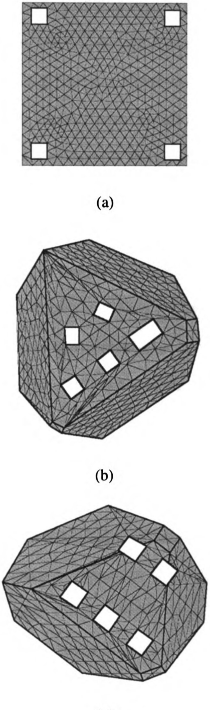

(a)

(b)

(c)

Figure 2.22 Meshed structures of the diamond film(a) and crystallites (Sample 1(b), Sample 2 (c)). Figure 2.20(b) and (c). Each model has square-shaped contacts on the surface.

2.3.2.2 analysis (processor : ABAQUS)

The meshed structures given by ANSYS were delivered to ABAQUS for the analysis. All coordinates of nodes and the topology of elements were used to generate an ABAQUS input file that includes all necessary information for the analysis; material property, boundary conditions, and output format as well as the geometry. Since ABAQUS does not provide the electromagnetic analysis, the heat conduction analysis was used. Both analyses follow the same differential equation, Laplace's equation with no charge and heat source. The temperature in the heat conduction analysis is equivalent to the voltage in the electric conduction analysis. The heat flux and the thermal conductivity correspond to the current and the electric conductivity respectively. By these correspondences, the electric conduction problem could be solved by the heat conduction analysis using ABAQUS. In the heat conduction analysis, the temperature is the only degree of freedom that is defined on each node. By minimizing the heat dissipation defined by the temperature, the solution on each node could be obtained under the subscribed boundary conditions and the material properties. After the temperatures on every node were obtained, the heat flux could be determined from the derivatives of the temperature functions and the thermal conductivity. An electric resistance could be defined by the temperature (voltage) and the heat flux (current). Some details of these procedures were described earlier in Section 2.1.4.2 and the rest can be found in some other references or ABAQUS manuals.[25]

Our main object in this analysis is to obtain the geometrical factors, not resistances. They represent the shape factors that are not related to the intrinsic material property (conductivity). To obtain these factors in this analysis, unit conductivity is given to the conductor. Then, the resistances calculated from the voltage and current given are equivalent to the geometrical factors Γ_{ij}^{lm}. In the *absence* of any contact resistances, these factors are related to the resistances R_{ij}^{lm} by a simple linear relation of

$$R_{ij}^{lm} = \rho \Gamma_{ij}^{lm} \ . \tag{2.32}$$

All possible combinations of the current and voltage measurements generate a 6 by 6 *geometrical factor table*. These geometrical factors include any information of complex current paths across the arbitrarily shaped sample for each combination.

2.3.2.3 contour map (postprocessor : ABAQUS)

From the analysis in the previous section, the voltages only on the nodes were obtained. Inside the elements, the equipotential lines were calculated from the interpolated functions of the voltage. The contour maps of the voltage distributions on the sample surfaces are shown in Figure 2.23 for a selected configuration of the current and voltage measurement. The current flows from the red pad (high potential) to the blue pad (low potential). The voltage distributions are indicated by the contour map. Figure 2.23(a) presents the potential distribution on the surface of a film. Figure 2.23(b) and (c) present the potential distribution of a crystal (Sample 1) viewed by different orientations. Figure 2.23(d) and (e) show the similar contour maps of another crystal (Sample 2). Figure 2.23(b) and (d) were viewed by the vertical direction (view point =(0, 0, 1)) and Figure 2.23(c) and (d) were rotated and shown by a different view point (1, -1, 1). By assigning high conductivity ($> 10^6$) to the contacts and unit conductivity to the sample, the contour

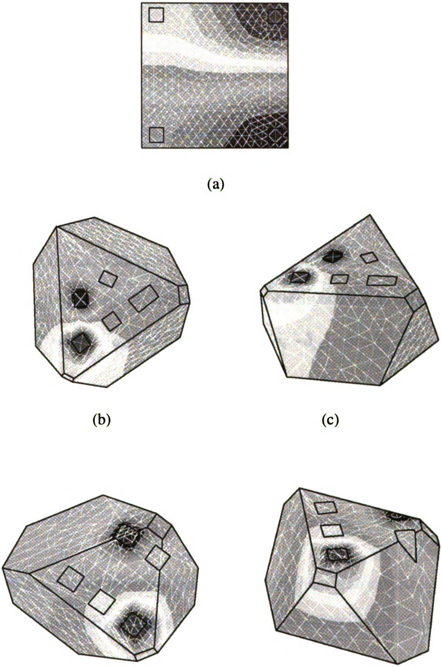

(a)

(b) (c)

(d) (e)

Figure 2.23 Equipotential lines on the surface of the samples given by ABAQUS. (a) is for homoepitaxial film. (b) (c) are for Sample 1. (d),(e) are for Sample 2. The figures of 3d samples were obtained in different orientations.

maps show the constant potential distributions on all contact areas including the lead-free contact as expected.

2.3.3 least square fitting

Table 2.5 in Section 2.2.3 is a modified resistance table for a 4-terminal problem showing each element in terms of the sample resistivity ρ, the geometric factors Γ_{ij}^{lm} and 6 of the 8 contact resistances (r_1, r_2, r_2', r_3, r_3', r_4').[26] Another table for reverse current flows is necessary to extract all the contact resistances for non-Ohmic contacts. From these two tables given by opposite current directions, a resistance can be defined as

$$R_{ij}^{lm} = \rho\Gamma_{ij}^{lm} + \bar{r}_i(\delta_{il} - \delta_{im}) + \bar{r}_j(\delta_{jm} - \delta_{jl}) + \Delta r_i(\delta_{il} - \delta_{im}) - \Delta r_j(\delta_{jm} - \delta_{jl}) \qquad (2.33)$$

where

$$\bar{r}_i = \frac{1}{2}(r_i + r_i') \qquad (2.34)$$

and

$$\Delta r_i = \frac{1}{2}(r_i - r_i') \,. \qquad (2.35)$$

A similar resistance table with both current and voltage leads reversed enables us to construct an Ohmic resistance table $\bar{R}_{ij}^{lm} = (R_{ij}^{lm} + R_{ji}^{ml})/2$ which is shown in Table 2.7, and the non-Ohmic resistance table $\Delta R_{ij}^{lm} = (R_{ij}^{lm} - R_{ji}^{ml})/2$, shown in Table 2.8. Note that the Ohmic resistance table displays all the symmetries of the analysis in Section 2.5.2, and in particular, only the six diagonal (2-terminal) elements are needed to generate the entire table. For the non-Ohmic resistance table, the six diagonal elements only

Table 2.7 The Ohmic resistance table obtained from Table 2.5. (symmetric)

$\overline{R}$	V_{12}	V_{13}	V_{14}	V_{23}	V_{24}	V_{34}
I_{12}	$\rho\Gamma_{12}^{12}+\bar{r}_1+\bar{r}_2$	$\rho\Gamma_{12}^{13}+\bar{r}_1$	$\rho\Gamma_{12}^{14}+\bar{r}_1$	$\rho\Gamma_{12}^{23}-\bar{r}_2$	$\rho\Gamma_{12}^{24}-\bar{r}_2$	$\rho\Gamma_{12}^{34}$
I_{13}	$\rho\Gamma_{13}^{12}+\bar{r}_1$	$\rho\Gamma_{13}^{13}+\bar{r}_1+\bar{r}_3$	$\rho\Gamma_{13}^{14}+\bar{r}_1$	$\rho\Gamma_{13}^{23}+\bar{r}_3$	$\rho\Gamma_{13}^{24}$	$\rho\Gamma_{13}^{34}-\bar{r}_3$
I_{14}	$\rho\Gamma_{14}^{12}+\bar{r}_1$	$\rho\Gamma_{14}^{13}+\bar{r}_1$	$\rho\Gamma_{14}^{14}+\bar{r}_1+\bar{r}_4$	$\rho\Gamma_{14}^{23}$	$\rho\Gamma_{14}^{24}+\bar{r}_4$	$\rho\Gamma_{14}^{34}+\bar{r}_4$
I_{23}	$\rho\Gamma_{23}^{12}-\bar{r}_2$	$\rho\Gamma_{23}^{13}+\bar{r}_3$	$\rho\Gamma_{23}^{14}$	$\rho\Gamma_{23}^{23}+\bar{r}_2+\bar{r}_3$	$\rho\Gamma_{23}^{24}+\bar{r}_2$	$\rho\Gamma_{23}^{34}-\bar{r}_3$
I_{24}	$\rho\Gamma_{24}^{12}-\bar{r}_2$	$\rho\Gamma_{24}^{13}$	$\rho\Gamma_{24}^{14}+\bar{r}_4$	$\rho\Gamma_{24}^{23}+\bar{r}_2$	$\rho\Gamma_{24}^{24}+\bar{r}_2+\bar{r}_4$	$\rho\Gamma_{24}^{34}+\bar{r}_4$
I_{34}	$\rho\Gamma_{34}^{12}$	$\rho\Gamma_{34}^{13}-\bar{r}_3$	$\rho\Gamma_{34}^{14}+\bar{r}_4$	$\rho\Gamma_{34}^{23}-\bar{r}_3$	$\rho\Gamma_{34}^{24}+\bar{r}_4$	$\rho\Gamma_{34}^{34}+\bar{r}_3+\bar{r}_4$

Table 2.8 The non-Ohmic resistance table obtained from Table 2.5. (non-symmetric)

ΔR	V_{12}	V_{13}	V_{14}	V_{23}	V_{24}	V_{34}
I_{12}	$\Delta r_1 - \Delta r_2$	Δr_1	Δr_1	Δr_2	Δr_2	0
I_{13}	Δr_1	$\Delta r_1 - \Delta r_3$	Δr_1	$- \Delta r_3$	0	Δr_3
I_{14}	Δr_1	Δr_1	$\Delta r_1 - \Delta r_4$	0	$- \Delta r_4$	$- \Delta r_4$
I_{23}	$- \Delta r_2$	$- \Delta r_3$	0	$\Delta r_2 - \Delta r_3$	Δr_2	Δr_3
I_{24}	$- \Delta r_2$	0	$- \Delta r_4$	Δr_2	$\Delta r_2 - \Delta r_4$	$- \Delta r_4$
I_{34}	0	$- \Delta r_3$	$- \Delta r_4$	$-\Delta r_3$	$- \Delta r_4$	$\Delta r_3 - \Delta r_4$

determine the off diagonal elements up to an arbitrary constant. To determine all the Δr_i it is necessary to have at least one of the 3-terminal elements. For this model, the non-Ohmic resistance table is independent of the resistivity, because we have assumed that the material itself is Ohmic.

Because the geometric factors are known from the FEM, we can in principle obtain the resistivity and the contact resistances by doing a least squares fit for the expressions in theoretical resistances (Table 2.7 and Table 2.8) and the measured resistances; i.e. we minimize a χ^2 defined by

$$\chi^2 = \sum_i \left[\frac{R_i^e - R_i^t(\rho, r)}{\sigma_i} \right]^2 , \tag{2.36}$$

where R_i^e are the experimental measurements and $R_i^t(\rho, r)$ are the theoretical resistances defined by Eq. (2.33) as a function of the resistivity ρ and contact resistances r. The sum is over the elements of the resistance matrix used for fitting and σ_i is a standard deviation of each experimental measurement, which includes both errors in the resistance measurements. The errors in the geometric factors might be from the incorrect computer modeling of the geometry as well as the small numerical error in the FEM. In practice, the least squares fit is best done separately for the Ohmic and the non-Ohmic parts (Table 2.7 and Table 2.8). The practical details of this fitting will be discussed in the next section, when it is applied to our two samples.

2.4 Experiment

2.4.1 sample preparation

In this section, several experimental processes of sample preparation, contact formation, and the *I-V* measurement by multi probes will be briefly described. Details of this work can be found in Jaeger et al.[27] The experimental measurements have been done on homoepitaxial diamond films and microcrystallites. The films were grown on the diamond substrates where as the microcrystals were grown on Si substrate. Since the conductivity of diamond crystallites has not been measured before in highly irregular geometry, our technique should be compared with a well-known method. We chose the van der Pauw method on the conductivity measurement of a 2d film. The conductivity of a 2d film can be given by the van der Pauw formula in Eq. (2.1), thus our result can be compared with the result from this formula.

The size of a homoepitaxial film (Figure 2.24) is 3 x 3 mm^2 and its thickness is 1.86 μm. It is a good two-dimensional object. The *I-V* measurement was done twice on the same film with different contact formations. Once it was done with a film with four contacts as in Figure 2.24(b). Later two more contacts were attached on the same sample as in Figure 2.24(c) and the measurement was done again. However, only four contacts (gray pads in the figures) were used for the measurement in both cases. Figure 2.25 presents two SEM photos of the CVD diamond crystallites whose conductivities were measured by our method. Although both samples had five contacts, only four contacts were used for the resistance measurement. Two crystallites were grown in the same condition. However, a twin boundary between the contacts was observed in one of the

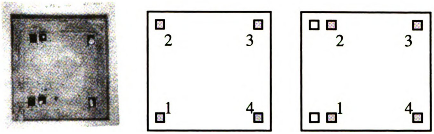

(a) (b) (c)

Figure 2.24 A normal picture of the 2d sample (diamond homoepitaxial film) is shown in (a). Two schematics ((b), (c)) of the sample denote the positions of the contacts. Film 1 (b) has four contacts and film 2 (c) has six contacts. Gray-colored squares in the figures represent the contacts actually used for the measurement.

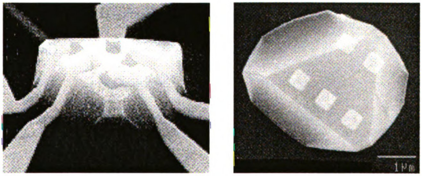

(a) (b)

Figure 2.25 Two micron-sized CVD diamond crystallites, Sample 1 (a) and Sample 2 (b). Sample 1 has Au leads attached on the Ti contacts and Sample 2 is a shape before the lead attachment.

Table 2.9 The characteristics of CVD diamond samples.

Sample	Description
Diamond film (homoepitaxial)	Homoepitaxial film on single crystal (100). Natural diamond substrate. Dimension : 3.0mm x 3.0mm x 1.86μm Contact size : 0.3mm x 0.3mm
Sample 1 (microcrystal)	Isolated microcrystal with no visible defects. Ohmic contacts. SiO_2 substrate. Diameter : ~ 4 μm , Height : ~ 2 μm
Sample 2 (microcrystal)	Isolated microcrystal with a twin defect. Non-Ohmic contacts. SiO_2 substrate. Diameter : ~ 4 μm , Height : ~ 2 μm

sample (b). Although no significant difference of the contacts was observed in the photos, it turned out that the contacts of one sample (a) were Ohmic where as the other contacts in (b) were non-Ohmic. Our method could be tested more generally for these two different samples whether it determines the conductivity, which is independent of the contact properties. The characteristics of all the samples in this work are listed in Table 2.9. All diamond samples were prepared by microwave plasma enhanced CVD at Kobe Steel USA, Inc.

2.4.2 four-probe measurement

With four probes formed on the samples, the *I-V* characteristics were measured by DC voltage as a function of temperature in a vacuum level less than 10^{-6} torr. To investigate the *I-V* characteristics of the contacts, a fixed amount of current was used for each current flow. All possible combinations of the voltage and current measurement generated a 6 by 6 resistance table that was described in Section 2.2.2. A total of 36 elements in the resistance table consist of six 2-terminal terms, six 4-terminal terms, and twenty-four 3-terminal terms. While these measurements were done through a broad temperature regime (-100 ~ 170° C) as in Figure 2.26, a complete measurement of a resistance table was done only for a specific temperature for each sample. At the other temperatures, only one 4-terminal resistance ($R_{23}^{14} = V_{14} / I_{23}$) was measured. Since the geometrical factor is temperature independent, the conductivity at the other temperatures can be obtained by dividing the 4-point resistances with this geometrical factor. The investigation of the temperature dependence of the conductivity provides the activation

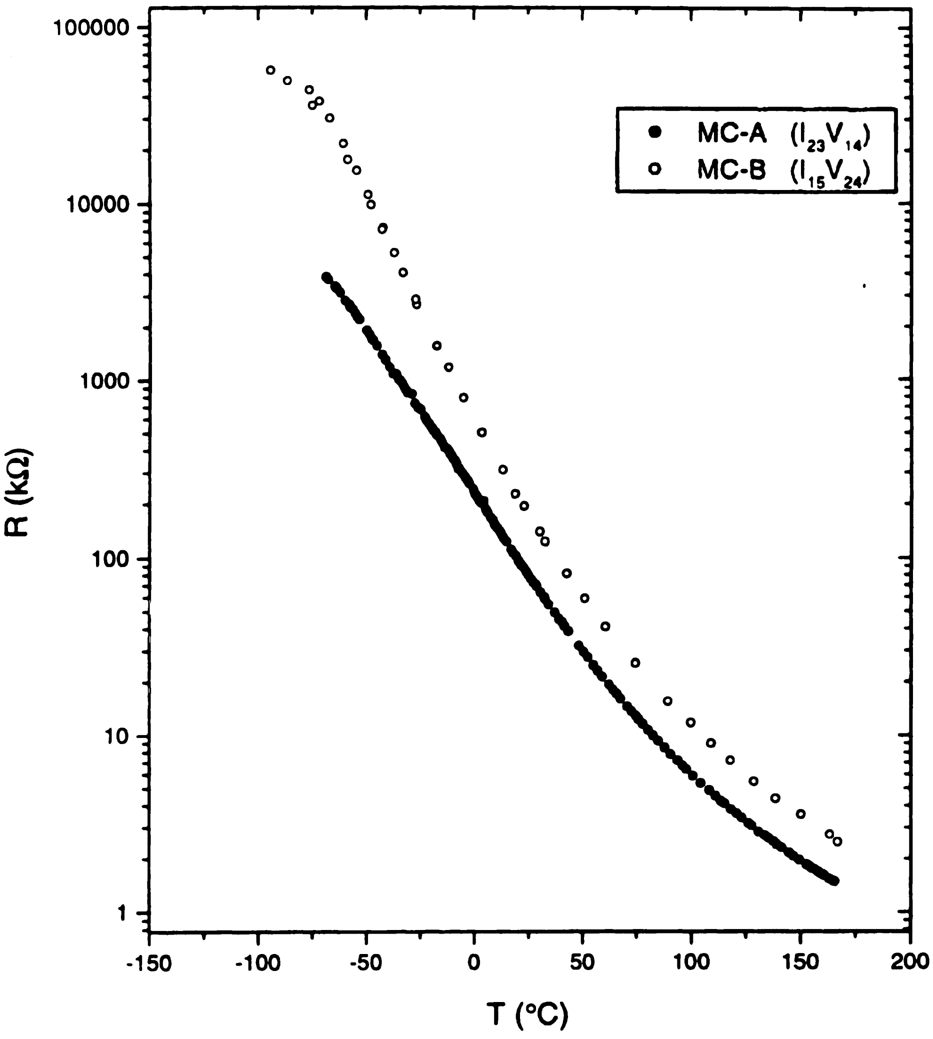

Figure 2.26 Temperature dependence of a resistance of diamond crystallites (Sample 1 (solid circles) and Sample 2 (open circles)). To investigate the temperature dependence of the resistivity of these samples, a four-terminal resistance (R_{23}^{14}) were measured over a wide range of temperatures.

energies of the doped semiconductors.[28] The conduction mechanism of each sample can be understood and compared using these activation energies.

The resistance measurements for some samples were done with two different current directions to determine the non-Ohmic contact resistances. Usually two diagonal resistances were measured for these two current directions; they could provide complete information of non-Ohmic contact resistances. In this submicron scale, the leads were electrically fragile because static discharges could happen near the contacts. The melting of metal leads that might cause the missing of an entire portion of the contacts sometimes happened during the measurement. So the current level should be kept below 10 μA to prevent the contact disconnection from the melting. With this problem, some measurements did not provide enough information (two complete sets of resistance table for two current flows) needed for the analysis.

2.5 Analysis

2.5.1 diamond film

To test our method, we used two films with multi probes whose conductivity could be determined by the van der Pauw method. One (Film 1) had only four leads on the film and the other (Film 2) had six leads. With the Film 1 with four contact pads of Figure 2.24(b), we measured all possible combinations of current and voltage measurement to construct a 6 by 6 resistance table of Table 2.10. It was given by constant current (1 μA) to investigate Ohmic behaviors of contacts at T=24.7° C. For this sample, we measured two diagonal terms (two terminal measurements) for two different current

Table 2.10 Resistances measured for homoepitaxial film by 4-probe experiment (kΩ).

R	V_{12}	V_{13}	V_{14}	V_{23}	V_{24}	V_{34}
I_{12}	**264.6(329.5)**	106.65	90.95	-158.17	-173.94	-15.72
I_{13}	107.41	**198.7(198.7)**	105.988	91.239	-1.405	-92.658
I_{14}	91.62	106.097	**184.5(184.5)**	14.485	92.636	78.158
I_{23}	-232.6	90.23	14.370	**322.4(248.1)**	247.3	-75.834
I_{24}	-246.7	-1.219	91.391	246.5	**337.7(265.1)**	92.612
I_{34}	-15.89	-93.714	78.268	-77.86	94.170	**172.1(172.1)**

Table 2.11 Geometrical factor table obtained by FEM (mm^{-1}).

Γ	V_{12}	V_{13}	V_{14}	V_{23}	V_{24}	V_{34}
I_{12}	**904.04**	515.40	393.80	-388.65	-510.24	-121.59
I_{13}	515.32	**1023.48**	506.32	508.16	-9.007	-517.16
I_{14}	393.80	506.27	**947.54**	112.47	553.74	441.27
I_{23}	-388.68	508.13	112.46	**896.80**	501.13	-395.67
I_{24}	-510.18	-9.044	553.81	501.14	**1063.99**	562.85
I_{34}	-121.54	-517.22	441.30	-395.68	562.84	**958.52**

Table 2.12 The resistivity and contact resistances of diamond film (Film 1) given by van der Pauw formula (VDP) and our method.

ρ (Ω cm) (VDP)	ρ (Ω cm)	$\bar{r}_1$, Δr_1 (kΩ)	$\bar{r}_2$, Δr_2 (kΩ)	$\bar{r}_3$, Δr_3 (kΩ)	$\bar{r}_4$, Δr_4 (kΩ)
12.51	12.91	37.8, -0.9	139.8, 34.1	24.55, -1.45	19.95, -1.35

directions to identify all non-Ohmic contact resistances. Notice that some of the matrix terms showed substantial asymmetry indicating that some contacts were non-Ohmic. However, the 4-terminal measurements (underlined) showed a relatively good symmetry. We also did the FEM analysis using ABAQUS to find out the geometrical factor table in Table 2.11. From the 36 elements in this table, we used only the 4-terminal terms to determine the resistivity of this film that would be compared with the same quantity calculated from the van der Pauw method. The contact resistances were obtained by fitting the diagonal elements in both tables. They turned out substantially non-Ohmic as anticipated from the asymmetry of the resistance table. The results from the van der Pauw and our method are presented in Table 2.12. The resistivity given by van der Pauw method was 12.51 (Ω cm) and the resistivity from our method was 12.91 (Ω cm) which agrees within 3% error. Thus, the fitted resistivity from our method agrees well with the resistivity from the van der Pauw formula.

Another test has been done on Film 2 that had six contact pads. At this time, I obtained two complete resistance tables for the different current directions as shown in Table 2.13 and Table 2.14. The minus signs in Table 2.14 came from the definition of the resistance. Table 2.13 and Table 2.14 were given by constant currents (100 nA) at T=22.8° C. These tables show a good symmetry in each term that indicates that the contacts are Ohmic. The geometrical factors of the film were given by the numerical simulation and shown in Table 2.15. All six pads were constructed on the film as perfect conductors, although two pads were not used in the measurement. From these geometrical factors and the resistance tables, the conductivity of the film could be determined by the van der Pauw method and our method. By the van der Pauw formula,

Table 2.13 Resistances measured by 4-probe experiment (kΩ).

R	V_{12}	V_{13}	V_{14}	V_{23}	V_{24}	V_{34}
I_{12}	**149.20**	76.30	53.51	-70.91	-91.58	-20.90
I_{13}	76.14	**162.20**	66.30	83.66	-9.91	-93.36
I_{14}	55.23	66.07	**141.10**	10.98	83.69	72.65
I_{23}	-70.40	83.03	10.97	**156.80**	81.17	-72.20
I_{24}	-90.63	-9.90	83.11	80.85	**177.80**	93.12
I_{34}	-20.87	-92.50	72.08	-72.00	92.53	**168.60**

Table 2.14 Another resistance table for the opposite current flows of Table 13. (kΩ)

R	V_{12}	V_{13}	V_{14}	V_{23}	V_{24}	V_{34}
I_{21}	**-149.00**	-76.06	-53.50	71.03	91.73	20.90
I_{31}	-75.89	**-162.00**	-66.06	-83.66	9.93	93.45
I_{41}	-55.04	-65.86	**-141.00**	-10.97	-83.76	-72.77
I_{32}	70.30	-83.09	-10.97	**-156.70**	-81.07	72.24
I_{42}	90.46	9.92	-83.23	-80.78	**-177.80**	-93.22
I_{43}	20.85	92.42	-72.28	71.96	-92.64	**-168.70**

Table 2.15 Geometrical factors calculated from FEM (mm^{-1}).

Γ	V_{12}	V_{13}	V_{14}	V_{23}	V_{24}	V_{34}
I_{12}	**712.19**	408.59	262.44	-303.61	-449.75	-146.14
I_{13}	408.63	**878.20**	350.58	469.57	-58.05	-527.62
I_{14}	262.47	350.58	**779.07**	88.11	516.60	428.49
I_{23}	-303.57	469.67	88.07	**773.24**	391.65	-381.59
I_{24}	-449.70	-58.07	516.57	391.63	**966.27**	574.64
I_{34}	-146.19	-527.69	428.44	-381.50	574.64	**956.13**

Table 2.16 The resistivity and contact resistances of Film 2 given by van der Pauw formula (VDP) and our method.

ρ (Ω cm) (VDP)	ρ (Ω cm)	$\bar{r}_1$, Δr_1 (kΩ)	$\bar{r}_2$, Δr_2 (kΩ)	$\bar{r}_3$, Δr_3 (kΩ)	$\bar{r}_4$, Δr_4 (kΩ)
12.62	13.25	17.5, 0.05	27.35, 0.05	18.15, 0.05	11.65, 0.05

the resistivity ρ was given by 12.62 (Ω cm). We used only two 4-terminal resistances (R_{12}^{34} , R_{14}^{23}) in the formula because the other term R_{13}^{24} was very unstable due to the symmetric formation of the contact pads. And the same resistivity as well as the contact resistances were obtained by our method and compared with the result from the van der Pauw method in Table 2.16. The same 4-terminal geometrical factors (R_{12}^{34} , R_{14}^{23}) used in the van der Pauw method were used to extract another resistivity 13.25 (Ω cm) by our method. It agreed with the van der Pauw result (12.62 (Ω cm)) within 5% error. All of the four contact resistances in the same table show good Ohmic behaviors as expected from measured tables. Our technique works well with a two dimensional sample. It was verified by the comparison of the result from the van der Pauw method. Therefore, we suggest that it can be applied to the 3d sample, too. One of the advantages of our method is that it could determine the contact resistances besides the resistivity of a sample. The detailed fitting procedure to select data set and fitting parameters will be mentioned in next section for the analysis of crystallites.

Another test simulation was done to check how the result was changed depending on the positions of leads. When one of the leads was moved by -0.1mm in x-direction

Table 2.17 Stability test of 4-terminal resistances on the position of one contact.

	R_{12}^{34}	R_{13}^{24}	R_{14}^{23}	R_{23}^{14}	R_{24}^{13}	R_{34}^{12}
Before (kΩ)	-121.59	-9.007	112.47	112.46	-9.044	-121.54
After (kΩ)	-124.84	-13.06	111.79	111.79	-13.06	-124.84
Error (%)	2.7	44.4	0.6	0.6	44.4	2.7

(sample size is about 3x3 mm^2), six terms of 4-terminal method were shifted from the initial values as in Table 2.17. Two of these terms (R_{13}^{24}, R_{24}^{13}) given by the crossed formations of voltage and current measurements showed the significant changes up to 44.4% by the shifting of one lead. However, the other terms turned out stable. From this result, it has been realized that the position of the contacts should be reconstructed accurately for the FEM especially for the symmetric formation.

2.5.2 sample 1 (*Ohmic* contacts)

As an illustration of this technique on 3d samples, we used two diamond crystallites with four terminals (Figure 2.25). A resistance matrix for Sample 1 (Table 2.18) was completed by making all 36 resistance measurements. Diagonal terms in boldface denote 2-terminal measurements and the underlined values are 4-terminal measurements. A 6 x 6 matrix of geometrical factors is obtained by using the FEM and shown in Table 2.19. Diagonal terms in boldface denote 2-terminal measurements and the underlined values are 4-terminal measurements. Within the experimental error, Table 2.18 is symmetric which indicates that r_2 and r_3 are Ohmic. If the contact resistances are Ohmic, we can determine the resistivity ρ and the four contact resistances ($r_i = r_i' = \bar{r}_i$, $i = 1,..,4$).

As a check of the validity of our method, we first calculated the resistivity from the 4- terminal measurements (where $R_{ij}^{lm} = \rho\Gamma_{ij}^{lm}$) with a linear fit through all six data points and the origin. We then used this ρ to determine the contact resistances from the 3-terminal measurements (each of which involves only one contact resistance) and then

Table 2.18 Resistances obtained from the experimental measurement for Sample 1 (kΩ).

R	V_{12}	V_{13}	V_{14}	V_{23}	V_{24}	V_{34}
I_{12}	**720.0**	560.0	508.0	-176.0	-231.8	-55.5
I_{13}	568.7	**1039.0**	534.5	497.3	-34.7	-531.1
I_{14}	518.4	540.2	**986.0**	20.2	500.0	476.9
I_{23}	-174.5	498.7	20.7	**665.0**	195.1	-477.7
I_{24}	-230.6	-35.2	498.5	195.4	**718.0**	531.0
I_{34}	-55.7	-534.2	473.7	-477.6	529.2	**999.0**

Table 2.19 Geometrical factors from the finite element method for Sample 1(μm^{-1}).

Γ	V_{12}	V_{13}	V_{14}	V_{23}	V_{24}	V_{34}
I_{12}	**1.6609**	0.9635	0.7955	-0.6974	-0.8653	-0.1679
I_{13}	0.9634	**1.9550**	0.9568	0.9916	-0.006647	-0.9982
I_{14}	0.7957	0.9569	**1.5608**	0.1612	0.7651	0.6039
I_{23}	-0.6973	0.9916	0.1613	**1.6889**	0.8586	-0.8303
I_{24}	-0.8652	-0.006684	0.7651	0.8585	**1.6303**	0.7718
I_{34}	-0.1679	-0.9982	0.6038	-0.8303	0.7717	**1.6021**

Table 2.20 Resistivity and contact resistances for Sample 1, assuming that all the contact resistances were Ohmic.

	ρ (Ω cm)	r_1 (kΩ)	r_2 (kΩ)	r_3 (kΩ)	r_4 (kΩ)
(a)	23.72	316.3	6.1	276.2	329.0
(b)	22.50	314.0	15.0	285.0	336.0
(c)	23.72	303.3	5.6	274.0	329.0
(d)	23.58	317.6	7.3	277.5	330.0

averaged the results. The results are shown in row (a) of Table 2.20. I then did a least squares fit for five parameters to the six 2-terminal measurements. The results are shown in row (b). In (c), the resistivity was fitted by 4-terminal measurement as in (a), and four contact resistances were obtained from six diagonal terms by a least squares fit. Finally, we fitted five parameters with all 36 elements of the resistance matrix, the results of which are shown in row (d) of Table 2.20. It is clear that all four methods give essentially the same results. Note that one of the contacts has a very small resistance compared to the others.

2.5.3 sample 2 (*non-Ohmic* contacts)

The measured resistance matrix for Sample 2 is given in Table 2.21. All measurements were done at constant current (100 nA) at room temperature (T= 20° C). The values in parentheses in the diagonal terms were measured for a reversed current flow. The different magnitudes in these two measurements show the non-Ohmic behavior of the contacts. Diagonal terms in boldface denote 2-terminal measurements and the underlined values are 4-terminal measurements. Using Table 2.5, it is clear from the asymmetries that contact resistance 3 was very non-Ohmic, and that contact resistance 2 had a small non-Ohmic part. As discussed in the previous section, a second set of measurements had to be taken, with the current probes reversed. This was only done for the six diagonal (2-terminal) elements before the leads were damaged. Nevertheless, this is a sufficient set of data to determine the resistivity and all the contact resistances. The geometrical factors are given for the Sample 2 as in Table 2.22. We processed the data for Sample 2 in four distinct ways to test the accuracy of the fitting procedure.

In the first method we first calculated the resistivity from the 4-terminal measurements and with this ρ determined six of the eight contact resistances from the 3-terminal measurements, and the remaining two contact resistances (r_1' and r_4) from the diagonal elements with the currents reversed. The results of this analysis are shown in row (a) of Table 2.23. In the second method we did a least squares fit to obtain the resistivity and the Ohmic part of the contact resistances ($\overline{r}_i$, $i = 1,..,4$), from the six diagonal elements of $\overline{R}_{ij}^{lm}$. From the six diagonal elements of ΔR_{ij}^{lm}, and the 3-terminal elements of the original resistance matrix that involve both r_2 and r_2', i.e. the elements (R_{12}^{23}, R_{12}^{24}, R_{23}^{12}, R_{24}^{12}), we were able to fit the non-Ohmic part of the four contact resistances (Δr_i, $i = 1,..,4$). The results are shown in row (b) of Table 2.23. There is rather good agreement between the two methods, with only a 10% difference in the resistivity. This agreement obtains in spite of the very large and non-Ohmic contact resistance r_3 that dominates the least squares fitting procedure for the diagonal elements. In general, it is probably best to determine the resistivity from the four terminal measurements, and so as a final check, we used the value of ρ determined from the 4-terminal measurements. And a least squares fit was done to obtain the Ohmic part of the contact resistances ($\overline{r}_i$, $i = 1,..,4$), from the six diagonal elements of $\overline{R}_{ij}^{lm}$. The non-Ohmic parts of the contact resistance are unchanged by this alternative method of determining the resistivity. These results are shown in row (c) of Table 2.23. Finally, the row (d) of Table 2.23 was given by fitting all parameters by whole table.

Table 2.21 Resistances obtained from the experimental measurement for Sample 2 (kΩ).

R	V_{12}	V_{13}	V_{14}	V_{23}	V_{24}	V_{34}
I_{12}	**875(875)**	386	369	-432.3	-451	-18.1
I_{13}	392	**3771(4878)**	587	3240	203	-3032
I_{14}	369.5	389	**1591(1591)**	212	1114	917
I_{23}	-450	3255	221	**3774(4936)**	663	-3026
I_{24}	-471	192	1126	654	**1705(1705)**	943
I_{34}	-20.1	-4207	918.9	-4190	935	**5236(4098)**

Table 2.22 Geometrical factors from the finite element method for Sample 2 (μm^{-1}).

Γ	V_{12}	V_{13}	V_{14}	V_{23}	V_{24}	V_{34}
I_{12}	**1.0825**	0.6336	0.6049	-0.4489	-0.4777	-0.02869
I_{13}	0.6336	**1.4178**	0.9440	0.7843	0.3104	-0.4737
I_{14}	0.6049	0.9440	**1.4112**	0.3391	0.8064	0.4671
I_{23}	-0.4489	0.7842	0.3391	**1.2332**	0.7880	-0.4450
I_{24}	-0.4776	0.3104	0.8064	0.7880	**1.2840**	0.4958
I_{34}	-0.02869	-0.4738	0.4673	-0.4452	0.4960	**0.9407**

Table 2.23 Resistivity and contact resistances for Sample 2.

	ρ (Ω cm)	$\bar{r}_1$, Δr_1 (kΩ)	$\bar{r}_2$, Δr_2 (kΩ)	$\bar{r}_3$, Δr_3 (kΩ)	$\bar{r}_4$, Δr_4 (kΩ)
(a)	62.68	-3.0 , -7.00	162.6 , 10.7	3379.6 , 600.7	675.5 , 51.3
(b)	69.08	-26.8 , 11.6	152.9 , 4.72	3361.7 , 575.9	654.4 , 7.70
(c)	62.68	19.8 , 11.6	189.5 , 4.72	3398.1 , 575.9	692.2 , 7.70
(d)	60.78	9.30 , -7.50	173.1 , 12.5	3390.5 , 600.9	687.0 , 52.0

In this analysis, it should be noted that there are some possibilities of error in modeling and fitting as well as experimental measurements. First, we suspect the effective contact area in the sample is less than that apparent in the SEM photographs. Some part of the contact might not form a good electrical contact with the sample, and hence decreases the real contact area. The sensitivity of diagonal and 4-terminal terms has been tested by calculating the resistance changes by shrinking the area of all the contacts by 1/3. The 2-terminal measurements varies 30~40 % but the 4-terminal ones were changed by less than 10%. The resistivity fitted by 4-terminal elements turned out more stable than the contact resistances included in 2-terminal terms under this change of the contact geometry. Hence the resistivity should be fitted from the 4-terminal resistance measurements, which are contact independent resistances, and the contacts are then obtained subsequently by fitting the whole resistance table. We note that a fine meshing is necessary for reliable results for the geometrical factors for the 2-terminal measurements, but a coarser meshing is sufficient to get reliable geometric factors for the 4-terminal measurements. And we could get better results by doing the measurements on many different samples that have the same resistivity and with many contacts that give more terms for consistency checks.

Throughout our theoretical treatment, although we have taken into account the spatial distribution of currents within the sample, there has been no attempt to consider the charge redistribution at surfaces and interfaces, for example due to band bending. Contact resistances, in particular, will depend on local electric fields which, in turn, will; depend on details of the semiconductor-metal interface. In retrospect, it is somewhat surprising that a model invoking local contact resistances should work so well, with contact pad dimensions and separations approaching a space charge depth. If the scale of the experiments were to shrink further, these considerations will need to be treated with more rigor. Even if the reconstructed geometry is correct, one more error is possible. The conductivity of the sample was assumed to be isotropic due to the diamond lattice structure. So, the conductivity has been treated as a scalar, not a tensor. However, this assumption may not be true for a sample with a twin boundary that could be observed in Sample 2. This twin boundary may affect the isotropy of conductivity or homogeneity of the material property. Nevertheless the reciprocal theorem is still true for anisotropic conductivity; a resistance table is still symmetric for anisotropic tensor. We did not analyze this effect on Sample 2 when the conductivity was determined in this chapter since the defect is not apparent to be considered in the SEM photo.

The temperature dependence of conductivity has been one of main concerns because it is crucial to understand the conduction mechanism of the doped semiconductors. The temperature dependence of the resistivity in Figure 2.27 was obtained from the temperature dependence of a 4-terminal resistance in Figure 2.26. It was done by rescaling the resistances with a geometrical factor for the measurement. The

Table 2.24 Fit result of conductivity model with two activation energies for data in Figure 2.27.[29]

Sample	σ_1 ($10^2\ \Omega^{-1}\ \mathrm{cm}^{-1}$)	E_1 (eV)	σ_2 ($10^2\ \Omega^{-1}\ \mathrm{cm}^{-1}$)	E_2 (eV)
Sample 1	114± 4	0.347 ±0.001	1711.9 ±345	0.109 ±0.004
Sample 2	163± 5	0.351 ±0.001	21.8± 17	0.059 ±0.014
Polycrystalline film	0.95 ±0.12	0.199± 0.004	102± 6	0.0089 ±0.009

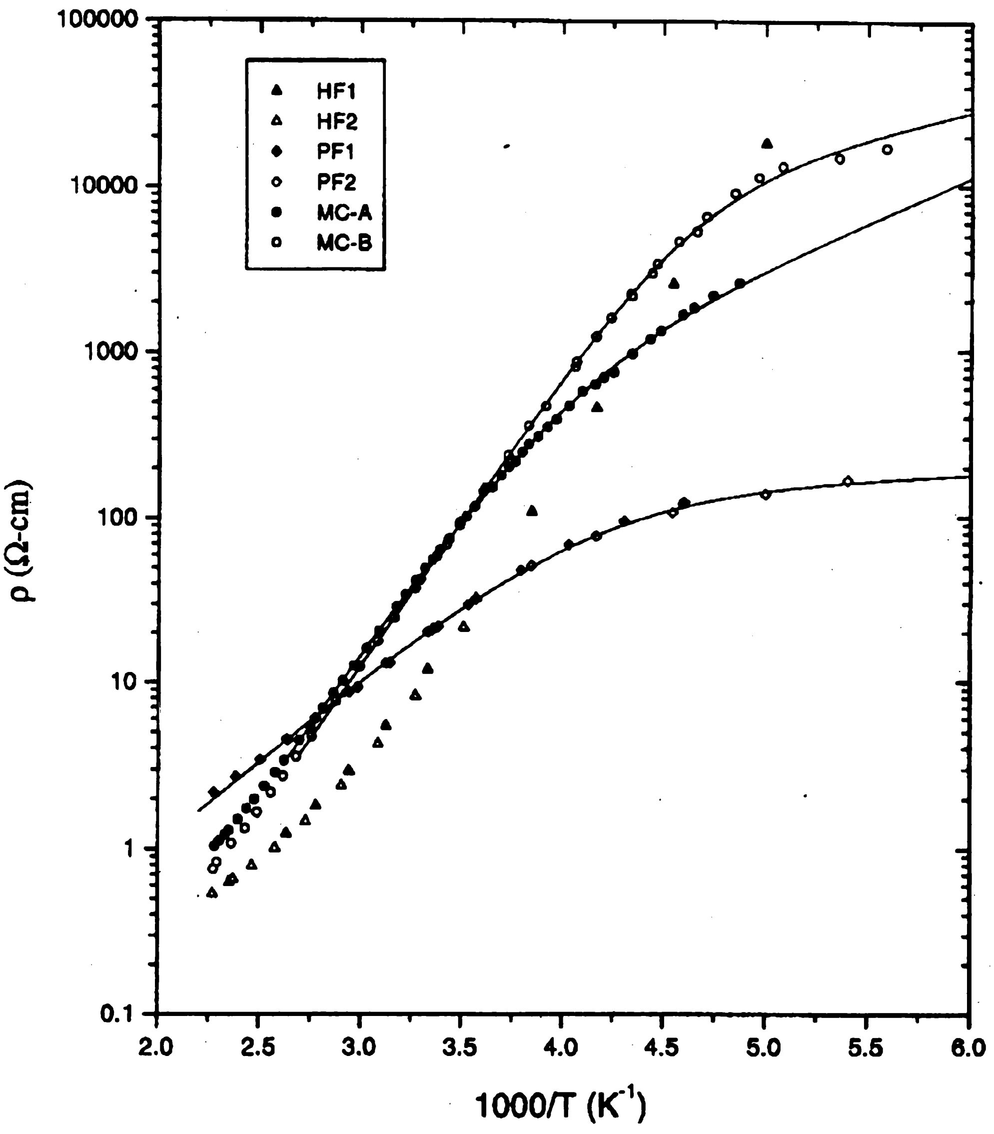

Figure 2.27 Temperature dependence of the resistivities of the diamond samples. Two microcrystallites (MC-A, MC-B) correspond to Sample 1 and Sample 2. PF1 and PF2 are polycrystalline films. HF1 and HF2 are homoepitaxial films. The resistivity of these samples was obtained by rescaling the resistance measurement in Figure 2.26 using the fitted resistivity.

geometrical factor for the 4-terminal measurement is a constant throughout whole temperature regime. The temperature dependence of the conductivity is governed by

$$\sigma = \sigma_1 \exp(-E_1 / kT) + \sigma_2 \exp(-E_2 / kT), \tag{2.37}$$

where E_1 is the impurity ionization energy and E_2 is from the nearest neighbor hopping. σ_1, σ_2, E_1 and E_2 were obtained by fitting the data with this relation. I present the fitted results given by Jaeger in Table 2.24.[29] It was observed that the activation energy E_1 was the same for two diamond crystallites, but the polycrystalline film presented significantly different activation energy. That indicates that the conduction mechanism in the polycrystalline film is quite different from the homoepitaxial film or microcrystallites. The discrepancy might be from the effect of grain boundaries in the film as mentioned in the motivation of this work. No significant structural defects such as grain boundaries are formed in a homoepitaxial film since it is grown on the diamond substrate.

2.6 Conclusion

A method to measure the resistivity and contact resistances of single crystals in complex geometry has been introduced and demonstrated on micron-sized diamond crystallites. The method is quite general, if the material of the sample is homogeneous and Ohmic, with contacts that can be non-Ohmic but should be equipotential surfaces. The sample resistivity and contact resistances were obtained experimentally using 4-probe measurements, aided by finite element calculations. This technique can be applied to determine the sample resistivity using any shape of sample. It is possible to determine the sample resistivity and the Ohmic part of the contact resistances solely from the set of 2-terminal measurements, with currents in both directions, but it is probably best to use the 4-terminal measurements to determine the resistivity. The most accurate results will be obtained from a complete set of resistance measurements with currents in both directions.

This technique was tested to determine the conductivity of some materials in complicated geometry like CVD diamond crystallites, but it should be noted that there are some restrictions on the application of this method. For a material that has an anisotropic conductivity, our method cannot be applied. There are six terms in a general conductivity tensor because of its symmetry. In our method described in this chapter, the conductivity has been treated as a scalar, not a tensor. Therefore, we need a different approach for the anisotropic case. The next chapter will be devoted to a presentation of a method to determine the anisotropic tensor using the *iterative linearization* technique as well as the multi probe measurement.

Chapter 3 ANISOTROPIC CONDUCTIVITY MEASUREMENT FOR COMPLEX GEOMETRY

3.1 Introduction

In this chapter, I introduce a method to determine the *anisotropic conductivity* of an arbitrary shaped sample. The conductivity of our samples (CVD diamond crystallites) was assumed isotropic throughout the previous chapter due to the symmetric lattice structure of the samples.[30,31] However, one of the crystallites had a clear twin boundary between the contact pads (see Figure 3.1). The homogeneity may not be satisfied in this sample because of this defect, that is a main requirement for the application of our method. Under the assumption that the effect of the defect could be neglected, its contribution to the transport has not been considered rigorously before.

However, this inhomogeneity of the sample induced by some significant defects

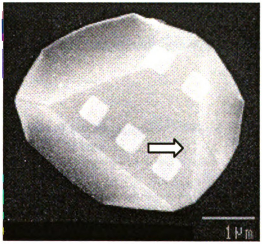

Figure 3.1 A diamond crystallite has a local defect (twin boundary) denoted by an arrow. This defect was neglected in the isotropic conductivity determination.

should be considered more carefully in the determination of the material properties. Moreover, some materials (Bi, Sn) and some superconductors are known to have anisotropic conductivity tensors from the anisotropic lattice structures (see Table 3.1). Diamond and Aluminum have an isotropic conductivity tensor from the cubic lattice structures, but some materials in other lattice structures (tetragonal, trigonal, and hexagonal) usually have anisotropic conductivity tensors. Therefore, the conductivity should be determined as a tensor form that has six terms in 3d. Only three diagonal terms can be determined when the three principal axes are known.

The main difference between the isotropic and anisotropic case is related to the geometrical factor. For an anisotropic conductivity tensor, the resistances can not be represented by the simple form of a geometrical factor times conductivity. In fact, the geometrical factor cannot be defined in the anisotropic case. Nevertheless, it may be possible to calculate the anisotropic conductivity tensor for some simple shapes (brick, cylinder) that build up uniform current patterns. However, it is not easy to fabricate the samples into such shapes in micron scale, and the principal axes of conductivity are generally unknown. To identify this conductivity tensor, I developed an algorithm using

Table 3.1 Electrical resistivity of metalic crystals.[32] Values of principal resistivities at T=20° C. (in unit $10^{-6}\ \Omega$ cm)

Crystal	System	ρ_1, ρ_2	ρ_3
Aluminum	Cubic	2.72	2.72
Tin (Sn)	Tetragonal	9.9	14.3
Bismuth (Bi)	Trigonal	109.0	138.0
Zinc	Hexagonal	5.91	6.13

the multi-probe measurement and computer simulations (the FEM analysis and the *iterative linearization technique*). This method has been tested for the 2d and 3d computer models and a real sample (Bi) whose anisotropic tensor components are already known as in Table 3.1.

In the next section, a brief description of the nonlinear problem induced by anisotropic conductivity is presented and I will describe the basic idea of a method based on *iterative linearization* in Section 3.2.2. The orthogonal transformation is introduced to find the principal axes of a tensor in Section 3.2.3. In Section 3.3, I introduce a general scheme of computer simulation using FEM on the computer models (Section 3.3.1) and the interfaces between the FEM package and the minimization routine (Section 3.3.2). I will explain how to apply this method to real material (Bi) in Section 3.4. The sample geometry and the lead formations will be described in that part. The results of the computer models and the real sample are presented and analyzed in Section 3.5.1 ~ 3.5.3. The stability test on our method is discussed in Section 3.5.4. To close this chapter, I will provide the conclusion and suggestions in Section 3.6.

3.2 Theory

3.2.1 anisotropic conductivity tensor

For an isotropic resistivity tensor, a sample resistance ${}^{s}R_{ij}^{lm}$ has been defined by

$$ {}^{s}R_{ij}^{lm} = \rho \Gamma_{ij}^{lm} , \tag{3.1}$$

where Γ_{ij}^{lm} is a geometrical factor that depends only on the geometry and the resistivity ρ is single parameter. The geometrical factor does not have any orientation dependence since the sample is isotropic. This simple relation in Eq. (3.1) makes it possible to determine a resistivity by fitting the geometrical factors Γ_{ij}^{lm} and the sample resistances ${}^{s}R_{ij}^{lm}$. However, the conductivity should be considered as a 3 x 3 tensor in general. This anisotropic behavior of the conductance could be observed in many materials. The conductivity tensor is symmetric when there is no external magnetic field.[33] Then, the number of the independent terms in the tensor is given by $d(d+1)/2$ in d-dimensions. It becomes three in 2d and six in 3d as shown in the following equations.

$$\sigma = \begin{pmatrix} \sigma_{xx} & \sigma_{xy} \\ \sigma_{xy} & \sigma_{yy} \end{pmatrix} \text{ in 2d} \tag{3.2}$$

$$\sigma = \begin{pmatrix} \sigma_{xx} & \sigma_{xy} & \sigma_{xz} \\ \sigma_{xy} & \sigma_{yy} & \sigma_{yz} \\ \sigma_{xz} & \sigma_{yz} & \sigma_{zz} \end{pmatrix} \text{ in 3d} \tag{3.3}$$

If the principal axes of a conductor are known and the coordinate axes in the simulation are set up equal to these principal axes, the conductivity tensor becomes a diagonalized tensor. Since all off-diagonal terms are set zeroes, the only unknown terms in a tensor are the diagonal terms. Even so we cannot use the previous method to determine the conductivity tensor because the geometrical factor Γ_{ij}^{lm} cannot be defined as in Eq. (3.1) for the anisotropic tensor ($\ddot{\sigma}$), i.e.

$${}^{s}R_{ij}^{lm} = R_{ij}^{lm}(\ddot{\sigma}) \neq \rho\Gamma_{ij}^{lm} \ . \tag{3.4}$$

So, the resistivity ρ cannot be obtained by dividing a resistance by a geometrical factor. All elements in a conductivity tensor are correlated in the expression of the resistances. These elements cannot be separated from the geometrical factors as previously done for the isotropic tensor. More general relations between the experimental measurements and the theoretical calculations should be

$$^{e}R_{ij}^{lm} = {}^{s}R_{ij}^{lm}(\overset{\leftrightarrow}{\sigma}) + r_i(\delta_{il} - \delta_{im}) + r_j'(\delta_{jm} - \delta_{jl}), \tag{3.5}$$

where $^{e}R_{ij}^{lm}$ is an experimental measurement and r_i and r_i' represent non-Ohmic contact resistances. We need to extract the conductivity tensor using Eq. (3.5) aided by the multi probe measurement and the FEM analysis.

In the presence of a magnetic field B, the tensor becomes antisymmetric and can be separated into a symmetric and an antisymmetric part as in Eq. (3.6).

$$\begin{aligned} \sigma = \begin{pmatrix} \sigma_{xx} & \sigma_{xy} & 0 \\ \sigma_{yx} & \sigma_{yy} & 0 \\ 0 & 0 & \sigma_{zz} \end{pmatrix} &\Rightarrow \begin{pmatrix} \sigma_{xx} & \sigma_{xy} + R_z B \sigma_0^{\,2} & 0 \\ \sigma_{xy} - R_z B \sigma_0^{\,2} & \sigma_{yy} & 0 \\ 0 & 0 & \sigma_{zz} \end{pmatrix} \\ &= \begin{pmatrix} \sigma_{xx} & \sigma_{xy} & 0 \\ \sigma_{xy} & \sigma_{yy} & 0 \\ 0 & 0 & \sigma_{zz} \end{pmatrix} + B \begin{pmatrix} 0 & R_z \sigma_0^{\,2} & 0 \\ -R_z \sigma_0^{\,2} & 0 & 0 \\ 0 & 0 & 0 \end{pmatrix}, \end{aligned} \tag{3.6}$$

where R_z is the Hall coefficient and σ_0 is given by

$$\sigma_0 = \left(\sigma_{xx}\sigma_{yy} - \sigma_{xy}^{\,2}\right)^{1/2}. \tag{3.7}$$

However, this Hall measurement will not be considered in this work.

3.2.2 iterative linearization technique for nonlinear inverse problem

The unknown conductivity tensor can be determined by fitting two resistances (experimental and theoretical) in Eq. (3.5). Since the functional forms of a resistance in terms of the tensor elements are generally unknown, we should use the *iterative linearization method.* While the tensor elements are changed, the linearized resistances calculated from the FEM are fitted to the experimental measurements to extract the optimized tensor elements. Usually the optimized solution can be achieved after many iterations of the linearization and least square fittings. This technique is also known as the *Gauss-Newton method.*[34] The term *Gauss* is named by the least-square fitting of the resistances and the term *Newton* comes from the iterative linearization technique in the optimization procedure. This technique has been widely used to solve nonlinear optimization problems, for instance the earth conductivity problem in geophysics.[35]

Here I describe the detailed procedures of this technique. Suppose we are trying to find an anisotropic conductivity tensor with unknown principal axes. Simply we choose an arbitrary tensor to start the iteration, which is defined by six parameters. To get the linearized form of each resistance for this tensor, all first derivatives of the resistances with respect to the six tensor elements are calculated using the FEM. Then, the expressions of the resistances are known as linearized forms, we can perform the least square fitting to extract a tensor. However, since the linearized forms are correct only near the previous tensor, the fitted tensor may not be the global solution of the optimization. Therefore, the fitted tensor substitutes for the old tensor and the same procedures are done. This iteration will go on until the best-optimized tensor is obtained. After the tensor is obtained, it is diagonalized by the orthogonal transformation to find the principal axes and values of the tensor.

In this iteration, the first step is very important. The iteration begins from an arbitrary selected point that might be far from the global solution. Then it is very crucial to find a next point close to the global solution in the first step. We begin the first step with an isotropic tensor (unit conductivity) and keep the tensor isotropic throughout the

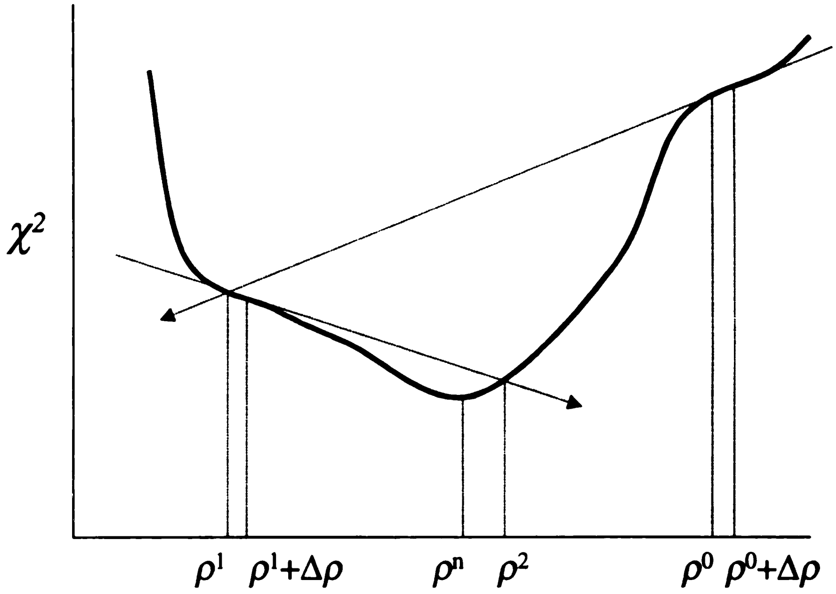

Figure 3.2 Iterative linearization technique of χ^2 minimization in 1d (Newton method). This technique is useful when the function form of the χ^2 is not known. Each step, the function form is approximated to a linearized form by Taylor expansion. After many iterations, it reaches the minimum point.

step. This procedure is exactly the same as our method in the previous chapter. We can determine the scale factor ρ^0 that is nothing but an isotropic conductivity. When a tensor is isotropic, there is only one parameter ρ^0 ($= \rho_{xx} = \rho_{yy} = \rho_{zz}$). Since the conductivity is isotropic in this step, we can use the relation of

$$R = \rho^0 \Gamma_0 \ , \tag{3.8}$$

where Γ_0 is a geometrical factor given by the initial tensor that is a unit conductivity tensor. The fitted tensor that will be used for the next step has same diagonal terms of ρ^0 as

$$\rho^0 = \begin{pmatrix} \rho^0 & 0 & 0 \\ 0 & \rho^0 & 0 \\ 0 & 0 & \rho^0 \end{pmatrix} . \tag{3.9}$$

From the second step, we use the linear approximation method of the resistances. Each tensor element is treated separately in the procedure. A resistance depending on the six fitting parameters can be represented by

$$R(\rho_{xx},\rho_{yy},\rho_{zz},\rho_{xy},\rho_{yz},\rho_{xz}) = R^0(\rho^0_{xx},\rho^0_{yy},\rho^0_{zz},\rho^0_{xy},\rho^0_{yz},\rho^0_{xz}) + \sum_{i<j} A_{ij}\Delta\rho_{ij} \ , \tag{3.10}$$

where R^0 is a resistance determined by the resistivity tensor ρ^0 given by a previous step. The linear expansion of the resistances can be defined by

$$\rho_{ij} = \rho^0_{ij} + \Delta\rho_{ij} \quad , \quad A_{ij} = \left(\frac{\Delta R}{\Delta\rho_{ij}} \right) = \frac{R(\rho^0_{ij} + \Delta\rho_{ij}) - R(\rho^0_{ij})}{\Delta\rho_{ij}} . \tag{3.11}$$

Selecting $\Delta\rho_{ij}$ is somewhat arbitrary depending on the functional shape around the tensor ρ^0_{ij}. The constant A_{ij} can be given by taking the numerical derivative of the resistance.

Then the resistances in Eq. (3.10) can be fitted with the experimental values to find a conductivity tensor that minimizes the χ^2 of the resistances. By continuing this process until the best optimum point is achieved, the anisotropic conductivity tensor and contacts can be given. This is the main idea of this algorithm.

Next, I explain the way to save one fitting procedure in the first step. Each iteration in this simulation requires a heavy computer job; sometimes it is very efficient to skip one iteration. Previously, I consider only an isotropic tensor in the first step for the rescaling of the resistivity. However, an anisotropic tensor also can be used for the rescaling and the determination of each tensor term simultaneously in the first step. First, I will describe the skip for a diagonalized tensor. It will be explained for a general tensor later. Suppose we have a diagonalized tensor. Then, we have only three unknown variables in a tensor. A resistance can be represented by a geometrical factor Γ_0 and some constants B_{ij} as in Eq. (3.12).

$$R(\rho_{xx},\rho_{yy},\rho_{zz})=\Gamma_0\left[\frac{\rho_{xx}+\rho_{yy}+\rho_{zz}}{3}+B_{xx}\rho_{xx}+B_{yy}\rho_{yy}+B_{zz}\rho_{zz}\right] . \qquad (3.12)$$

Since a resistance R should be equal to Γ_0 for the unit tensor ($\rho_{xx}=\rho_{yy}=\rho_{zz}=1.0$), a relation between three coefficient B_{ij} can be found by

$$B_{xx}+B_{yy}+B_{zz}=0 \ . \qquad (3.13)$$

Then Eq. (3.12) can be simplified as

$$R(\rho_{xx},\rho_{yy},\rho_{zz})=\Gamma_0[\langle\rho\rangle+B_{yy}(\rho_{yy}-\rho_{xx})+B_{zz}(\rho_{zz}-\rho_{xx})] , \qquad (3.14)$$

where

$$\langle \rho \rangle = \frac{\rho_{xx} + \rho_{yy} + \rho_{zz}}{3}. \tag{3.15}$$

One coefficient B_{xx} has been removed from Eq. (3.12) using Eq. (3.13). If we define new parameters of χ_{ij} and B_{ij} by

$$\chi_{ij} = \frac{\rho_{jj} - \rho_{ii}}{\langle \rho \rangle} \quad , B_{ij} = \Gamma_0 \left(\frac{\Delta R}{\Delta \rho_{ij}} \right) - \frac{1}{3} , \tag{3.16}$$

then we have a relation between a resistance and the fitting parameters $\langle \rho \rangle$ and χ_{ij}.

$$R(\rho_{xx}, \rho_{yy}, \rho_{zz}) = \Gamma_0 \langle \rho \rangle [1 + B_{yy}\chi_{xy} + B_{zz}\chi_{xz}] \tag{3.17}$$

In the first step, the rescaling is done by $\langle \rho \rangle$ while χ_{ij} provides the separation of each tensor element. If the off-diagonal terms are considered as well, this relation can be generalized by adding some extra terms ξ_{ij} associated with off-diagonal terms in Eq. (3.12).

$$R(\rho_{xx}, \rho_{yy}, \rho_{zz}, \rho_{xy}, \rho_{yz}, \rho_{xz}) = \Gamma_0 \langle \rho \rangle [1 + B_{yy}\chi_{xy} + B_{zz}\chi_{xz} + B_{xy}\xi_{xy} + B_{yz}\xi_{yz} + B_{xz}\xi_{xz}], \tag{3.18}$$

where new parameters of ξ_{ij} can be defined by

$$\xi_{ij} = \frac{\rho_{ij}}{\langle \rho \rangle}. \tag{3.19}$$

So we have six fitting parameters ($\langle \rho \rangle$, χ_{xy}, χ_{xz}, ξ_{xy}, ξ_{yz}, ξ_{xz}) in the resistances with six geometrical factors (Γ_0, B_{yy}, B_{zz}, B_{xy}, B_{yz}, B_{xz}) calculated at the starting point. However, this amended first step has been used only for especially heavy computer jobs in the real simulation. Usually I applied the simple algorithm for the first step given by Eq. (3.8).

In each iterative step, we minimize χ^2 of the experimental resistances R^e and the theoretical resistances $R^t(\tilde{\rho}, r_j)$. The theoretical resistances can be given by a resistivity tensor $\tilde{\rho}$ and the contact resistances r_j as in Eq. (3.5).

$$\chi^2 = \sum_i \left[\frac{R_i^e - R_i^t(\tilde{\rho}, r_j)}{\sigma_i} \right]^2 , \qquad (3.20)$$

where i denotes the index of all data and σ_i is the standard deviation of each experimental measurement. We used Levenberg-Marquardt method to minimize χ^2 to determine the unknown parameters (six terms in a resistivity tensor and the contact resistances).[23]

3.2.3 orthogonal transformation

After the iteration, an optimized conductivity tensor is obtained. However each element in this tensor varies under the rotation of the coordinate; it is changed for different coordinate systems. So, the principal axes and diagonal elements should be obtained. The sample properties are characterized by these invariant quantities. A symmetric conductivity tensor in Eq. (3.3) is a Hermitian matrix that has three real eigenvalues and three orthogonal eigenvectors.[36] Three eigenvalues (principal values) and eigenvectors (principal directions) of the matrices can be determined by doing the orthogonal transformation on the tensor.

$$\tilde{\sigma} = \begin{pmatrix} \sigma_{11} & \sigma_{12} & \sigma_{13} \\ \sigma_{12} & \sigma_{22} & \sigma_{23} \\ \sigma_{13} & \sigma_{23} & \sigma_{33} \end{pmatrix} \Rightarrow \begin{pmatrix} \sigma_{11}^p & 0 & 0 \\ 0 & \sigma_{22}^p & 0 \\ 0 & 0 & \sigma_{33}^p \end{pmatrix} , \qquad (3.21)$$

To identify the principal axes and values, we solve an eigenvalue problem of the tensor σ_{ij}.

$$\vec{\vec{\sigma}} \cdot \vec{x}_i = \lambda_i \vec{x}_i \ , \tag{3.22}$$

where λ_i is an eigenvalue that denotes a conductivity and $\vec{x}_i$ is an eigenvector for the eigenvalue.

3.3 Computer Simulation

3.3.1 sample geometry

First, I have counted how many leads are needed on the sample for enough information to determine the tensor. Most fittings in this chapter have been done with only 4-terminal measurements to obtain the tensor. The contact resistances were not considered in most cases. In the previous chapter, the fitting with 4-terminal terms turned out to give a better result than the fitting with whole terms including 2-point, 3-point terms. The isotropic tensor can be determined by four leads since the tensor has single unknown parameter that is fewer than the independent 4-terminal terms. However, the number of the unknowns is increased for an anisotropic tensor, so we may need more leads. Moreover, it is hard to form many contacts on some samples. Therefore, it is important to know what is the minimum number of the contacts necessary to reconstruct the conductivity tensor. Since there are six unknown parameters in the tensor now, we should have more than six independent 4-point resistances. Following the argument in Appendix A.2, we should have at least six leads on the sample. To identify the contact

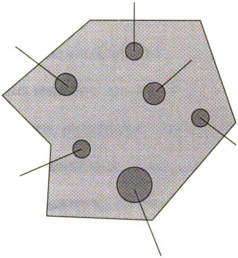

(a)

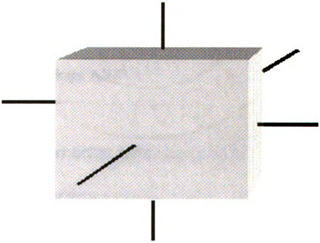

(b)

Figure 3.3 Many probes are attached on the surface of samples in 2d (a) and 3d (b). More contacts are needed for anisotropic conductivity tensor compared to isotropic conductivity tensor.

resistances also, we need six leads. Now there are $6+n$ unknowns (6 tensor terms and n contact resistances) and this number should be less than ${}^{n}C_{2}$ $(=n(n-1)/2)$ that is the number of the independent terms in a resistance table. Therefore, we need six leads in both cases whether the contact resistances are fitted or not.

To illustrate this technique, we generated computer models in 2d and 3d as shown in Figure 3.3. Six surface probes were formed on the sample both in 2d and 3d. By the counting argument of the 4-terminal terms, only five probes were enough to determine three tensor elements in 2d. Six circular contacts of different sizes were formed in the 2d planar sample and six identical small bricks of contact pads were attached on the surface of the large brick of 3d sample. The contacts were randomly distributed on the 2d sample, but for the 3d sample, the six contacts were attached one on each facet. A 2d sample was meshed by ~3000 brick elements (DC2D4 in ABAQUS) and a 3d sample was by ~5000 tetrahedral elements (DC3D10). Modeling (generating geometry and meshes) was done again by the commercial package ANSYS.[24]

3.3.2 simulated experimental data using FEM

To test my method for these computer models, I generated simulated resistance tables. An anisotropic conductivity tensor has been arbitrarily selected to generate the simulated resistance table. By performing the FEM with this prescribed tensor, I obtained a 15 x 15 resistance table constructed by all possible voltage and current measurements. With this tensor, the contact resistances were added to the sample resistances. Only Ohmic contacts were considered for this test sample. Moreover, to simulate the real experimental measurement, the resistance table was decorated by Gaussian noise. This simulated resistance table was used as experimental resistances to test how our method could find the prescribed tensor and contact resistances. A commercial package ABAQUS[25] was used for the analysis.

3.3.3 iterative linearization fitting using FEM

In each iteration, the resistance calculation using FEM was done by the fitted conductivity tensor obtained from the previous step. And these resistances were fitted with the experimental values again to determine another tensor for the next step. In each step, I calculated the whole resistances $R_{ij}^{lm}(\rho_j)$ (225 terms) using the fitted conductivity tensor ρ_j given from the previous step. And some other resistances $R_{ij}^{lm}(\rho_j+\Delta\rho_j)$ were calculated to obtain the linear expansions of A_{ij} in Eq. (3.11) or B_{ij} in Eq. (3.16).

$$A_{ij}=\frac{\Delta R_{ij}^{lm}}{\Delta\rho_j}\,, \tag{3.23}$$

$$B_{ij}=\Gamma_0\left(\frac{\Delta R_{ij}^{lm}}{\Delta\rho_j}\right)-\frac{1}{3}\,, \tag{3.24}$$

$$\frac{\Delta R_{ij}^{lm}}{\Delta\rho_j}=\frac{R_{ij}^{lm}(\rho_j+\Delta\rho_j)-R_{ij}^{lm}(\rho_j)}{\Delta\rho_j} \tag{3.25}$$

The least square fitting could be done in each step using numerical derivatives given by the FEM. The whole table or only 4-terminal terms were used for the fitting. After approaching close to an optimum point, the iteration was stopped. The fitted conductivity tensor and contact resistances were compared with the initially given quantities. While the fitting was done iteratively, I obtained a diagonalized conductivity tensor by the orthogonal transformation. The diagonalized tensor showed the principal axes of the tensor and the principal values along the principal axes.

3.4 Experiment

3.4.1 sample preparation (Bi cylinder)

A test of this method has been performed on a bismuth cylinder. As shown in Table 3.1, bismuth has an anisotropic resistivity tensor. It has two distinguishable principal directions: one ($\rho_p = \rho_1 = \rho_2$) is the isotropic on xy-plane and the other (ρ_3) is perpendicular to the plane. Later, I will call the ρ_p a planar resistivity and ρ_3 a perpendicular resistivity. This property comes from its trigonal lattice structure. The planar resistivity component is known to be 109.0 (10^{-6} Ω-cm) and the perpendicular component is 138.0 (10^{-6} Ω-cm). The discrepancy between these two elements is about 40%; this number is larger than the possible error estimations of the measurement or the simulation. In Figure 3.4, I display the geometry of our test sample. It is a relatively thin cylinder that may be treated as a circular plate. Its diameter is 10.4mm and thickness is 2.0mm. Six gold electrodes were formed on both circular planes of the sample by the evaporation technique. All the contact areas were circular (diameter : 1.0mm). Three contacts were formed on the top, the others were formed on the bottom. Three pads on a plane were rotated by some angle from the other three pads (see Figure 3.4(b)). Otherwise, we would have measured extremely small 4-point resistances that might have caused some serious numerical error. Usually the symmetric formations of contacts raise

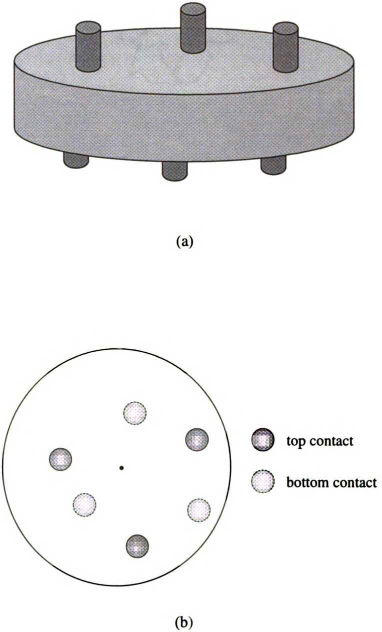

Figure 3.4 Schematics of a real sample (Bi cylinder) with six circular Au electrodes. (a) It is a relatively thin cylinder. Three contact pads were formed on each circular plane of the sample. (b) Three pads on a plane were formed to have an angle from three pads on the other plane.

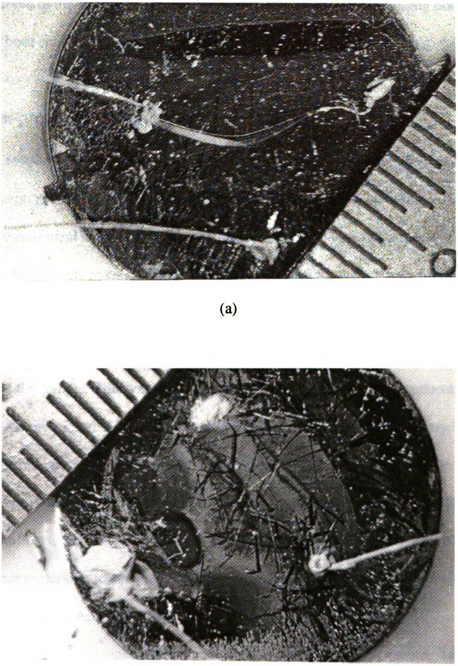

(a)

(b)

Figure 3.5 The normal photos of the Bi sample for the real measurement.[37] It has six contacts that are formed on both sides of the circular planes. (a) and (b) show the formation of contacts on these two sides. The ruler shows the size of the sample.

the errors in the simulation because of the sensitivity of the 4-terminal resistances that has been observed in the isotropic case. The geometry was constructed by taking normal photos of both sides of the sample as given in Figure 3.5.

3.4.2 six-probe measurement

A resistance table (15 x 15) was obtained by all possible voltage and current measurement. A total of 225 terms were obtained in a resistance table. Only 90 terms of 4-point measurement would be used in the fitting since the contact resistances were not concerned for this real material. DC current has been used for the *I-V* measurement on the sample. It was important to use low currents to remove the thermoelectric effect of the high conductivity sample. Each 4-point resistance was measured to check the Ohmic property of the sample. This was really important to check whether the conductance was related to the thermoelectric effects. Thermoelectric effects break the symmetry in the 4-point measurement. So, if these effects are significant in the measurement, their contributions to the resistances should be considered separately. With several different DC current flows, the *I-V* curves for all 4-terminal measurements were obtained and fitted by the linear regression technique to find the derivatives that were equivalent to the 4-terminal resistances. Among 90 terms, some measurements showed bad *I-V* characteristics. Some 4-point measurements were observed to be asymmetric. These terms were removed from the final data since I had enough data in the table. The asymmetry might be normal for 2-point and 3-point resistances because of the non-Ohmic contacts. However, 4-point resistances should not be asymmetric if the conductance is only electrical. That asymmetry might be from the thermoelectric conductance. However, that effect has been neglected throughout this work based upon the asymmetry was not substantial. So, the 4-point resistances were symmetrized by taking the average of two off-diagonal elements. Finally, this refined resistance table was used to determine the conductivity tensor elements of the Bi sample.

3.5 Analysis

3.5.1 computer generated sample (2d)

Our method has been tested on a 2d computer model in Figure 3.6. That irregular plane has six circular probes. Figure 3.6(a) shows the meshed structure and Figure 3.6(b) presents a voltage distribution on the sample for a measurement given by the FEM analysis. Table 3.2 shows the prescribed and the fitted conductivity tensors. The fitting procedures were done by whole resistance table and 4-terminal resistances only. The second row represents the conductivity elements that have been used to generate the

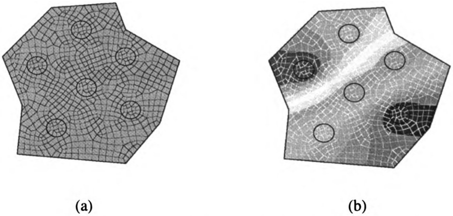

(a) (b)

Figure 3.6 A computer generated sample for the determination of anisotropic conductivity. This 2d computer model has six circular probes. The contour map (b) shows the equipotential lines. The meshing was done by ANSYS and the analysis was done by ABAQUS.

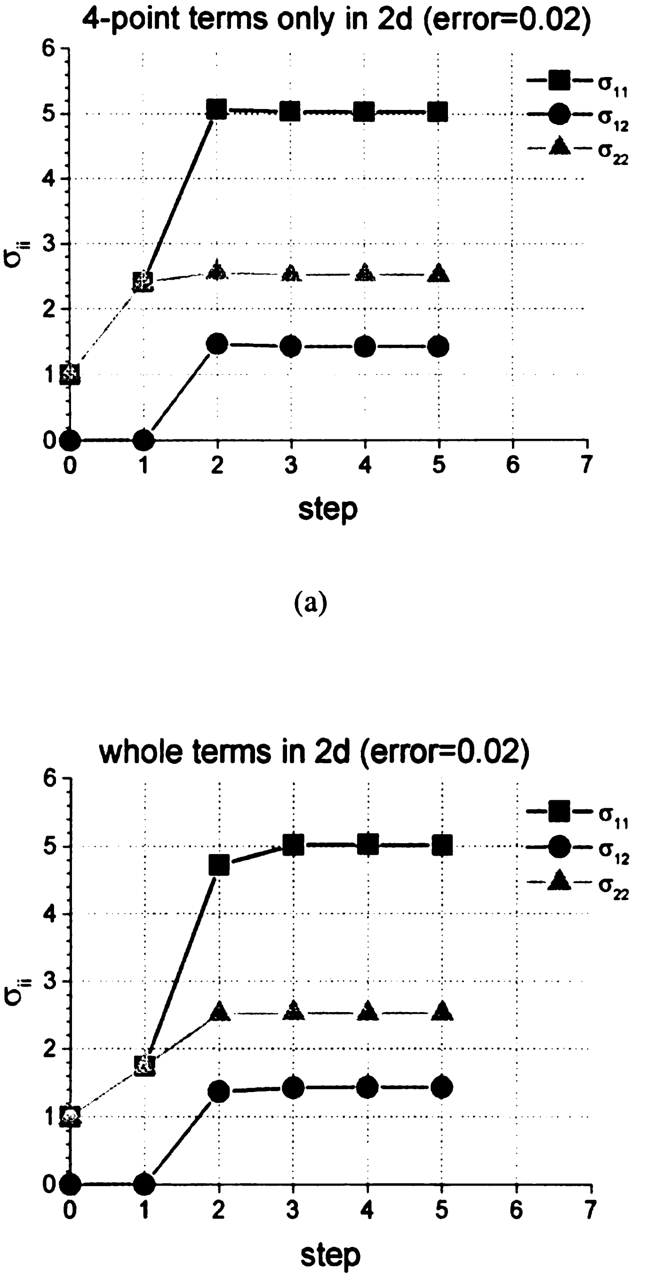

(a)

(b)

Figure 3.7 These figures show the fitting procedures of the tensor in 2d. The fittings were performed using only 4-point resistances (a) or whole resistances in the table (b). Three data points are equivalent to three conductivity tensor terms.

Table 3.2 The comparison of the fitted results of the conductivity tensor elements with the prescribed values for the computer model in 2d.

	σ_{11}	σ_{12}	σ_{22}
Prescribed	5.00	1.40	2.50
4-point terms (a)	5.03	1.42	2.52
Whole terms (b)	5.01	1.43	2.52

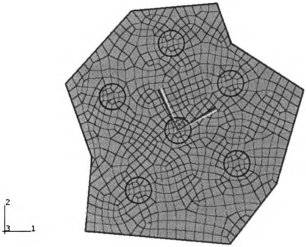

Figure 3.8 Two principal directions were drawn on the surface of 2d computer model. Three directions (one real and two fitted) represent a remarkable coincidence.

simulated resistances. We compared the fitted results in the table with the predefined tensor. In both cases, our method reproduced the real values remarkably within acceptable error levels that were associated with the Gaussian noise. For this 2d sample, 2% of noise had been added to the resistances to simulate the experimental measurement. Figure 3.7 shows the fitting procedures for two data sets (4-point terms (a) and whole terms (b)). Usually the iterations were observed to be stabilized just after a few steps.

The orthogonal transformations were done to diagonalize the fitted tensors. Two principal values and two principal directions equivalent to the values were given for the real tensor and two fitted tensors. The diagonalized tensors and the principal vectors of each tensor were presented in Eq. (3.26)~(3.28). Eq. (3.26) came from the prescribed tensor and the rest came from the fitted tensor. These principal directions in each case were shown on the surface of the model as in Figure 3.8.

$$\sigma_0 = \begin{pmatrix} 5.627 & 0.000 \\ 0.000 & 1.873 \end{pmatrix}, \qquad \begin{matrix} \vec{x}_1 = (0.913 \quad 0.409) \\ \vec{x}_2 = (-0.409 \quad 0.913) \end{matrix}. \tag{3.26}$$

$$\sigma_a = \begin{pmatrix} 5.67 & 0.00 \\ 0.00 & 1.88 \end{pmatrix}, \qquad \begin{matrix} \vec{x}_1 = (0.912 \quad 0.411) \\ \vec{x}_2 = (-0.411 \quad 0.912) \end{matrix}. \tag{3.27}$$

$$\sigma_b = \begin{pmatrix} 5.66 & 0.00 \\ 0.00 & 1.87 \end{pmatrix}, \qquad \begin{matrix} \vec{x}_1 = (0.910 \quad 0.414) \\ \vec{x}_2 = (-0.414 \quad 0.910) \end{matrix}. \tag{3.28}$$

3.5.2 computer generated sample (3d)

I did another test simulation on a 3d computer model with six probes. A meshed structure of the sample and the voltage distribution on the surface were presented in Figure 3.9(b). The predefined conductivity tensor and the fitted results were given in

Table 3.3. Since we have six terms in a tensor, the number of the fitting parameters is also six. Two different fittings with different fitting data (4-point terms and whole table) were done again for this 3d sample. These results by two different data sets (4-point (a) and whole table (b) in Figure 3.10) showed a good agreement with the predefined tensor elements. The errors in the results might be acceptable, although they came out higher than in 2d case. 2% Gaussian noise had been added to generate the simulated resistances. Usually a few more steps were needed to reach to the optimum solution compared to the 2d case. It is simply because of the increase of the fitting parameters in 3d. From these graphs, I realized that the first a few steps were critical in the entire process. The rest of the iterations did not improve the results in most cases. I obtained the principal values and axes of the conductivity tensor by diagonalizing the fitted tensor. Eq. (3.29) shows the diagonalized tensor of the prescribed conductivity tensor and the principal vectors. And Eq. (3.30) and (3.31) were given from the fitted tensors by 4-point terms and whole resistances respectively.

Table 3.3 The comparison of the fitted results of the conductivity tensor elements with the prescribed values for the computer model in 3d.

	σ_{11}	σ_{12}	σ_{22}	σ_{13}	σ_{23}	σ_{33}
Prescribed	8.0	-0.8	11.0	1.5	-0.5	9.0
4-point terms (a)	7.640	-0.817	10.19	1.521	-0.613	9.604
Whole terms (b)	7.845	-0.811	10.24	1.619	-0.552	9.366

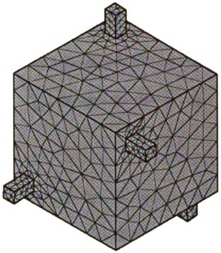

(a)

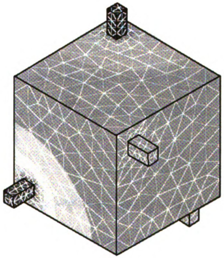

(b)

Figure 3.9 The meshing (a) and equipotential lines (b) of a 3d computer generated sample. Six brick-shaped probes were formed on six facets of the sample.

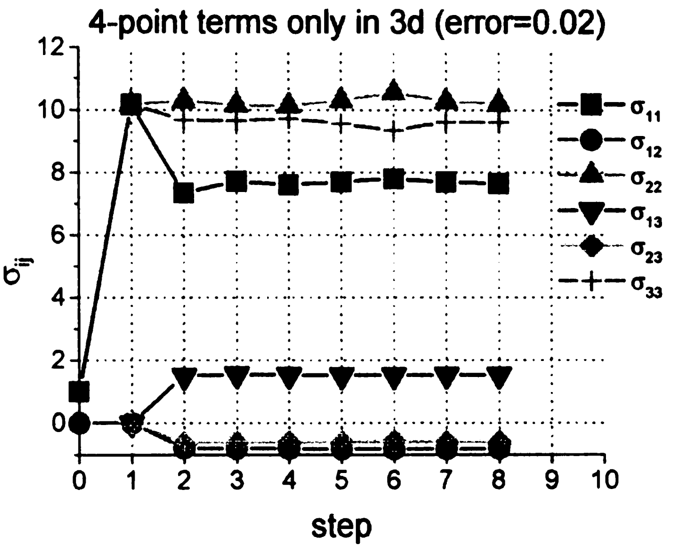

(a)

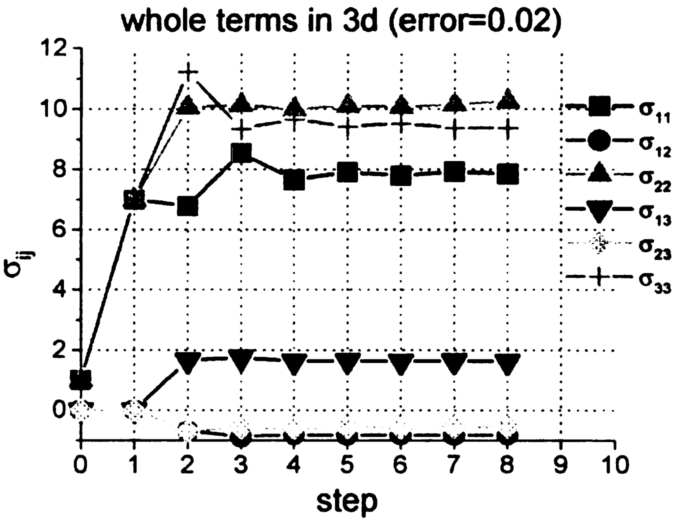

(b)

Figure 3.10 These figures show the fitting procedures of the tensor in 3d. The fittings were performed using only 4-point resistances (a) or whole resistances in the table (b). Six parameters in a tensor were obtained each step. The iterations in 3d needed a few more steps to the optimum than in 2d.

$$\sigma = \begin{pmatrix} 6.89 & 0.00 & 0.00 \\ 0.00 & 11.55 & 0.00 \\ 0.00 & 0.00 & 9.57 \end{pmatrix}, \quad \begin{aligned} \vec{x}_1 &= (0.822 \quad 0.0916 \quad -0.562) \\ \vec{x}_2 &= (-0.352 \quad 0.857 \quad -0.376) \\ \vec{x}_3 &= (0.447 \quad 0.507 \quad 0.737) \end{aligned} \tag{3.29}$$

$$\sigma_a = \begin{pmatrix} 6.76 & 0.00 & 0.00 \\ 0.0 & 11.27 & 0.00 \\ 0.00 & 0.00 & 9.41 \end{pmatrix}, \quad \begin{aligned} \vec{x}_1 &= (0.886 \quad 0.131 \quad -0.445) \\ \vec{x}_2 &= (-0.411 \quad 0.666 \quad -0.622) \cdot \\ \vec{x}_3 &= (0.215 \quad 0.734 \quad 0.644) \end{aligned} \tag{3.30}$$

$$\sigma_b = \begin{pmatrix} 6.77 & 0.00 & 0.00 \\ 0.00 & 11.24 & 0.00 \\ 0.00 & 0.00 & 9.44 \end{pmatrix}, \quad \begin{aligned} \vec{x}_1 &= (0.854 \quad 0.119 \quad -0.507) \\ \vec{x}_2 &= (-0.441 \quad 0.682 \quad -0.583) \cdot \\ \vec{x}_3 &= (0.277 \quad 0.722 \quad 0.635) \end{aligned} \tag{3.31}$$

The sensitivity test of our method has been performed for several simulated resistance tables that were generated by different noise levels. I monitored how the errors in the fitted results were related to the noise levels and shown in Figure 3.11. It shows two curves that correspond to the fitting data of whole table and 4-point terms. They turned out basically linear as expected, but the derivatives were quite different. The derivative of the fitting with whole table was somewhat higher than the fitting with 4-point terms only. This result seems to support the argument that the fitting with 4-point is more efficient than the fitting with whole table in the determination of the anisotropic tensor.

3.5.3 real sample (Bi cylinder)

The test for a real material has been done by two different meshings for the same geometry. Figure 3.12 presents one meshed sample and the voltage distributions of the Bi cylinder obtained by the FEM analysis. Two figures obtained from different view angles show the voltage distribution on the top and side of the sample. Notice that whole contacts were given as equipotential regions since the six small cylindrical contact pads

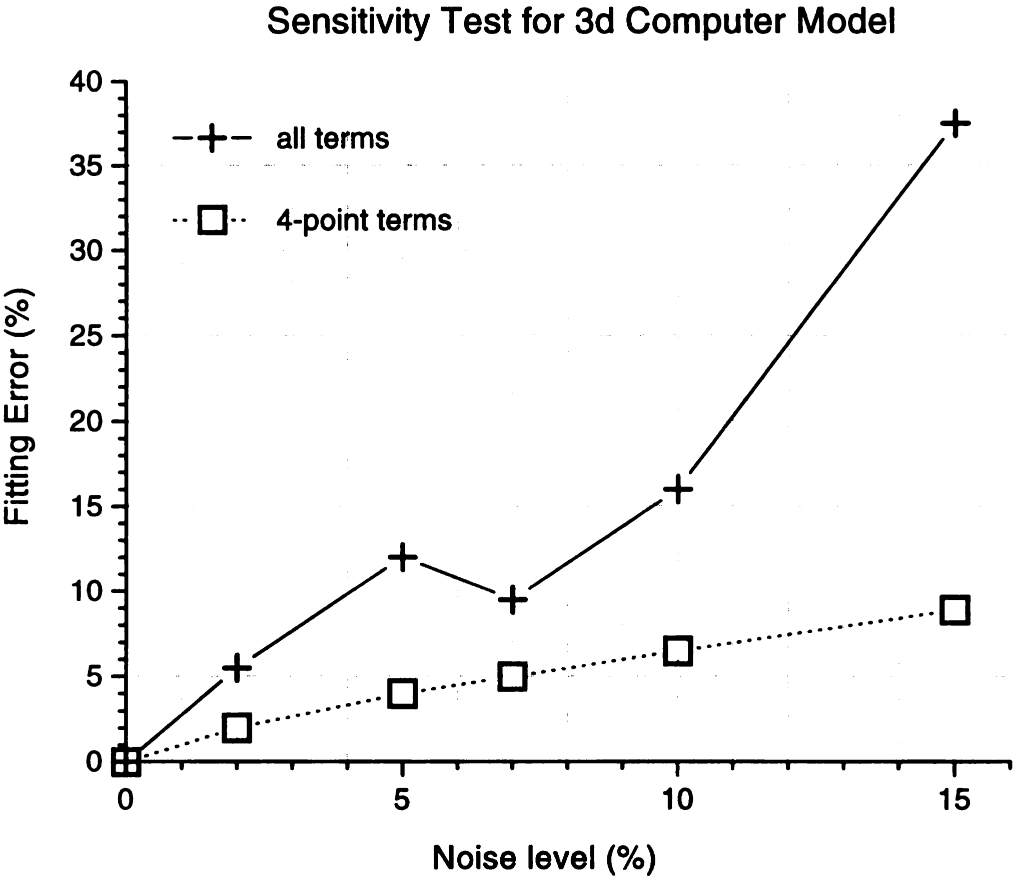

Figure 3.11 Sensitivity test of the conductivities fitted by 4-point terms and whole table has been done to check the relation between the result and the Gaussian noise.

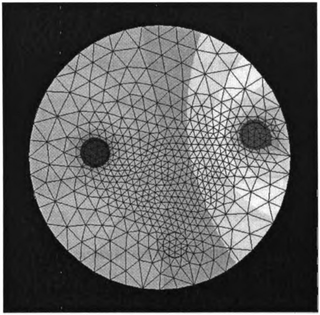

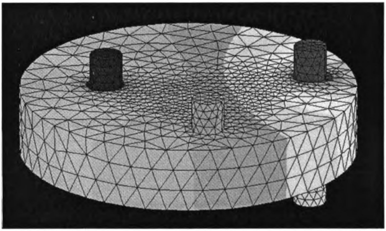

Figure 3.12 Equipotential lines of the real sample (Bi) obtained by FEM analysis.

were perfect conductors. The well-known conductivity elements of Bi and the fitted results by our technique are presented in Table 3.4. And the fitting procedures of two different meshings were shown in Figure 3.13(a) and (b). The real conductivity components (planar (109.0) and perpendicular (138.0)) of the Bi sample were represented by the two horizontal solid lines in the figures. In this test, only 4-terminal resistances were used in the fitting according to the argument in the previous tests. It has been realized that the fitting with 4-terminal terms was more effective than the fitting with whole table. Since the orthogonal transformation has been done in each step, I have only three data points in the figures. Three points correspond to the three principal components of the conductivity tensor. The errors of the fitted conductivities were measured relatively high compared to the results of the computer models. This result might be acceptable when the experimental and simulation error levels are considered. However, the separation between the planar and perpendicular components is not so clear in the results. If I take the average of two planar resistivity values (98.75, 126.3), it is given by 112.52 that agrees remarkably with the real value (109.0). However, these two components never crossed over in the entire fitting procedures. The separation between these two planar components was quite substantial. Moreover, the fluctuations of the fitted components

Table 3.4 Principal values of the resistivity of Bi. (10^{-6} Ω cm)

	ρ_{11}	ρ_{22}	ρ_{33}
Real Sample (Bi)	109.0	109.0	138.0
Fitted result	98.75	126.3	152.1
Error (%)	9.4	15.9	10.2

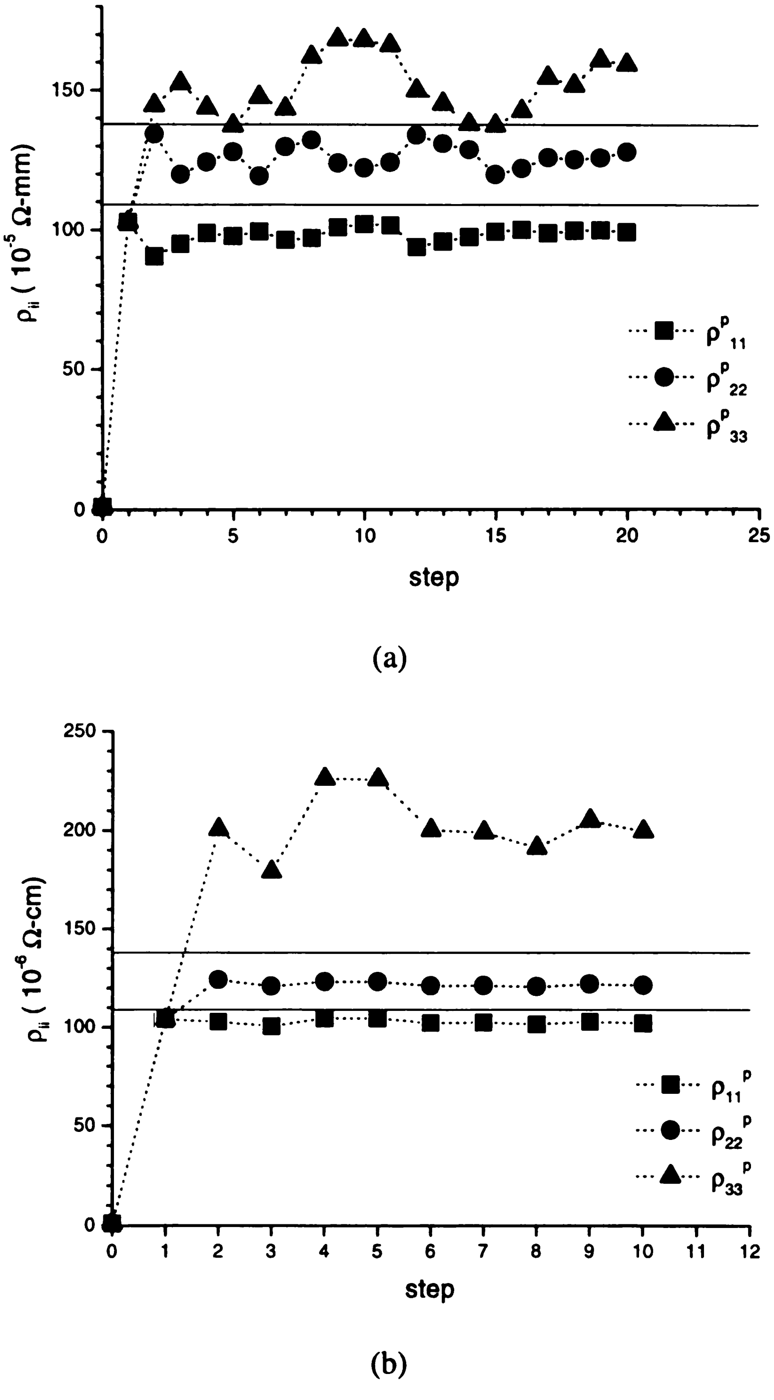

Figure 3.13 Fitting procedures of a resistivity tensor of the real sample. Two meshings were used to test our method on this sample. Only three principal components of the tensor were shown in these pictures. Two planar resistivity components (solid circle and square) are observed stable around the real value, but the perpendicular component (triangle) shows a substantial variation, especially in (b).

were observed to be significant in both fitting procedures as in Figure 3.13. By the comparison of two fitting procedures, the fluctuation of the perpendicular component was more serious than the other two planar components.

The experimental errors were believed not to exceed 10%. So, there must be some other considerable error sources in this method. One of the main error sources might be the incorrect geometry reconstruction of the sample. Therefore, in next section, I will describe various stability tests to investigate the possible error sources, the meshings and the geometry reconstruction.

3.5.4 stability test

First, I selected several different sizes and types of elements for the meshing and checked if the fitted results depend on the way of meshings. The characteristics of all meshings used in this test were presented in Table 3.5. I ran the algorithm with these meshings to obtain the anisotropic conductivity tensors. The fitting procedures were given in Figure 3.14. The planar components (solid square and circle) fluctuate slightly around the real value (109.0) that is denoted by the lower solid line for all meshings, but the variation of the perpendicular component is quite significant. Therefore, I realized that a finer meshing did not improve the fitting result so much. The variation of the perpendicular component was quite substantial in the simulation.

The other test has been done to find the dependence of the result on the positions of the contact pads. I built up several structures that had contact pads on slightly different positions by rotating three pads on a plane. The fitted results by these different structures were presented in Figure 3.15. It was observed that even small rotations (2° ~ 5°) could give substantial differences to the results. Interestingly, the two planar components were found to cross over at some degree between 2° and 5°. And the perpendicular component was observed fluctuating significantly. It should be emphasized that the geometry reconstruction is very important especially in anisotropic case.

Meanwhile, I tried to understand why the perpendicular component ρ_3 was not accurate and showed a serious instability. I thought that the error might be related to the thickness of the sample. To verify this, another test was done for two identical computer models except for the thickness. One model (Cylinder 1) was the same shape of the Bi sample and the other one (Cylinder 2 in Figure 3.16) had different thickness that was 5mm (note that the thickness of Cylinder 1 was 2.0mm). Both samples had six probes at same positions. I generated the simulated resistances for each model as done before. A meshing (Bi10-1) was used to generate the resistances of Cylinder 1 and a different meshing (Bulk10-1) was used for Cylinder 2. I further tested if the technique could reproduce the prescribed conductivity components. I used the four meshings described in Table 3.6 including the meshing that was used to generate the simulated resistances. In Figure 3.17, the perpendicular component for the thin sample (Cylinder 1) could not be

Table 3.5 Different meshings for the stability test of a cylindrical sample.

Meshing	Bi10-1	Bi10-2	Bi4-1	Bi4-2
Element type	DC3D10	DC3D10	DC3D4	DC3D4
Nodes per elements	10	10	4	4
Total Nodes	4473	1744	2445	728
Number of elements	2492	908	9809	2492

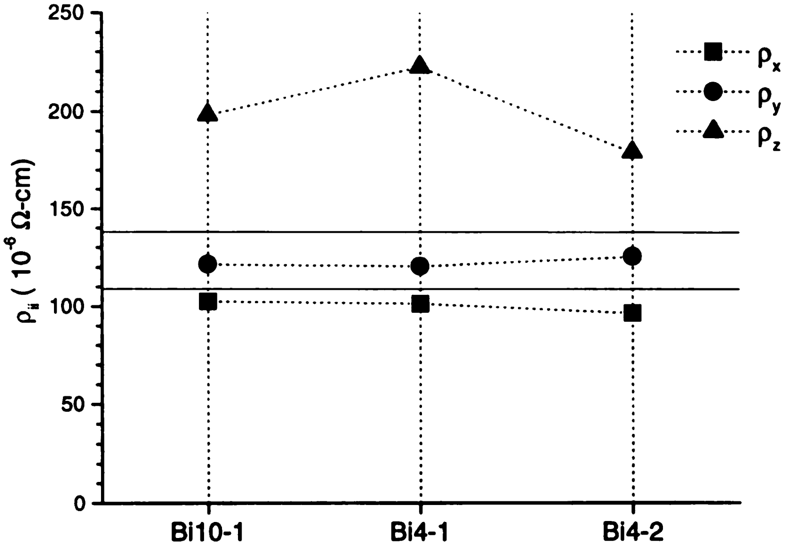

Figure 3.14 Resistivity fittings were done for the Bi sample using three different meshings. Bi10-1 is a fine meshing and Bi4-2 is a rough meshing. It turned out that the perpendicular resistivity component was so sensitive on the meshing while the other components were stable.

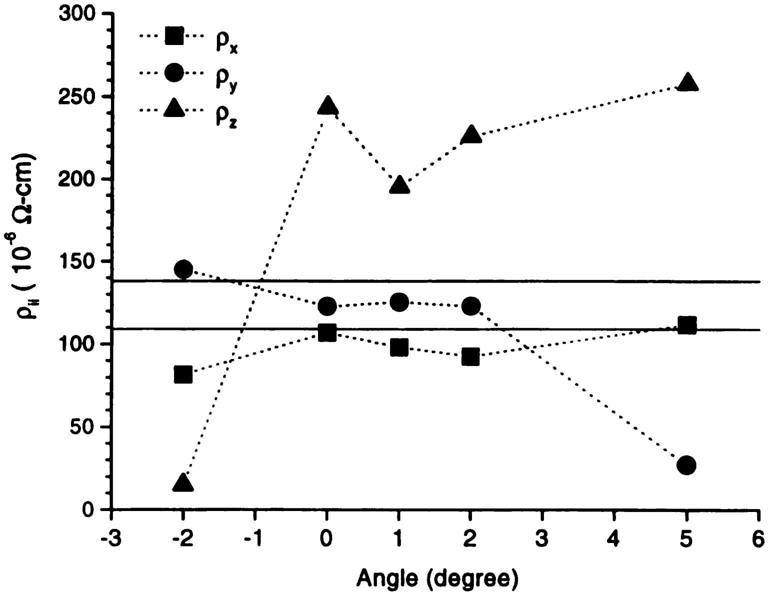

Figure 3.15 Resistivity fittings were performed on some modified structures. The modifications were done by rotating the contact pads. The dependence of the result on the angles was shown in the figure. Huge variations were observed for all components. Interestingly, two planar resistivity components (ρ_x , ρ_y) crossed over somewhere between 2° and 5° .

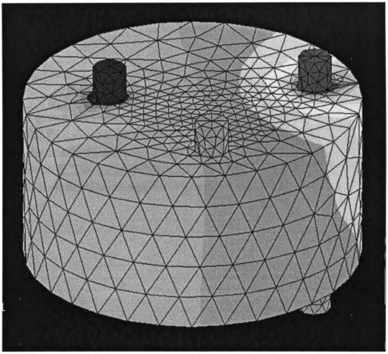

Figure 3.16 Equipotential lines of thicker cylindrical sample (Cylinder 2). This model has more layers of elements along the perpendicular direction. That may enhance the fitting result for that direction.

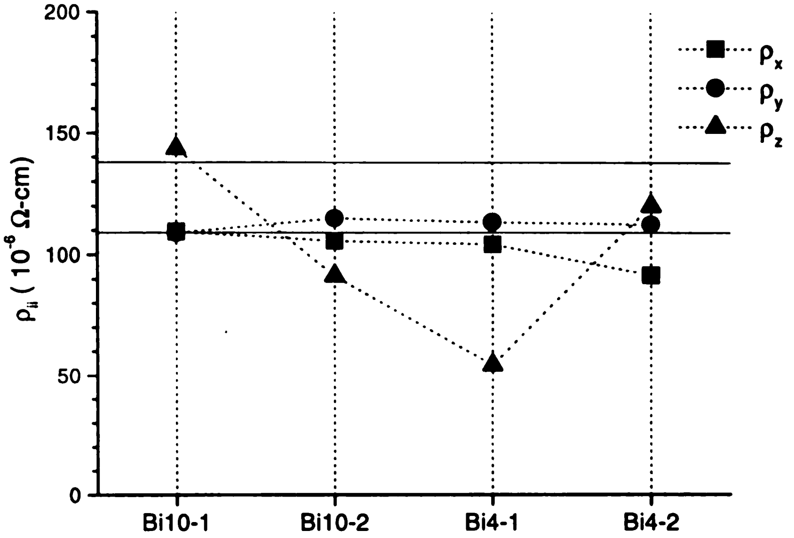

Figure 3.17 This graph was obtained from another computer test for the same geometry of the Bi cylinder (Cylinder 1). The simulated resistances were generated by the meshing Bi10-1. The fitted results from different meshings were presented. The perpendicular component (triangle) shows still a huge variation for this computer model.

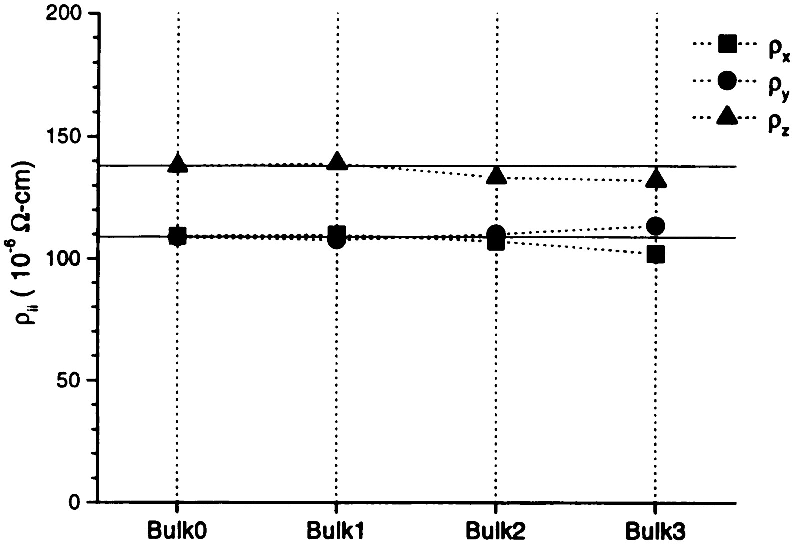

Figure 3.18 Another computer test for a thick sample (Cylinder 2) as shown in Figure 3.16. The simulated resistances were generated by the meshing Bulk10-1. The fitting from other meshings could reproduce the all resistivity components nicely including the perpendicular component.

Table 3.6 Different meshings for the stability test of Cylinder2.

Meshing	Bulk10-1	Bulk10-2	Bulk4-1	Bulk4-2
Element type	DC3D10	DC3D10	DC3D4	DC3D4
Nodes per elements	10	10	4	4
Total Nodes	9359	4473	2445	728
Number of elements	5727	2492	9809	2492

reproduced in some different meshings. For a rough meshing (Bi4-2), a noticeable error was detected for the planar components. However, for the thicker sample (Cylinder 2), all different meshings could reproduce remarkably the prescribed components as shown in Figure 3.18. From this test, I realized that the real Bi cylinder was too thin to have enough information of current path along the perpendicular direction. Most current flows were formed in the horizontal direction. There was no significant current flow into the perpendicular direction, that is required to determine the conductivity component corresponding to the direction. So, I suggest that the sample should be a cube-like shape and the leads should be arranged to detect current paths in all principal directions; otherwise the method may fail to determine all components of an anisotropic tensor.

3.6 Conclusion

In this chapter, I introduced a technique to determine the anisotropic conductivity tensor in complex geometry, which has been generalized from the method for the determination of isotropic conductivity. This method has been tested on computer models in 2d and 3d with arbitrary shape and real material (Bi). Six probes were required to identify the six unknown parameters in a symmetric conductivity tensor. The iterative linearization technique has been adapted to deal with the problem where the resistance in terms of the tensor components were unknown. This method has worked remarkably in the determination of the prescribed conductivity tensor for the computer model. However, for the real sample (Bi cylinder), the technique did not work properly. Some significant errors, especially for the perpendicular component were observed in the resulting conductivity tensors. After some stability tests performed by various computer models, it was realized that the resulting errors were inevitable for such a thin sample. For a test on a computer model that was more cubic, the method turned out to determine the conductivity much better. This technique has been demonstrated for the conductivity measurement, however it can be applied more generally to evaluate other properties. I believe that this algorithm could be used to determine any material property in a complex geometry.

Chapter 4 EFFECTIVE CONDUCTIVITY OF A MEDIUM WITH CIRCULAR INCLUSIONS

4.1 Introduction

In the previous two chapters, I described how to determine a material property (conductivity) using experimental measurement and theoretical calculation. The samples were actually single materials with isotropic or anisotropic conductivities. Only one material (diamond or Bi) was considered in the conductivity determination. The numerical techniques using FEM analysis were introduced and demonstrated to determine the unknown conductivity of samples with a complex geometry. However, in this chapter, my concern is with the (effective) material properties of a *composite material.* The study of material properties of composite materials has been the focus of much research in condensed matter physics, material science, mechanical engineering, and so on. Due to the interests in diverse fields, the study of the effective medium theory on a composite material has been conducted in various ways. Meanwhile, some efforts have been devoted to the investigation of the universal relation between various material properties (electric conductivity, heat conductivity, magnetic permeability, viscosity, even elastic constants) of the materials. Analytic approaches have been successful in some simple geometries. However, these approaches are usually limited when some complex structures are concerned. Therefore, the numerical analysis should be adapted to study the effective medium theory in more complex geometries. The numerical simulation using FEM could be introduced for this purpose. To check the performance of this method for composite materials, it should be tested on a composite in simple geometry where analytic solutions can be obtained.

In next section, I give a brief background of our study on composite materials. That part describes how the research has been done historically. The motivation of this work is also mentioned. In Section 4.3, the sample geometry is defined such as a composite that includes two hyperspherical inclusions. Two resistances from 4-point and 2-point measurements are defined for the geometry. The analytic solutions and asymptotic forms of the resistances are described, too. The computer simulations using FEM method are introduced and performed to calculate the resistances numerically in Section 4.4. The numerical results are presented and compared with the analytic solutions in Section 4.5.1(2d) and 4.5.2(3d). Furthermore, the relations between the 4-point and 2-point measurement in the geometry are obtained and discussed in Section 4.5.3. I will close this chapter by presenting the conclusion and suggestions in Section 4.6

4.2 A brief history of the study on a composite material

The study of the properties of random mixtures containing a low fraction of inclusions has been of much interest since Maxwell's study of a system of spherical inclusions.[38] The dielectric constant of a composite is given by the low volume fraction expansion as

$$\varepsilon = \varepsilon_0 (1 + [\varepsilon] c + O(c^2) + \dots) \ , \tag{4.1}$$

where c is the volume fraction of the inclusions. Here $[\varepsilon]$ is the first order coefficient, as

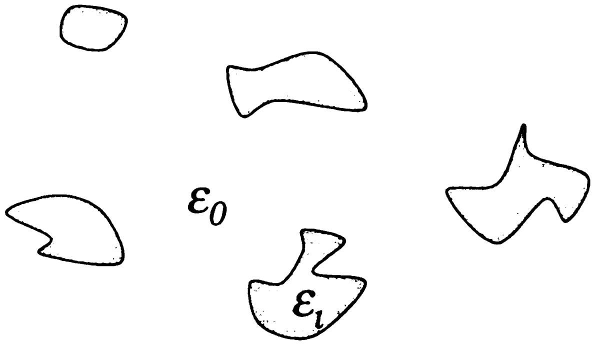

Figure 4.1 A composite material consists of two different dielectric constant regions (ε_0, ε_i) in dilute limit.

given by Maxwell, is for a d-dimensional sphere

$$[\varepsilon] = d\beta \equiv d\left(\frac{\varepsilon_1 - \varepsilon_0}{\varepsilon_1 + (d-1)\varepsilon_0} \right), \tag{4.2}$$

where β, the expansion in brackets, is proportional to the polarisability associated with an isolated spherical inclusion with dielectric constant ε_i in the host medium with dielectric constant ε_0. The $O(c)$ coefficient for the viscosity of a suspension containing a system of hard spheres has been also found by Einstein,[39, 40] although these two do not have universal relations.

Recently, Thorpe obtained the exact results for the $O(c)$ coefficient of electrical conductivity for inclusions of other shapes in 2d using conformal mapping.[41] Hetherington et al.[42] calculated the conductivity of a sheet containing n-sided polygons with sharp corners by solving the integral equations numerically. The results were compared with analytical solutions in the limits when the inclusion is either a hole or a superconductor. Jeffrey used the Batchelor-Green multipole expansion formalism to determine the second order expansion $O(c^2)$ in the problem of dielectric inclusions.[43] Binns and Lawrenson[44] and more recently Djordjevic et al.[45] also studied this problem with the image charge method in 2d, which provided better convergence than the multipole expansion method. Choy et al. showed in a recent paper that the troublesome divergent dipole integral term could be removed and the result agreed completely with the result of Jeffrey and Djordjevic.[46]

This study of random mixtures has been done also for the mechanical properties of composite materials that consist of a host and many inclusions. These studies provided effective mechanical properties as the function of the rigidity of inclusions, the distribution patterns,[47] and the shapes of inclusion. The elastic moduli of a matrix containing circular holes with three different distributions of honeycomb, triangular, and random was studied for the percolation theory of Young's modulus of the composite.[48] It turned out that the relative Young's modulus E/E_0 of a two-dimensional sheer containing circular holes, overlapping or not, is the same for all materials, independent of the Poisson ratio, for any prescribed geometry as a consequence of the CLM theorem.[49] Davis et al. studied the elastic moduli of composite materials consisting of an isotropic, elastic matrix with perfectly rigid circular inclusions near random close packing (see Figure 4.2).[50] This study has been done for the practical reason that the stiffness of rigid fiber inclusions could be enhanced remarkably by arranging them inside a host material.[51] A theory of the bulk modulus was developed by assuming that the elastic energy of the neck regions was minimized subject to the constraint that average local strain was equal to the macroscopic strain. The local strain was approximated by a simple function that depended on the gap distance but not on the surrounding environment, in a concentrated

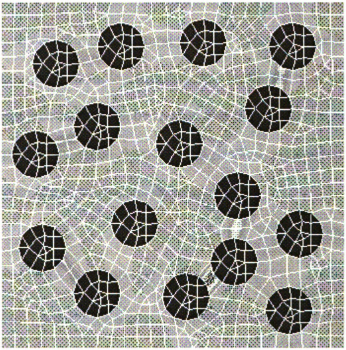

Figure 4.2 Elastic energy distribution in a composite material with many circular inclusions under hydrostatic pressure. The contour map was given by the elasticity analysis using ABAQUS. Elastic energy turned out to be distributed mostly near the necks between two circles.

random array of rigid inclusions in an elastic matrix under hydrostatic deformation in 2d. In that study, a solution of an electric conduction problem for the geometry was applied to solve the elastic problem according to its universal formalism.

However, most analytic solutions of composite materials could be obtained only for simple geometry. For more complicated structures, we should do numerical analysis using computer simulation. The finite element method (FEM) would be one of the most efficient techniques to perform this structural analysis. This technique has been introduced to determine the isotropic and anisotropic conductivity of single materials in the previous chapters. However, it can be applied also to a composite material. To test this method on composite materials, the numerical simulation should be done for a simple composite where some analytic solutions are available.

4.3 Theory

In this section, I provide the analytic solution of the dielectric problem of a composite that has two hyperspherical inclusions. Two resistances in the geometry are defined according to the configurations of voltage and current measurement. The first configuration is that a voltage is applied on the infinite boundaries of the host. Since the host is very large compared to the size of the inclusions, the applied voltage forms constant electric field near the inclusions. A resistance defined for this configuration is called *4-point resistance* since there is no common lead for the voltage and current measurements. The second configuration is that the voltage is applied on the centers of two inclusions. A resistance from this configuration is called *2-point resistance*. The detailed definitions of these resistances will be given in Section 4.3.1 and Section 4.3.2.

In both cases, the resistances (or effective conductivities) can be calculated as a function of the distance between the inclusions. In 2d, exact solutions can be obtained by image charge method [52] and multipole charge method[45] when the inclusions are perfect conductors. In 3d, an empirical approximation and asymptotic solutions are given for the similar composite structure. An interesting feature is given by the comparison of these two resistances. The ratio of the two resistances approaches a constant in the close neck limit.

4.3.1 4-point resistance (R_4)

Consider two circles with radius a in the infinite plane as shown in Figure 4.3. They are separated by L and the neck distance is w. The plane is a normal conductor that has a conductivity σ_0 and the circular inclusions are perfect conductors ($\sigma >> \sigma_0$). Two inclusions are located in a constant electric field E_0 formed by a voltage applied on the boundaries of the host. The voltage between the inclusions is calculated for this geometry. The initial voltage before the formation of the inclusions is given by $E_0 L$. However, if two circular conductors are implanted in this host, they deform the current paths in the region near the inclusions. Then, a voltage change ΔV from the initial value is induced between the two centers of the inclusions.

4.3.1.1 Exact solutions in 2d

Djordjevic et al. solved this problem for perfect conductor inclusions in 2d using the multiple image charge method.[45] The solution is given in closed form by

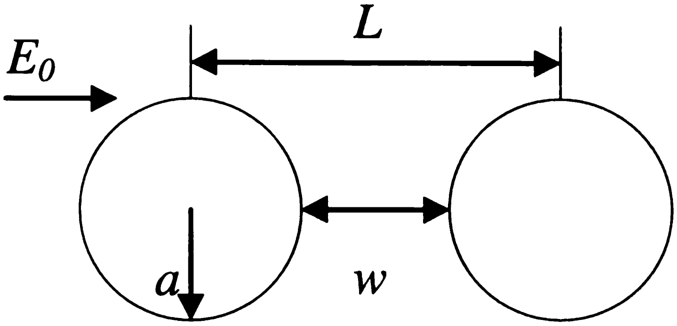

Figure 4.3 4-point resistance measurement of two circular inclusions. The voltage between two inclusions is calculated in terms of the geometrical parameters when a constant electric field is applied.

$$\Delta V = E_0\sqrt{L^2-4a^2} = E_0\sqrt{(w+2a)^2-4a^2} = E_0\sqrt{w(w+4a)} \ , \qquad (4.3)$$

where $L = w+2a$ is the distance between two centers, a is the radius of the circular inclusions. The asymptotic forms of this solution can be checked simply. ΔV approaches $E_0 L$ as L goes to infinity. No voltage difference is measured ($\Delta V = 0$) when two inclusions touch ($L = 2a$).

Besides this induced voltage ΔV, we should have a current to define a resistance for this configuration. Thus, a *normalized current* I_0 has been defined by total current flow into the cross section of the inclusions in the direction of E_0 (see Figure 4.4). The current density J_0 in the host is given by $\sigma_0 E_0$ from Ohm's law. The cross section of the inclusion is given by $2a$ in 2d. Therefore, the normalized current I_0 is given by $2a\sigma_0 E_0$. Thus, from the given ΔV and the new current I_0, a resistance R_4 can be defined by

$$R_4 = \frac{\Delta V}{I_0} \ . \qquad (4.4)$$

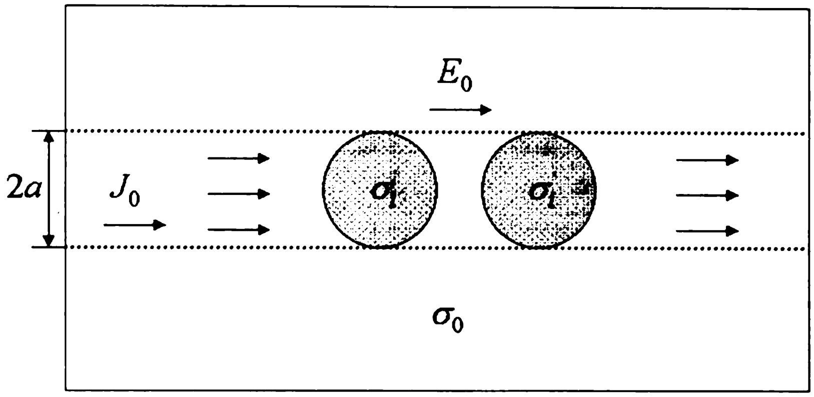

Figure 4.4 Normalized current I_0 is defined by the total current flowing through the cross section of the inclusions.

This resistance is called a *4-point resistance* because it is equivalent to a resistance measured from the 4-point measurement. The 4-point resistance R_4 can be given using the closed form of ΔV in Eq. (4.3) and the normalized current I_0.

$$R_4 = \frac{\Delta V}{I_0} = \frac{E_0\sqrt{w(w+4a)}}{2a\sigma_0 E_0} = \frac{1}{2\sigma_0}\sqrt{\frac{w}{a}\left(\frac{w}{a}+4\right)} \tag{4.5}$$

The asymptotic forms in two limits are given by

$$R_4 \approx \frac{1}{\sigma_0}\sqrt{\frac{w}{a}} \quad , \qquad w/a \ll 1 \tag{4.6}$$

$$R_4 \approx \frac{1}{2\sigma_0}\left(\frac{w}{a}+2\right) \text{ , } w/a \gg 1 . \tag{4.7}$$

4.3.1.2 Empirical approximation and asymptotic solutions in 3d

Before discussing the 3d composite, let us consider the 1d composite that has two perfect linear conductors as in Figure 4.5. The current density between the inclusions are

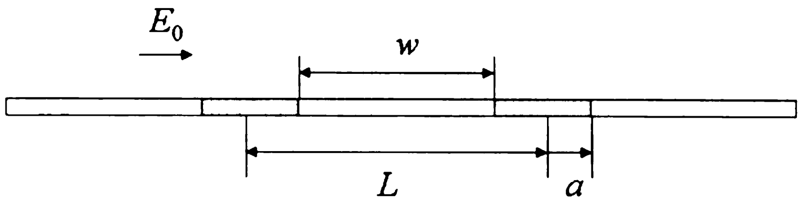

Figure 4.5 One dimensional composite material with two perfect conductor inclusions.

identical for the two resistance measurements (R_4, R_2). Since the voltage ΔV between the inclusions is simply given by $E_0 w$ in the constant electric field, the 4-point resistance R_4 can be represented by

$$R_4 = \frac{\Delta V}{I_0} = \frac{E_0 w}{\sigma_0 E_0} = \frac{w}{\sigma_0} \; . \tag{4.8}$$

Let us move to the 3d composite structure. In 3d, the inclusions are spheres. Thorpe suggested an empirical approximation of the voltage ΔV between the inclusions.[53]

$$\Delta V = E_0 L \left[1 - \left(\frac{2a}{L} \right)^d \right]^{\frac{1}{2^{d-1}}} , \tag{4.9}$$

where d is the dimension. This formula reproduces correctly the exact solutions in 1d and 2d.

$$\Delta V = E_0 [L - 2a] = E_0 w \quad , \quad d = 1 \tag{4.10}$$

$$\Delta V = E_0 \sqrt{L^2 - 4a^2} \quad , \quad d = 2 \tag{4.11}$$

In 3d ($d = 3$), the approximation gives

$$\Delta V = E_0 L^{1/4} (L^3 - 8a^3)^{1/4} \; . \tag{4.12}$$

In addition, the normalized current I_0 defined in Section 4.3.1 is given by $\pi a^2 \sigma_0 E_0$ in 3d because the cross section of the spheres is πa^2. Then, the 4-point resistance R_4 in 3d is obtained by

$$R_4 = \frac{\Delta V}{I_0} = \frac{E_0 L^{1/4} (L^3 - 8a^3)^{1/4}}{\pi a^2 \sigma_0 E_0} = \frac{1}{\pi \sigma_0 a} \left(\frac{w}{a} + 2 \right)^{1/4} \left[\left(\frac{w}{a} + 2 \right)^3 - 8 \right]^{1/4} . \qquad (4.13)$$

Meanwhile, the asymptotic solution of the same composite in 3d was given in the close neck limit ($w/a << 1$).[46] That was done by Choy et al. using the multipole image method. Following this method, the voltage ΔV in that limit is obtained as a logarithmic function.

$$\Delta V \approx \frac{\pi^2 a E_0}{3} \left| \ln\left(\frac{a}{w} \right) + const \right|^{-1} , \qquad w/a << 1 \qquad (4.14)$$

A constant term exists in the formula as the next leading term. Then, the 4-point resistance is represented by

$$R_4 = \frac{\Delta V}{I_0} \approx \frac{\pi}{3 \sigma_0 a} \left| \ln\left(\frac{a}{w} \right) + const \right|^{-1} , \quad w/a << 1. \qquad (4.15)$$

Comparing with this logarithmic form in the limit, the approximation in Eq. (4.6) turns out incorrect; because the asymptotic form of the empirical formula is given by

$$R = \frac{\Delta V}{I_0} \approx \frac{E_0 2a(3w/a)^{1/4}}{\pi a^2 \sigma_0 E_0} = \frac{2.632}{\sigma_0 \pi a} \left(\frac{w}{a} \right)^{1/4} , \qquad w/a << 1. \qquad (4.16)$$

4.3.2 2-point resistance (R_2)

The second configuration for the resistance calculation is much simpler than the 4-point resistance. As presented in Figure 4.6, a voltage difference V_0 is applied across

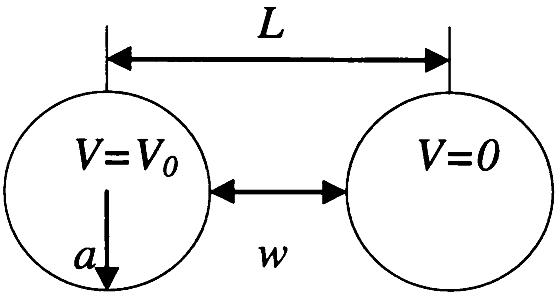

Figure 4.6 2-point resistance measurement of two circular inclusions. A resistance is obtained when the current flows between these two inclusions.

the centers of two inclusions, and then current flows between the inclusions. Most current flows through the neck when the inclusions are close. From this current flow, a resistance is simply given by

$$R_2 = \frac{V_0}{I} , \tag{4.17}$$

where V_0 is the applied voltage and I is total current between the inclusions. This resistance R_2 is called *2-point resistance* because it is equal to the normal resistance measurement.

4.3.2.1 Exact solutions in 2d

Exact solutions of this resistance for this geometry has been derived by the image charge method. Details of this method can be found in the reference.[52] Suppose ε is the electric permeability of the host. Then, the capacitance C between two circular conductors in 2d is given by

$$C = 2\pi\varepsilon\left[\cosh^{-1}\left(\frac{L^2}{2a^2}-1\right)\right]^{-1} = 2\pi\varepsilon\left[\cosh^{-1}\left(\frac{w^2}{2a^2}+\frac{2w}{a}+1\right)\right]^{-1}, \tag{4.18}$$

where $L = w + 2a$. The resistance R between two circles can be represented as the function of the geometry parameters (w, a) by

$$R_2 = \frac{1}{C}\frac{\varepsilon}{\sigma_0} = \frac{1}{2\pi\sigma_0}\cosh^{-1}\left(\frac{w^2}{2a^2}+\frac{2w}{a}+1\right). \tag{4.19}$$

The asymptotic forms of this resistance can be given by

$$R_2 \approx \frac{1}{\pi\sigma_0}\sqrt{\frac{w}{a}}+\dots \quad , \quad w/a \ll 1, \tag{4.20}$$

$$R_2 \approx \frac{1}{\pi\sigma_0}\ln\left(\frac{w}{a}\right)+\dots \quad , \quad w/a \gg 1. \tag{4.21}$$

One of these asymptotic formulas (Eq. (4.20)) can be obtained more simply using the approximation that all currents flow through the neck. It is presented in Appendix A.3.

4.3.2.2 Exact solutions in 1d and 3d

In 1d, the 2-point resistance (R_2) is simply given by

$$R_2 = \frac{w}{\sigma_0}, \tag{4.22}$$

where w is the neck distance. This resistance (R_2) is equal to the 4-point resistance (R_4) in Eq. (4.8).

In 3d, this 2-point resistance can be obtained by the image charge method.[52]

$$R_2 = \frac{1}{C}\frac{\varepsilon}{\sigma_0} = \left[2\pi\sigma_0 a\sinh(\beta)\sum_{n=1}^{\infty}\frac{1}{\sinh(n\beta)}\right]^{-1}, \tag{4.23}$$

where $\cosh(\beta) = \frac{w}{2a} + 1$. The capacitance C between two perfect spherical conductors is

$$\begin{aligned} C &= 2\pi\varepsilon a \sinh(\beta) \sum_{n=1}^{\infty} \left[\frac{1}{\sinh(2n-1)\beta} + \frac{1}{\sinh(2n\beta}) \right] \\ &= 2\pi\varepsilon a \sinh(\beta) \sum_{n=1}^{\infty} \frac{1}{\sinh(n\beta)} = 2\pi\varepsilon a \left\{ 1 + \frac{1}{\sinh(2\beta)} + \frac{1}{\sinh(3\beta)} + \ldots \right\} \end{aligned} \quad . \qquad (4.24)$$

Meanwhile, the exact asymptotic expansion in the limit has been done by Choy.[46] It is obtained by

$$R_2 \approx \frac{1}{\sigma_0 a\pi} \left[\ln\left(\frac{a}{\omega}\right) + const \right]^{-1}, \quad w/a \ll 1. \qquad (4.25)$$

4.3.3 The ratio of R_4 and R_2

The ratio of the 4-point resistance and 2-point resistance can be given by the exact form in 2d and asymptotic form in 3d. In 1d, two resistances turned out identical from Eq. (4.8) and Eq. (4.22). So, the ratio in 1d is 1.

In 2d, two resistances were given by the exact forms. It should be noted that the two resistances (see Eq. (4.6) and Eq. (4.20)) have the identical forms of square root in the limit of $w/a \ll 1$. The only difference is the pre-factor that is a constant π. So, the ratio is obtained by

$$\frac{R_4}{R_2} = \pi \ , \quad w/a \ll 1. \qquad (4.26)$$

In 3d, due to the infinite sums in Eq. (4.20), the asymptotic behavior cannot be determined in the close neck limit ($w/a \ll 1$) in this analytic solution. However, if we consider only the leading terms of logarithmic form in Eq. (4.15) and Eq. (4.22), the ratio of the resistances (R_4 and R_2) can be given by

$$\frac{R_4}{R_2} \approx \frac{\pi^2}{3} \approx 3.29 \ . \tag{4.27}$$

4.4 Computer Simulation

4.4.1 FEM analysis for 2d composite

To calculate the resistances defined in the previous section for a composite, numerical simulations were performed using the FEM. Modeling to obtain the meshed geometry was done by ANSYS, and the FEM analysis of electrical conduction problem was performed by ABAQUS. Details about these procedures can be found in Chapter 2. In this problem, the geometry itself is not complicated like the diamond crystal. It consists of a large square host and two circular inclusions. Therefore, the modeling was somewhat a simple procedure. However, I had some troubles in the meshing while computer models were generated over a wide range of the neck distances. In the close neck limit, the finite elements near the neck region should have been extremely small. Usually, the meshing in this limit has been restricted due to the limitation of the computer memory. To generate a constant electric field, two large pads were attached to the boundaries of the host and these pads were modeled to be perfect conductors in the analysis.

I made a large square host material ($L_x = 1.0$, $L_y = 1.0$) that included two circular perfect conductors ($a = 0.05$). In addition, two large pads (*P*) were attached on the

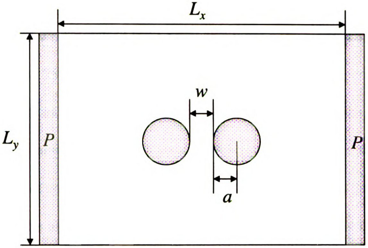

Figure 4.7 The geometry of 2d composite material with circular inclusions. Huge plates were attached to the host to form a constant electric field in 4-point resistance measurement. Those plates were removed for 2-point resistance measurement.

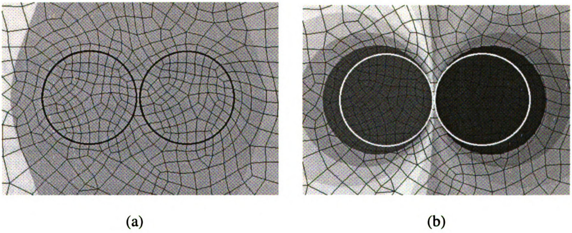

Figure 4.8 Contour graphs of voltage distribution near the neck in 2d. (a) is given from 4-point measurement and (b) is given from 2-point measurement.

boundaries to form a constant field inside the host for the 4-point resistance calculation. However, these pads were not used for 2-point resistance calculations. The geometry was meshed by more than 2500 square elements that have four nodes on the corners. Normally, there were more than 2500 nodes in the meshed models. Many computer models over a wide range of the neck distances were generated. In the analysis of the 4-point resistances, unit conductivity was given to the host material and high conductivity (10^6) was given to the inclusions and pads. The resistance was calculated as a function of neck distance. Two figures in Figure 4.8 represent the voltage distributions inside the sample. Figure 4.8(a) denotes for a 4-point resistance calculation when a voltage is applied on the host boundary and Figure 4.8(b) shows a 2-point resistance when the voltage is applied on the centers of the inclusions. In the 2-point resistance calculation, it should be noted that the current distribution is concentrated near the neck region.

4.4.2 FEM analysis for 3d composite

A numerical simulation using FEM has been done for 3d composite. A large brick was constructed as the host material ($L_x = 1.0$, $L_y = L_z = 0.6$) and two spheres ($a = 0.05$) were used for two spherical inclusions (see Figure 4.9). After meshing this geometry using tetrahedral elements, the FEM analysis was performed over a wide range of the neck distances. Figure 4.10(a) and (b) show the generated meshes and the equipotential distributions for two resistance calculations (R_4 and R_2).

The computer models were meshed by tetrahedral elements that had four nodes and four facets. Normally, much finer meshings (~1500 nodes, ~7000 elements) than the

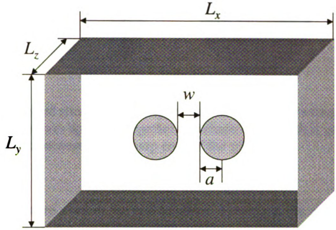

Figure 4.9 Three-dimensional composite material with two spherical inclusions. Similar large bricks were attached to the host for 4-point measurement.

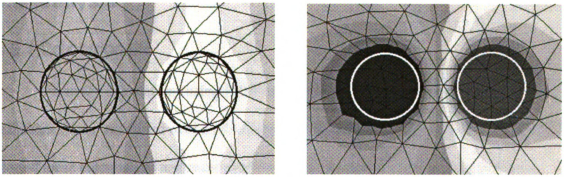

(a) (b)

Figure 4.10 Contour graph of voltage distribution near the neck in 3d. (a) is given from 4-point measurement and (b) is given from 2-point measurement.

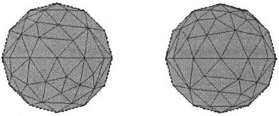

Figure 4.11 The meshed structure of the spherical inclusions. For a rough meshing, as these spheres approach together, the shape of the neck is getting less realistic because of the sharp ends of the spheres.

meshing in the figure were used in the real analysis. However, the generation of realistic shapes of the sphere was seriously limited by the computer memory problem. The spherical inclusions were modeled as polygons as shown in Figure 4.11. These rough meshings could generate significant numerical errors in the simulation, especially in the close neck limit ($w/a << 1$).

4.5 Analysis

4.5.1 2d composite

From the calculations using FEM code (ABAQUS), 4-point and 2-point resistances were examined over a wide range of the neck distances ($0.01 < w/a < 10.0$). I plotted these calculations and compared them with the analytic solutions as in Figure 4.12. Cross (+) in the graph represents the 4-point resistance calculation obtained from FEM analysis and the solid line indicates the exact solution given by Djodjevic et al. as shown in Eq. (4.5). Square (□) denotes the FEM result of 2-point resistance and the solid line means the analytical solution obtained by the image charge method. The results

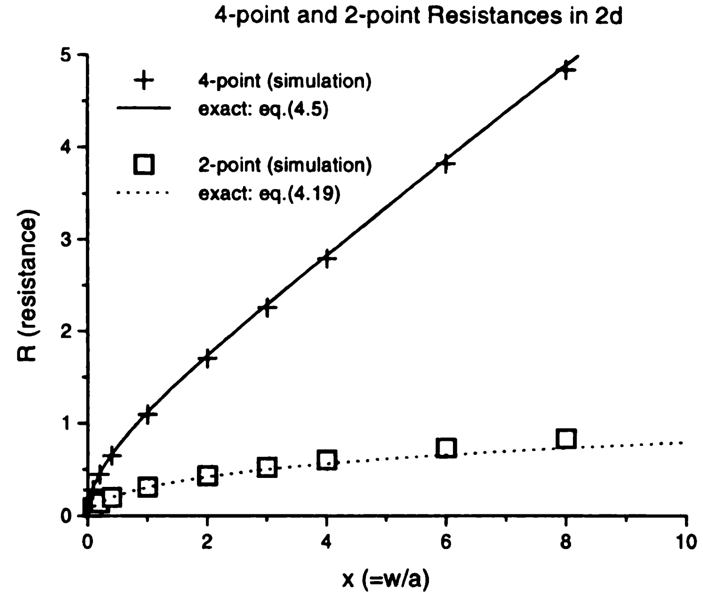

(a)

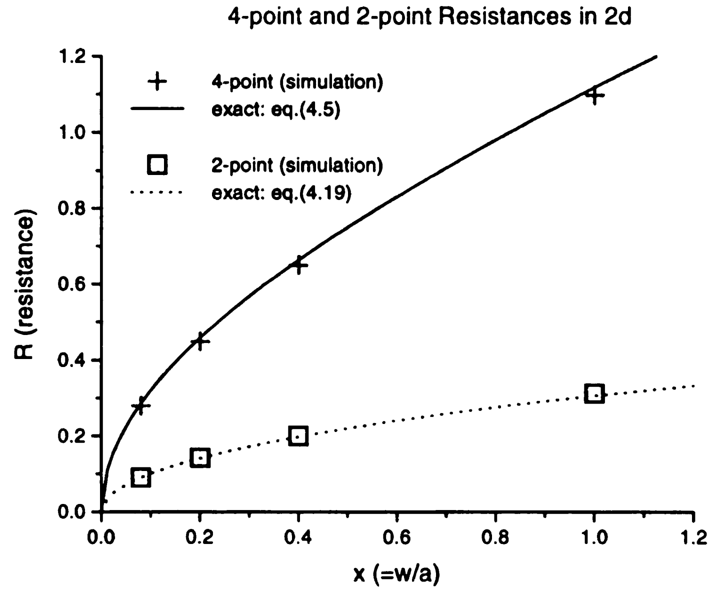

(b)

Figure 4.12 Numerical solutions of the 4-point and 2-point resistances were obtained for 2d composite using FEM analysis. They agree well in all regions with the analytical solutions. (b) shows the detail in the close neck limit.

from the simulation show good agreement with the analytical solutions. However, the simulated 2-point resistances in the far field limit were observed to be slightly higher than the analytical solutions. That is the finite size effect of the host, i.e. the inclusions were getting close to the boundaries of the host as the neck distances increase. In Figure 4.12(b), more details in the close neck limit were shown to verify the asymptotic behaviors. Even using the rough meshes, the numerical calculation could reproduce the square root law in 4-point and logarithmic law in 2-point resistances in that limit.

4.5.2 3d composite

Figure 4.13 presents the numerical result and analytical solutions in 3d. The cross represents the 4-point resistance (R_4) from the simulation and the solid line denotes the empirical formula that is suggested by Thorpe. Choy's solution in the close neck region is shown by the dashed line. This asymptotic line is drawn by selecting a constant for the best fit with the numerical result in the region. The empirical formula agrees well with the numerical results in most part in the figure. However, serious disagreements were detected in the close neck limit as shown in Figure 4.13(b). In the limit, the numerical simulation, the empirical formula, and the Choy's asymptotic solution do not agree very well. The numerical error should be from the rough meshing in that region.

The square mark shows the simulated 2-point resistance (R_2) and the solid line is the analytic solution given by the infinite series sum. The dashed line denotes the another asymptotic formula in the other limit ($w/a \ll 1$) given by Choy. The simulated results were obtained slightly lower than the analytic solution. The rough meshing raised errors again for the 2-point resistances in the close neck limit. Substantial discrepancy between

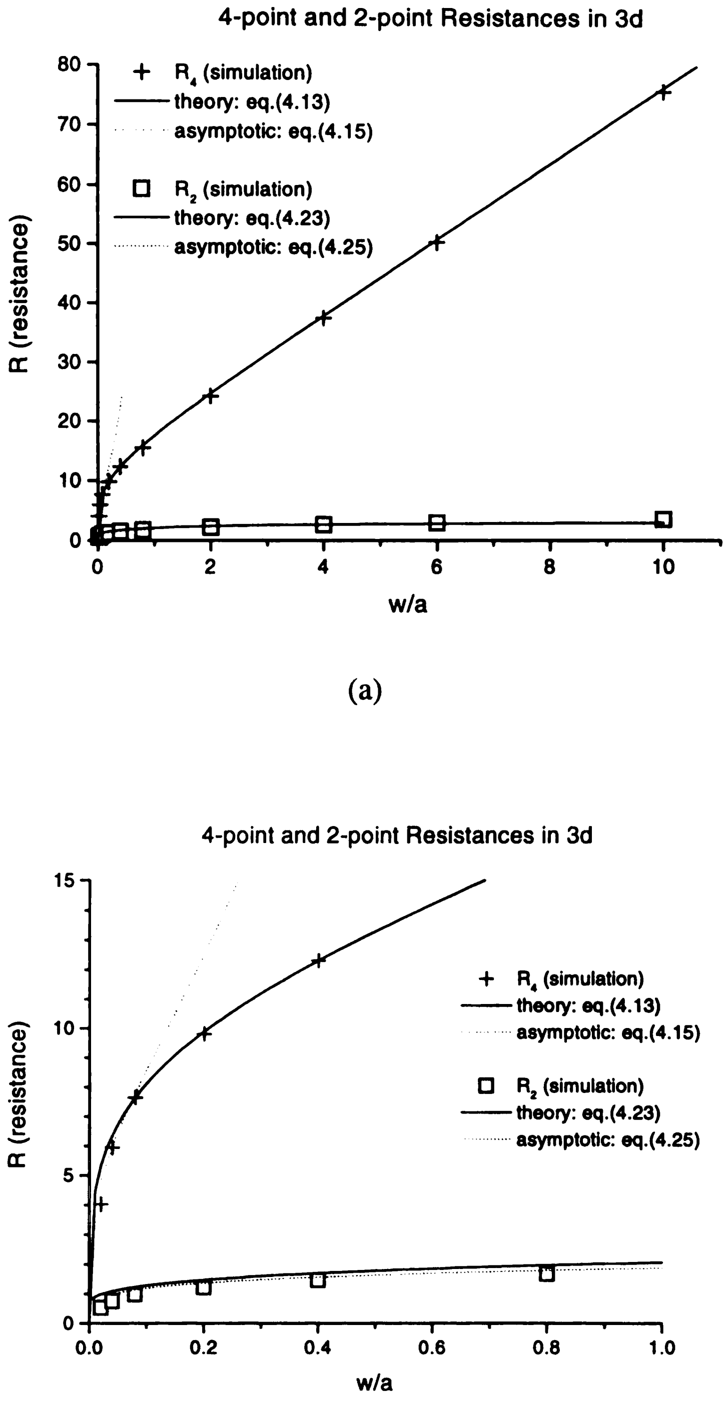

(a)

(b)

Figure 4.13 Numerical solutions of the 4-point and 2-point resistances were obtained for 3d composite using FEM analysis. They agree nicely in most regions with the analytical solutions, but show some disagreements in an asymptotic regime (close limit). (b) shows the detail in that limit.

the numerical result and the exact solution has been detected in that limit

4.5.3 The ratio of 4-point and 2-point resistances

The ratio of two resistances (4-point and 2-point) has been one of the major concerns in this study. The analytic prediction and the numerical result are presented in Figure 4.14. The ratio can be determined analytically in 2d since all exact forms of the resistances are obtained. As expected from the analytical solutions, that ratio approaches π in the close neck limit ($w/a << 1$). The numerical simulation is observed to approach this constant in that limit. The prediction of this ratio in 3d was given by $\pi^2/3$ from the asymptotic forms done by Choy. However, from the numerical simulation, the ratio turns out to approach ~8.0. A large error occurred here mainly because the numerical error caused by the rough meshings. However, the analytic prediction also has error because the constant terms as the second leading terms in the formula have been neglected in the derivation of this ratio. It should be tested more carefully with better meshings. This study could be a subject for the future research.

4.6 Conclusion

In this chapter, I have described two main subjects. One was the demonstration of the numerical analysis using the FEM for the study of composite materials and the other was the investigation of the ratio of two resistance calculations (4-point and 2-point). Both studies were done for a simple composite model that was composed of a large host and two spherical inclusions of perfect conductors. Two resistance measurements (4-

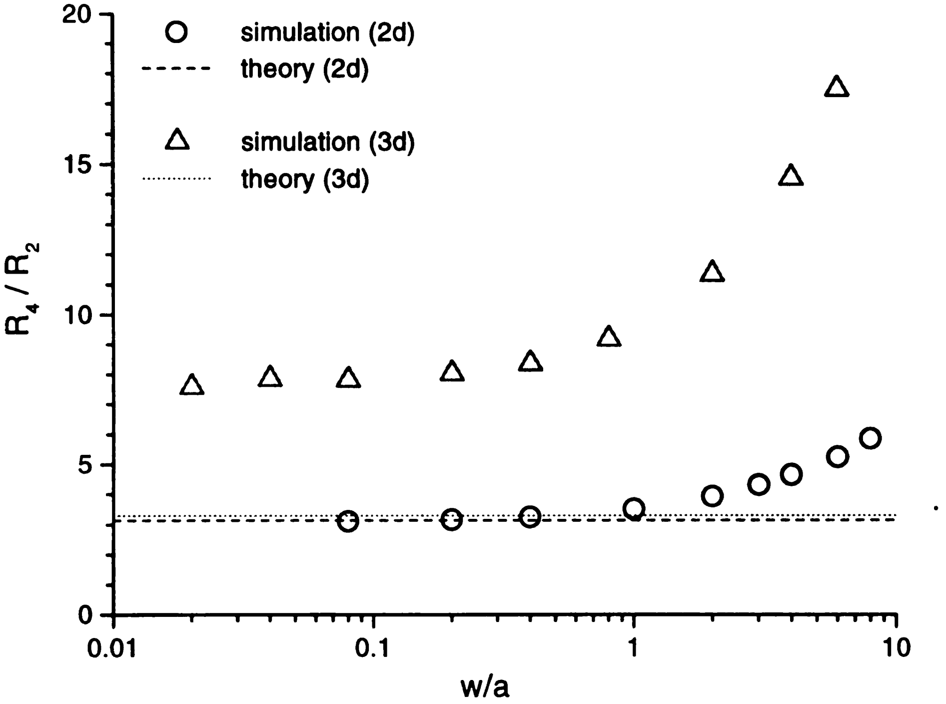

Figure 4.14 The ratio between 4-point resistance and 2-point resistance in 2d and 3d. Each ratio was observed to approach a constant in the close neck limit ($w/a \ll 1$). The limiting value is given by π in 2d and $\pi^2/3$ in 3d.

point, 2-point) were defined in the geometry depending on whether the voltage is applied to the boundary of the host or the inclusions. For the first subject, I presented the simulated results of these two resistances using the FEM analysis and they were compared with the analytic solutions. Since the numerical results were observed to be consistent with the analytic predictions, the FEM could be suggested as a primary step to investigate the effective medium theory of complex composite materials. For the second subject, I compared two resistances over a wide range of the neck distances. A simple relation between these two quantities was found analytically in 2d and numerically in 3d in the close neck limit ($w/a << 1$). However, the numerical result should be tested with better meshings. I suggest that this simple relation may provide an useful approach to the study of composite material properties.

APPENDICES

A.1 Reciprocity theorem

This electric reciprocity theorem has been stated in many works since the earliest work was done by Lord Rayleigh in last century.[54] Since then, many publications related to this topic came out because of theoretical and practical interests.[55,56,57] This relation is quite general; it works for all materials with any shapes in any dimensions. It does not depend on whether the sample is homogeneous, isotropic or not. The sample can be a composite material that has various shapes of inclusions of different conductivity, even some holes in it. The only condition of this theorem is that the sample should be Ohmic. First, this theorem was concerned with electric field. However, since the role of magnetic field in a conductivity tensor was understood by the Onsager relation,[58, 59] this reciprocity theorem has been concerned with the interference term in the conductivity tensor by magnetic field, too. This leads to the reverse-magnetic-field reciprocity (RMFR) under the assumption of the linearity of a sample.[21] These reciprocity relations have important implications for electronic-transport properties in electric current and magnetic field (Hall effect, magnetoresistance).

In this appendix, I simply derive this theorem for zero magnetic field under the assumption that a bulk conductor can be represented by an equivalent resistor circuit. Suppose a sample in arbitrary shape is electrically equivalent to a circuit of resistors as in Figure A.1. All of the resistors are fully connected to each other. In this proof, the sample and the resistors in the circuit are assumed electrically Ohmic, which means that it does not show any diode behavior. This is the only requirement of the theorem. Thus, this

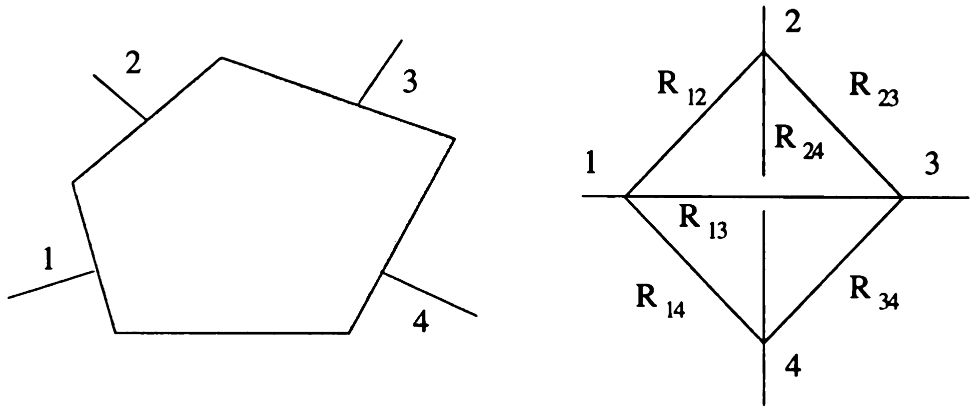

Figure A.1 A sample with four probes and its equivalent circuit. The electric circuit is composed of many resistors that are fully connected.

theorem does not work for non-Ohmic sample. The laws of Kirchhoff in an electrical circuit can be used to prove it.

Suppose we have a sample with n leads on it for the conduction, then there are r ($={}^nC_2$) resistors in the circuit. First, we need to know the number of independent current loops in this circuit to find out how many linear equations we need. The maximum number of currents is r, which is same with the number of resistors. And there are $n-1$ constraints of currents by current conservation on each lead, known as the first law of Kirchhoff. Although there are n vertices for constraints, the two constraints on vertices that the external current flows in and out are really a single constraint. Then we have d independent current loops for n leads as

$$d = r - (n-1) = r - n + 1\,, \tag{A.1}$$

where r ($={}^nC_2$) is a number of resistors and n is a number of vertices. Because there are r unknown currents, i_1, i_2, ... , i_r on each resistor, we have $n-1$ constraints for currents at each vertex by Kirchhoff's first law of current conservation. Although there are n vertices for constraints, the two constraints on vertices that the external current flows in and out are really a single constraint. Since r is equal to $n(n-1)/2$, the number of independent loops in the circuit is given by

$$d = \frac{n(n-1)}{2} - (n-1) = \frac{(n-1)(n-2)}{2} \tag{A.2}$$

which is one for 3 leads, three for 4 leads, six for 5 leads and so on. We also have one more loop by the external current i_0 as well as d loops in the sample. We need to set up $d+1$ current loops for Kirchhoff laws which give $d+1$ current equations. There is one condition in setting up these loops that each resistor should be included in at least one current loop. To prove the reciprocity theorem, a resistor R_{pq} is selected for external current flow and R_{mn} for voltage measurement. A voltage V is applied across R_{pq} and the current i_0 flows in. Suppose R_{mn} is shared by m current loops ($i_{j+1}, .., i_{j+m}$) and R_{pq} is shared by p current loops ($i_{k+1}, \dots, i_{k+p}$) and the external current i_0. Now we have $d+1$ linear equations from Kirchoff laws

$$\begin{pmatrix} R_{pq} & 0 & \cdot & 0 & 0 & \cdot & -R_{pq} & -R_{pq} & \cdot & 0 \\ 0 & M_{1,1} & \cdot & \cdot & \cdot & \cdot & \cdot & \cdot & \cdot & \cdot \\ \cdot & \cdot & \cdot & \cdot & \cdot & \cdot & \cdot & \cdot & \cdot & \cdot \\ 0 & \cdot & \cdot & M_{j+1,j+1} & \cdot & \cdot & \cdot & \cdot & \cdot & \cdot \\ 0 & \cdot & \cdot & \cdot & M_{j+m,j+m} & \cdot & M_{j+m,k+1} & \cdot & \cdot & \cdot \\ \cdot & \cdot & \cdot & \cdot & \cdot & \cdot & \cdot & \cdot & \cdot & \cdot \\ -R_{pq} & \cdot & \cdot & \cdot & M_{k+1,j+m} & \cdot & M_{k+1,k+1} & \cdot & \cdot & \cdot \\ -R_{pq} & \cdot & \cdot & \cdot & \cdot & \cdot & \cdot & M_{k+p,k+p} & \cdot & \cdot \\ \cdot & \cdot & \cdot & \cdot & \cdot & \cdot & \cdot & \cdot & \cdot & \cdot \\ 0 & \cdot & \cdot & \cdot & \cdot & \cdot & \cdot & \cdot & \cdot & M_{d,d} \end{pmatrix} \begin{pmatrix} i_0 \\ i_1 \\ \cdot \\ i_{j+1} \\ i_{j+m} \\ \cdot \\ i_{k+1} \\ i_{k+p} \\ \cdot \\ i_d \end{pmatrix} = \begin{pmatrix} V \\ 0 \\ \cdot \\ 0 \\ 0 \\ \cdot \\ 0 \\ 0 \\ \cdot \\ 0 \end{pmatrix} \tag{A.3}$$

where $M_{0,0}$ is R_{pq} and p terms ($M_{0,k+1}, .., M_{0,k+p}$) in *0-th* column are $-R_{pq}$. In Eq. (A.3), $M_{i,j}$ is a matrix element that represents a sum of resistors where the current i_j

flows in the *i-th* loop. It is equal to $M_{j,i}$ because those two terms represent the same resistors that are shared by the *i-th* and *j-th* current loops. A solution for i_j from Eq. (A.3) is given by

$$i_j = V\frac{\Delta_{0,j}}{\Delta} \tag{A.4}$$

where Δ denotes the determinant of the matrix and $\Delta_{i,j}$ is a cofactor of $M_{i,j}$. Since the net current flow $\sum_{a=1}^{m} i_{j+a}$ in R_{mn} is given by the sum of all currents of loops pass through it, a resistance defined by a voltage across *m*, *n* and a current through *p*, *q* is given by

$$R_{pq}^{mn} = \frac{V_{mn}}{i_0} = \frac{R_{mn}\sum_{a=1}^{m} i_{j+a}}{V\frac{\Delta_{0,0}}{\Delta}} = \frac{R_{mn}\sum_{a=1}^{m}\Delta_{0,j+a}}{\Delta_{0,0}}, \tag{A.5}$$

In this equation, $\Delta_{0,j+a}$ is equal to $-R_{pq}\sum_{b=1}^{p}\Delta_{(0,k+b),(0,j+a)}$ because there are *p* terms of $-R_{pq}$ in the *0*-th column and the other terms are zero except *0*-th element R_{pq} irrelevant in calculating $\Delta_{0,j+a}$. [$\Delta_{(0,k),(0,j)}$ is the determinant of the matrix without the *0*-th and *k*-th rows and the *0*-th and *j*-th columns.] From this relation, we have

$$R_{pq}^{mn} = -\frac{R_{mn}R_{pq}\sum_{a=1}^{m}\sum_{b=1}^{p}\Delta_{(0,k+b),(0,j+a)}}{\Delta_{0,0}}. \tag{A.6}$$

By switching the leads *p, q* and *m, n* [which is equivalent to exchanging $k+b$, $j+a$ in this notation], we have another resistance R_{mn}^{pq} defined by a voltage *V* applied across R_{mn}

instead of R_{pq} and a voltage measured across R_{pq}. Since $\Delta_{(0,k+b),(0,j+a)}$ is equal to $\Delta_{(0,j+a),(0,k+b)}$ due to the symmetry of the matrix, we have a symmetric relation by

$$R_{mn}^{pq} = -\frac{R_{pq}R_{mn}\sum_{a=1}^{m}\sum_{b=1}^{p}\Delta_{(0,j+a),(0,k+b)}}{\Delta_{0,0}} = R_{pq}^{mn} \tag{A.7}$$

This *reciprocity theorem* says that the resistance from a voltage across *p*, *q* and current through *m*, *n* is equal to another resistance from voltage across *m*, *n* and current through *p*, *q* in an equivalent resistor electrical circuit, and therefore in the sample.

A.2 Counting of Independent *4-terminal* terms

In this part, I describe how to count the number of 4-terminal independent terms in a resistance table. I have shown that there are ${}^{n}C_2$ $(= n(n-1)/2)$ independent terms in a resistance table for an n-probe measurement in Section 2.2.2. Four probes are enough to determine the isotropic conductivity because the four probes generate two independent 4-terminal terms. However, the unknown parameters are increased in an anisotropic conductivity tensor. Thus, we need more independent terms in a resistance table. To have more independent terms in a table, we need to have more probes on the sample. How many probes are needed for an anisotropic conductivity tensor? In Table A.1, the first column shows the number of terminals and the second column is the number of unknowns when the contacts are Ohmic. The third column is the number of independent terms in a resistance table as proved in Section 2.2.2. The fourth column is the number of contact resistances that is equal to the number of leads.

Table A.1 A table represents the number of independent 4-terminal terms in a resistance matrix for n-probe measurement.

Number of Terminal	Unknowns (ρ_{ij}, contact resistances)	Independent Elements (A)	Contact resistances (B)	Independent 4-terminal terms ($A-B$)
2	8	1	2	0
3	9	3	3	0
4	10	6	4	2
5	11	10	5	5
6	12	15	6	9
7	13	21	7	14
8	14	28	8	20
:	:	:	:	:
n	$6+n$	${}^{n}C_2$ $(=n(n-1)/2)$	n	$n(n-3)/2$

The number of independent 4-terminal terms in the last column can be given by following argument. There are A independent terms in a resistance table. Meanwhile, the contact resistances are independent of the sample resistances. They are independent each other, too. So, if we subtract the contact resistances (B) from the whole independent terms (A), the rest (A-B) should be independent of the contact resistances. Therefore, we have A-B independent 4-terminal terms. Following this argument, we need 6 probes on a sample to determine 6 components in an anisotropic tensor, because six probes generate 9 independent 4-terminal terms.

A.3 Resistances of Two Perfect Hyperspherical Conductors

Consider two hyperspheres in the plane with radius a and separated by L so that the neck distance is w (see Figure A.2). If x is the distance up the vertical line from the center, then we have

$$x = (a + \frac{w}{2})\sin\theta = (1 + \frac{w}{2a})a\sin\theta = (1+\chi)a\sin\theta \ , \quad \chi = \frac{w}{2a} \ . \tag{A.8}$$

The two spheres have a resistance between them that is mainly given by the neck region. If we strip the neck into long this differential sections and add up the resistances in parallel, we find the total resistance R as [where $w = L - 2a$].

$$R^{-1} = \sigma_0 \int_0^{x_{\max}} \frac{\gamma_{d-1} x^{d-2} dx}{w + 2a(1-\cos\theta)} \tag{A.9}$$

where γ_d factor for the area in d dimensions, that might be 2 in 1d and 2π in 2d and 4π

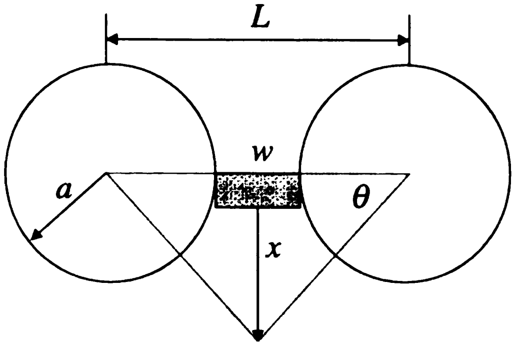

Figure A.2 Two circular perfect conductors in a host material in the close neck limit.

in 3d etc. More generally $\gamma_d = 2\pi^{\frac{d}{2}} / \Gamma\left(\frac{d}{2}\right)$. If we look at small θ, we may write $\theta \approx x / a$, so that the integral becomes

$$R^{-1} = \sigma_0 \int_0^{x_{\max}} \frac{\gamma_{d-1} x^{d-2} dx}{w + x^2 / a} \tag{A.10}$$

if we make a change of variable to y, where $x = \sqrt{awy}$, the integral can be rewritten as which can be evaluated to give

$$R^{-1} = \sigma_0 a \gamma_{d-1} (\omega a)^{\frac{d-3}{2}} \int_0^{\infty} \frac{y^{d-2} dy}{1 + y^2} \tag{A.11}$$

where we have replaced the upper limit in the integral with infinity for narrow necks. This integral converges at the lower end if $d > 1$ and at the upper end if $d < 3$, so that in general for $1 < d < 3$, we have the result

$$R^{-1} = \sigma_0 \frac{a\pi\Gamma\left(\frac{3-d}{2}\right)}{(wa\pi)^{\frac{3-d}{2}}}. \tag{A.12}$$

This gives a result in two dimensions as

$$R^{-1} = \sigma_0 \pi \sqrt{a / w} \tag{A.13}$$

Note that as d approaches one from above, $R^{-1} = \sigma_0 / \omega$ as expected, and as d approaches three form below, we have a divergence. If we use the closed form in 2d,

$$R^{-1} = \sigma_0 \int_0^{x_{\max}} \frac{\gamma_1 dx}{w + 2a(1 - \cos\theta)} = \sigma_0 \int_0^{\theta_{\max}} \frac{\cos\theta d\theta}{(1+\chi) - \cos\theta} \tag{A.14}$$

Then we have

$$\begin{aligned} R^{-1} &= \sigma_0 (1+\chi) \left[-\theta + \frac{2(1+\chi)}{\sqrt{(1+\chi)^2 - 1}} \arctan\left\{ \frac{\sqrt{(1+\chi)^2 - 1}}{\chi} \cdot \tan\frac{\theta}{2} \right\} \right]_0^{\theta_{\max}} \\ &= \sigma_0 (1+\chi) \left[-\theta_{\max} + \frac{2(1+\chi)}{\sqrt{(1+\chi)^2 - 1}} \arctan\left\{ \frac{\sqrt{(1+\chi)^2 - 1}}{\chi} \cdot \tan\frac{\theta_{\max}}{2} \right\} \right] \end{aligned} \tag{A.15}$$

In the limit $\chi = w / 2a << 1$, we have the same result with Eq. (A.13).

$$R^{-1} \approx \sigma_0 \left[-\theta_{\max} + \frac{2}{\sqrt{2\chi}} \arctan\left\{ \frac{\sqrt{2}}{\sqrt{\chi}} \cdot \tan\frac{\theta_{\max}}{2} \right\} \right] \approx \sigma_0 \frac{\pi}{\sqrt{2\chi}} = \sigma_0 \pi \sqrt{\frac{a}{w}} \tag{A.16}$$

A more close examination of the integral when d=3, shows that if we use $x_{\max} = a$ for the upper limit, which seems reasonable, we can do the integral in Eq. (A.9) in closed form, to give

$$\begin{aligned} R^{-1} &= \sigma_0 \int_0^{x_{\max}} \frac{\gamma_2 x dx}{w + 2a(1 - \cos\theta)} = \frac{\pi \sigma_0}{a} \int_0^{x_{\max}} \frac{x dx}{(1+\chi) - \cos\theta} \\ &= \pi \sigma_0 (1+\chi)^2 a \int_0^{\theta_{\max}} \frac{\cos\theta \sin\theta d\theta}{(1+\chi) - \cos\theta} \end{aligned} \tag{A.17}$$

Let $y = \cos\theta$, then

$$\begin{aligned}
R^{-1} &= -\pi\sigma_0(1+\chi)^2 a\int_1^{y_{\max}} \frac{y\,dy}{(1+\chi)-y} \\
&= -\pi\sigma_0(1+\chi)^2 a\left[-y-(1+\chi)\ln\{(1+\chi)-y\}\right]_1^{y_{\max}} \\
&= \pi\sigma_0(1+\chi)^2 a\left[(y_{\max}-1)+(1+\chi)\ln\left\{\frac{(1+\chi)-y_{\max}}{\chi}\right\}\right] \\
&\approx \pi\sigma_0 a\left[(y_{\max}-1)+\ln\left\{\frac{1-y_{\max}}{\chi}\right\}\right]
\end{aligned} \tag{A.18}$$

If we take $y_{\max} = 0$ $(\theta = \frac{\pi}{2})$, then

$$\begin{aligned}
R^{-1} &\approx \pi\sigma_0 a\left[\ln\left\{\frac{1}{\chi}\right\}-1\right] = \pi\sigma_0 a\left[\ln\left\{\frac{2a}{w}\right\}-1\right] = \pi\sigma_0 a\left[\ln\left\{\frac{a}{w}\right\}+\ln\{2\}-1\right] \\
&= \pi\sigma_0 a\left[\ln\left\{\frac{a}{w}\right\}-0.3069\right]
\end{aligned} \tag{A.19}$$

And if $y_{\max} = \frac{1}{\sqrt{2}} = 0.7071$ $(\theta = \frac{\pi}{4}$, $x_{\max} = a)$, then

$$\begin{aligned}
R^{-1} &\approx \pi\sigma_0 a\left[-0.2929+\ln\left\{\frac{0.2929}{\chi}\right\}\right] = \pi\sigma_0 a\left[\ln\left\{\frac{a}{w}\right\}+\ln 2+\ln 0.2929-0.2929\right] \\
&= \pi\sigma_0 a\left[\ln\left\{\frac{a}{w}\right\}-0.8277\right]
\end{aligned} \tag{A.20}$$

The exact asymptotic expansion done by Choy gives

$$R^{-1} \approx \sigma_0 a\pi\left[\ln\left(\frac{a}{\omega}\right)-\frac{8}{3}\right] \approx \sigma_0 a\pi\left[\ln\left(\frac{a}{\omega}\right)-2.667\right]. \tag{A.21}$$

Thus we get the leading term right in both 2d and 3d, but the next term is wrong.

BIBLIOGRAPHY

BIBLIOGRAPHY

---

[1] The term *resistivity* is also used sometimes in this dissertation.

[2] This sample was prepared by M. Schnars and B. Golding.

[3] S. M. Sze, *Physics of Semiconductor Devices* (John Wiley & Sons, Inc., New York, 1981), pp.848-851.

[4] R. J. Gillespie et al., *Chemistry* (Allyn and Bacon, Inc., Newton, MA, 1986), p.803.

[5] J. R. Olson, R. O. Pohl, J. W. Vandersande, A. Zoltan, T. R. Anthony, and W. F. Banholzer, Phys. Rev. B **47**, 14850 (1993).

[6] C. H. Seager and T. G. Castner, J. Appl. Phys. **49**, 3879 (1978)

[7] J. Werner, "Electronic Properties of Grain Boundaries," in *Polycrystalline Semiconductors : Physical Properties and Applications*, ed. By G. Harbeke, (Springer-Verlag, Heidelberg, 1985), pp.76-94.

[8] L. J. van der Pauw, Phillips Techn. Rdsch. **20**, 230 (1958).

[9] L. V. Bewley, *Two-dimensional fields in electrical engineering* (The MacMillan Co., New York, 1948).

[10] Y. Sun, O. Ehrmann, J. Wolf, and H. Reuchl, Rev. Sci. Instrum. **63**, 3752 (1992).

[11] Any boundary value problem can be classified into *well-posed* or *ill-posed* problem. Following is a definition of those problems by Hadamard.[11]
Well-posed problem :
(a) There exists a (globally-defined) solution for all (reasonable) data.
(b) The solution is unique.
(c) The solution depends continuously on given data (stability).
Ill-posed problem :
All problems do not satisfy these conditions of well-posed problems.

[12] A. N. Tikhonov and V. Y. Arsenin, *Solutions of Ill-Posed Problems* (Wiley, New York, 1977).

[13] S. Kubo, in *Inverse problems in engineering mechanics*, edited by M. Tanaka and H. D. Bui (Springer-Verlag, Heidelberg, 1993), p.51.

[14] A. R. Day developed an algorithm for this using the conjugate gradient method.

---

[15] L. Collatz, *The numerical Treatment of Differential Equations* (Spring-Verlag, New York, 1966).

[16] S. H. Crandall, *Engineering Analysis* (McGraw-Hill, New York, 1956).

[17] K. J. Bathe and E. L. Wilson, *Numerical Methods in Finite Element Analysis* (Prentice-Hall, Inc., Englewood Cliffs, NJ, 1976))

[18] G. Strang and G. Fix, *An Analysis of the Finite Element Method* (Prentice-Hall, Inc., Englewood Cliffs, NJ, 1973).

[19] D. S. Burnett, *Finite Element Analysis : From Concepts to Application* (Addison-Wesley, Reading, MA, 1987).

[20] B. I. Bleaney and B. Bleaney, *Electricity and Magnetism* (Oxford University Press, Oxford, 1957), p.69

[21] H. H. Sample, W. J. Bruno, S. B. Sample, and E. K. Sichel, J. Appl. Phys. **61,** 1079 (1987).

[22] C. Young et al., *Ray Tracing Creations* (Waite Group Press, Corte Madera, 1994), p.3.

[23] W. H. Press, S. A. Teukolsky, W. T. Vetterling, and B. P. Flannery, *Numerical Recipes* (Cambridge University Press, New York, 1992), p.653.

[24] ANSYS is a registered trademark of SAS IP, Inc..

[25] ABAQUS is the product of Hibbitt, Karlsson and Sorensen, Inc.. For more information, see ABAQUS User's Manual HKS, Inc..

[26] For the labeling scheme chosen, the contact resistances r_1' and r_4 do not appear in Table 2.5. A labeling scheme that involves the cyclic permutations of the four indices (i.e. which replaces I_{14} with I_{41}) would be more useful. The resistance table would contain all 8 contact resistances that could then be determined from a single set of measurements.

[27] M. D. Jaeger, S. Hyun, A. R. Day, M. F. Thorpe, and B. Golding, Diamond and Related Materials 6, 325–328 (1997).

[28] B. I. Shklovskii and A. L. Efros, Electronic Properties of Doped Semiconductors, (Spring-Verlag, Berlin, 1984), Chap.4.

[29] M. D. Jaeger, Ph. D. Thesis, Michigan State University, 1997.

---

[30] C. Kittel, *Introduction to Solid State Physics*, 6th ed. (John Wiley & Sons, Inc., New York, 1986), p.19.

[31] N. W. Ashcroft and N. D. Mermin, *Solid State Physics* (Pergamon Press, Inc., New York, 1962).

[32] W. P. Mason, *Crystal Physics of Interaction Processes* (Academic Press, New York, 1966), p.216.

[33] L. D. Landau and E. M. Lifshitz, *Electrodynamics of Continuous Media* (Pergamon Press, New York, 1960), p.93.

[34] H. R. Schwarz, *Numerical Analysis* (John Wiley & Sons, New York, 1989), p.320.

[35] Z. Xiong and A. Kirsch, J. of Comp. and Appl. Math., **42,** 109 (1992).

[36] G. Arfken, *Mathematical Methods for Physicists*, 3rd ed. (Academic Press, Orlando, 1985), p.510.

[37] This sample was prepared by M. Schnars and B. Golding.

[38] J. C. Maxwell, *Electricity and Magnetism* (Clarendon Press, Oxford, 1873).

[39] A. Einstein, Ann. Phys. **19** 289 (1906).

[40] A. Einstein, Ann. Phys. **34** 591 (1911).

[41] M. F. Thorpe, Proc. R. Soc. London Ser. A **437**, 215 (1992).

[42] J. H. Hetherington and M. F. Thorpe, Proc. R. Soc. London Ser. A **438,** 591 (1992).

[43] D. J. Jeffrey, Proc. R. Soc. London A **335**, 355 (1973).

[44] K. J. Binns and P. J. Lawrenson, *Electric and Magnetic Field Problems* (Pergamon, Oxford, 1973), pp.48-53.

[45] B. R. Djordjevic, J. H. Hetherington, and M. F. Thorpe, Phys. Rev. B **53**, 14862 (1996).

[46] T. C. Choy, A. Alexopulos, and M. F. Thorpe, Phil. Trans. R. Soc. Lond. A (1996).

[47] J. Chen, M. F. Thorpe, and L. C. Davis, J. Appl. Phys. **77**(9) 4349 (1995).

---

[48] A. R. Day, K. A. Snyder, E. J. Garboczi, and M. F. Thorpe, J. Mech. Phys. Solids, **40** 1031-1051 (1992).

[49] A. Cherkaev, K. Lurie, and G. W. Milton, Proc. R. Soc. London A **438**, 519-529 (1992).

[50] L. C. Davis, K. C. Hass, J. Chen, and M. F. Thorpe, Proceedings of the Conference on Composite Materials held in Virginia, June 1993.

[51] M. F. Thorpe and I. Jasiuk, Proc. R. Soc. London A **438**, 531 (1992).

[52] W. R. Smythe, *Static and Dynamic Electricity*, 2nd ed. (McGraw-Hill, New York, 1950), p.76-78, p.118-122.

[53] M. F. Thorpe, unpublished.

[54] J. W. Strutt, Lord Rayleigh, *The Theory of Sound*, 2nd ed., vol. I (Dover, New York 1945; reprinted from the 2nd ed. Published by Macmillan in 1894), p.155.

[55] H. A. Lorentz, *Collected Papers*, vol. III (Martinus Nijhoff, The Hague, 1936), p.1.

[56] J. R. Carson, Bell Syst. Tech. J. **3**, 393 (1924).

[57] V. H. Rumsey, Phys. Rev. **94**, 1483 (1954).

[58] L. Onsager, Phys. Rev. **37**, 405 (1931).

[59] L. Onsager, Phys. Rev. **38**, 2265 (1931).